# Investigating Liquid-Liquid Phase Separation in Lipid Bilayers: A Multi-Modal Approach Utilizing Spectroscopy, Microscopy, and Cryo-EM

A Dissertation Presented for the
Doctor of Philosophy
Degree
The University of Tennessee, Knoxville

Karan Deep Sharma
August 2024

## ACKNOWLEDGEMENTS

I am deeply grateful to the mentors, colleagues, friends, and family whose unwavering support and encouragement made my graduate school journey possible. I owe my deepest appreciation to my advisor, Dr. Fred Heberle. His mentorship has been transformative for me. His considerate nature and willingness to guide me through every challenge has a great impact on my research and me as a person. I cannot stress enough how integral his support has been to my work. He worked with me hands-on in the lab, guiding me through experiments and data analysis. His mentorship also taught me how to navigate the challenges of research and life with a positive attitude and a kind heart.

I am also grateful to my committee members, Dr. Best, Dr. Roy, and Dr. Lavrentovich, for their invaluable guidance, constructive feedback, and continuous direction throughout my academic journey. A special thanks to my collaborators, Dr. Best, Dr. Lou, Dr. Doktorova, and Dr. Waxham, for their invaluable contributions and continuous support. Your expertise and guidance have been an essential part of this work.

I would like to extend my heartfelt thanks to my labmates: Kristen, Emily, Elizabeth, Deeksha, Zidan, Anupam, Loretta, Maryam, and Bill. Working with you all has been a great pleasure. To my friends Aleksandra, Bishal, and Nishita, your companionship and encouragement made this journey not only bearable but enjoyable. Thank you for always being there for me. I also extend my gratitude to my friends from all around the world: Harshit, Navodita, Hardeep, Sumit, Arsh, Gaurang, Ashita, and Shilpa. Your friendship and support have been a source of strength and joy. A special thanks to Ruhani, Dhrupat, and Beant, the first people I met when I landed in Knoxville with all my luggage missing.

I am also immensely grateful to my brother Khushdeep, whose support and understanding have been invaluable throughout this process. Finally, I would like to express my deepest gratitude to my parents. Their unwavering support,

encouragement, and love have been the cornerstone of my academic journey. Their belief in me has been a constant source of motivation. Thank you all for your support and belief in me. This thesis and journey would not have been possible without every one of you.

## ABSTRACT

This thesis explores the characterization of liquid-liquid phase separation in model lipid bilayers using fluorescence, optical microscopy, and cryo-electron microscopy (cryo-EM) integrated with machine learning (ML) analysis. The plasma membrane has a complex composition, lateral heterogeneity and dynamic structure which makes it challenging to study. Simplified model membranes containing three or four-component lipid mixtures, typically comprising low- and high-melting lipids along with cholesterol, form phase separated systems that mimic lateral heterogeneity/lipid rafts in biomembranes. In living cells, lipid rafts are thought to form nanoscopic domains smaller than 200 nm. These domains cannot be resolved by conventional optical microscopy.

For a long time, these nanoscopic domains have been characterized using indirect techniques. Seeing is believing and cryo-EM is employed as the primary tool for visualizing these nanoscopic domains, leveraging its ability to analyze samples particle-by-particle. Chapter 3 introduces a novel application of ML for characterizing phase-separated vesicles in cryo-EM images. It presents a simulation-based study testing various supervised and unsupervised ML methods for classifying the phase state of liposomes. Chapter 4 transitions to an experimental study, applying the supervised ML pipeline developed in Chapter 3 to estimate phase fraction, domain size and domain number in a three-component mixture. Substantial heterogeneity is observed in experimental samples that was not present in simulated liposomes. Together, these studies successfully demonstrate cryo-EM's potential for studying nanoscopic domains in model membranes on vesicle-by-vesicle basis.

Chapter 5 investigates the role of the membrane dipole potential in lipid phase separation, providing insights into the mechanisms driving domain formation in lipid bilayers. This comprehensive study also highlights the synergy between advanced microscopy, ML, and theoretical modeling in elucidating the complexities

of lipid phase behavior. These studies underscore the importance of lipid composition in biological membranes as a mechanism for controlling lipid raft formation and function.

## TABLE OF CONTENTS

## LIST OF TABLES

## LIST OF FIGURES

## ABBREVIATIONS

| | |
|---|---|
| PM | Plasma membrane |
| PC | Phosphatidylcholine |
| Lo | Liquid-ordered |
| Ld | Liquid-disordered |
| $T_M$ | Transition temperature |
| Cryo-EM | Cryogenic electron microscopy |
| CFM | Confocal fluorescence microscopy |
| DSC | Differential Scanning Calorimetry |
| GUV | Giant unilamellar vesicle |
| LUV | Large unilamellar vesicle |
| RBC | Red blood cell |
| MLV | Multilamellar vesicle |
| DPPC | 1,2-dipalmitoyl-sn-glycero-3-phosphocholine |
| DOPC | 1,2-dioleoyl-sn-glycero-3-phosphocholine |
| FRET | Fluorescence Resonance Energy Transfer |
| ESR | Electron Spin Resonance |
| XRD | X-ray Diffraction |
| NMR | Nuclear Magnetic Resonance |
| AFM | Atomic Force Microscopy |
| SANS | Small-angle neutron scattering |
| SLD | Scattering Length density |
| MD | Molecular dynamics |
| ML | Machine Learnnig |
| DT | Decision Trees |
| GBT | Gradient Boosted trees |
| RF | Random Forest |
| LR | Logistic Regression |
| NN | Nearest Neighbor |
| IP | Intensity profile |
| POPG | 1-palmitoyl-2-oleoyl-sn-glycero-3-phospho-(1'-rac-glycerol) (sodium salt) |
| POPC | 1-palmitoyl-2-oleoyl-sn-glycero-3-phosphocholine |
| Chol | Cholesterol |
| TFPC | 1-palmitoyl-2-(dipyrrometheneboron difluoride)undecanoyl-sn-glycero-3-phosphocholine |
| LRPE | 1,2-dioleoyl-sn-glycero-3-phosphoethanolamine-N-(lissamine rhodamine B sulfonyl) (ammonium salt) |
| NBD-DSPE | 1,2-distearoyl-sn-glycero-3-phosphoethanolamine-N-(7-nitro-2-1,3-benzoxadiazol-4-yl) (ammonium salt) |

| | |
|---|---|
| DSPC | 1,2-distearoyl-sn-glycero-3-phosphocholine |
| FMM | fluid mosaic model |
| GPMV | Giant plasma membrane vesicles |
| e-DPPC | 1,2-di-O-hexadecyl-sn-glycero-3-phosphocholine |
| e-DOPC | 1,2-di-O-(9Z-octadecenyl)-sn-glycero-3-phosphocholine |
| POPG | 1-palmitoyl-2-oleoyl-sn-glycero-3-phospho-(1'-rac-glycerol) (sodium salt) |
| POPC | 1-palmitoyl-2-oleoyl-sn-glycero-3-phosphocholine |

# Chapter 1

# Introduction to lipid bilayers, lipid rafts, their characterization, and machine learning

Portions of this chapter (primarily Section 1.3) have been modified from a review paper with permission: Sharma, K. D.; Heberle, F. A.; Waxham, M. N. Visualizing lipid membrane structure with cryo-EM: past, present, and future. Emerging Topics in Life Sciences 2023, 7 (1), 55-65. K.D.S., M.N.W., and F.A.H. conducted the literature survey. K.D.S., M.N.W., and F.A.H. wrote the manuscript

## 1.1 Structure, composition, and function of plasma membrane

The plasma membrane (PM) is an integral component of all living cells. The PM is far from being a passive barrier; rather, it is an extremely dynamic and complex structure[1]. The major constituents of PM include hundreds of types of lipids (including carbohydrate-modified lipids) and proteins. The PM acts as a semi-permeable barrier that separates the interior environment of the cell from the exterior. Its dynamic nature is essential for performing various functions, signaling, and adapting to changes in environmental conditions.

### 1.1.1 Membrane lipids and bilayer structure

Glycerophospholipids, sphingolipids, and sterols are the three major categories of membrane lipids. Glycerophospholipids are the most abundant lipids in cellular membranes.[2] A glycerophospholipid is made up of three structural components that include two acyl chains, a glycerol backbone, and a headgroup (Fig. 1.1). Phosphatidylcholine is the most abundant headgroup in phospholipids. Glycerophospholipids have an amphiphilic structure as they have a polar head group and two non-polar fatty acyl chains. In water, lipids self-assemble to form a bilayer because of the entropy-driven hydrophobic effect. The hydrophobic acyl chains aggregate inward to avoid interaction with water molecules while hydrophilic portions interact with the water on the outer side (Fig. 1.2). Next, there are several types of sphingolipids present in PM including sphingomyelins, ceramides, and gangliosides. Sphingolipids generally have a higher main chain transition temperature ($T_M$) than glycerophospholipids due to the presence of longer saturated hydrocarbon chains, hydrogen bonding, and rigid ceramide backbones. Various studies estimate that the mammalian PM contains 30-40 mole% cholesterol.[3-5] Cholesterol is insoluble in water and readily partitions into membranes, where it helps in the maintenance of membrane fluidity and stability.[6 7]

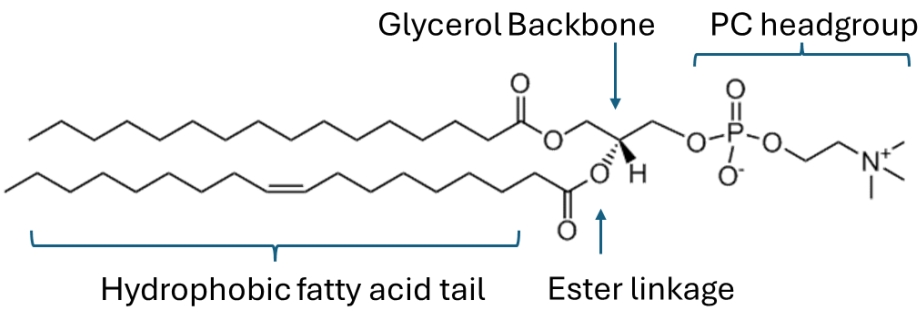


**Figure 1.1 General structure of a phospholipid (in this case, POPC).** Two hydrophobic tails are attached via ester linkages to a glycerol backbone, which is further connected to a polar PC head group.

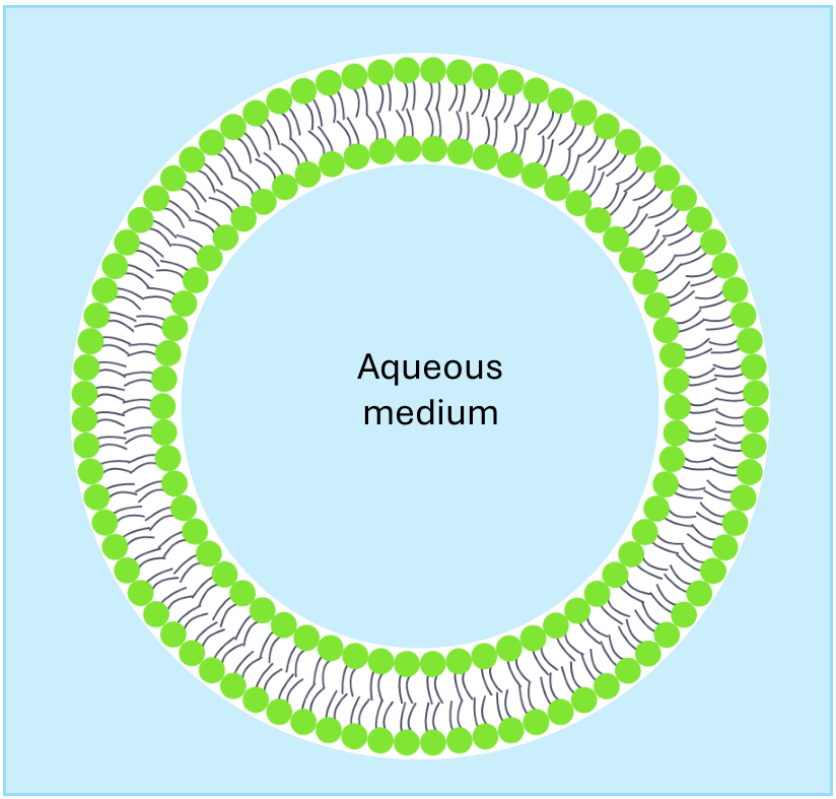


**Figure 1.2 Structure of a lipid bilayer in aqueous medium.** Shown is a 2D projection of a spherical lipid bilayer assembly, illustrating the head groups facing water on both sides and the hydrophobic tails positioned at the core of the bilayer.

The lipid self-assemblies form the basic structure of the PM in which proteins and carbohydrates are embedded or attached to the surface. The PM is a roughly 5 nm thick bilayer structure, defining the boundary between life and death for individual cells. The complex structure of cellular membranes in eukaryotic cells is a result of over three billion years of evolution. Lipidomics has revealed that eukaryotic cells invest vast resources to produce thousands of different kinds of lipids.[8] The diversity in lipid composition by itself highlights the complexity and specificity required for various cellular functions. Even for the simplest cellular membranes, accurately determining the exact lipid composition is challenging.

### 1.1.2 Functions of plasma membrane

The highly dynamic PM serves numerous essential functions in cells.[9] It acts as a selective cellular barrier. Several processes occur inside cells, including the synthesis, modification, and degradation of various materials. Selective permeability is crucial for regulating cell function. There are various kinds of transport proteins present in the PM that regulate the passage of ions, nutrients, and waste products across the PM. Even the membrane components are continuously turned over. Damaged or excess lipids and proteins are identified and removed through various degradation pathways. Further, the PM helps to maintain the pH of the cytosol and preserves adequate cytosolic osmotic pressure. It also stabilizes the cell by providing structural support to maintain its shape. The PM also helps the cell communicate with other cells and its environment. There are receptors present on the surface of the PM that detect extracellular signals from molecules such as neurotransmitters and hormones. It also helps the cells to respond to external stimuli and provide immune surveillance.

### 1.1.3 Asymmetric composition of plasma membrane

The PM has an asymmetric composition across the two leaflets.[4, 10] There is an asymmetry in the degree of lipid unsaturation, in the types of lipid headgroups, and in the number of lipids (Fig 1.3). Flippases and scramblases are the enzymes that maintain and regulate lipid distribution across the two leaflets. Asymmetry is one of the most challenging aspects of studying the PM. A detailed study was performed to determine the composition of individual leaflets of human red blood cell (RBC) PM.[4]

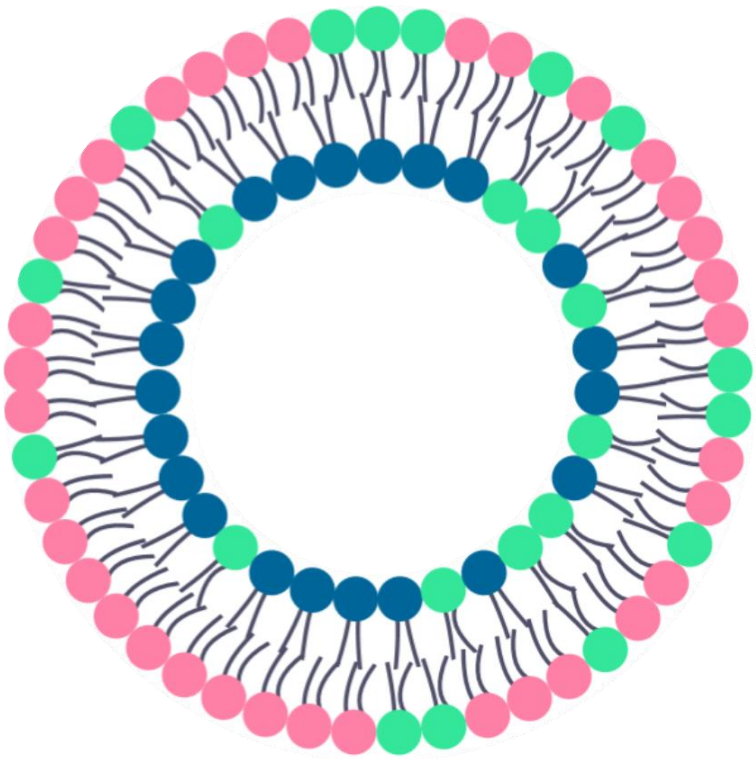

**Figure 1.3 Schematic representation of lipid bilayer asymmetry.** The asymmetry is represented by different composition of lipids in the outer and inner leaflets.

RBCs were chosen for this lipidomic study due to the absence of any internal membranes. Phospholipid unsaturation turned out to be highly asymmetric in composition. The inner leaflet was estimated to have about twice the amount of unsaturated lipids as compared to the outer leaflet. The outer leaflet of the PM was found to be more densely packed and less diffusive as compared to the inner leaflet. The asymmetric structure of the PM also reflects the fact that transmembrane proteins embedded in the PM have an asymmetric structure as well. The asymmetry of PM is believed to influence many core biological functions by modifying the overall biophysical and structural properties of PM.[10, 11]

### 1.1.4 Lateral heterogeneity in the plasma membrane and the lipid raft model

The fluid mosaic model (FMM) was proposed by Singer and Nicolson in 1972.[12] According to FMM, PM is a dynamic and complex lipid bilayer structure with embedded proteins. The lipid bilayer acts as a fluid matrix where both lipids and proteins move laterally within the layer. In 1973, Shimshick and McConnell suggested the presence of lateral heterogeneity in lipid bilayers.[13] In 1978, Wunderlich et al. suggested the presence of liquid-liquid phase-separated systems.[14] Several experimental studies explore the lateral heterogeneity and phase separation in lipid bilayers in the 1980s[15] and 1990s.[16]

In 1997, Kai Simons and coworkers proposed a model for PM organization called the lipid raft hypothesis[17]. According to this model, PM lipids are not randomly mixed within the bilayer, but instead self-organize into domains of a liquid-ordered (Lo) phase that float in a matrix of liquid-disordered (Ld) phase (Fig 1.4). The Lo domains, referred to by Simons as “lipid rafts”, were proposed to be compositionally enriched in saturated lipids and cholesterol. The stability of lipid rafts is attributed to cholesterol, which exhibits a strong affinity for sphingolipids.[18] This interaction leads to the dense packing of lipids within lipid rafts. Further, it also results in a thicker membrane region for the Lo domain as compared to the surrounding Ld phase. Lipid rafts are suggested to play an important role in membrane signaling, protein sorting, and trafficking.[19]

**Figure 1.4 Lipid rafts.** A representation of lipid rafts (Lo phase, orange) floating in the matrix of Ld phase (gray).

## 1.2 Simple ternary lipid mixtures as model systems

As discussed previously, the PM has a complex composition and dynamic structure. It becomes extremely challenging to pinpoint the function of each kind of lipid. The presence of proteins and carbohydrates makes it even more difficult to study the PM. The presence of asymmetry adds another layer of complexity to it. Proteins and lipids are estimated to make up equal portions of the cell membrane by mass. It raises a challenge if we can use lipid-only mixtures to model PM accurately. It was found that around 80-85% of the protein mass is situated in the aqueous environment and the rest is embedded within the lipid bilayer and proteins make up around 20% of the membrane area.[20] Therefore, lipid-only models can still provide valuable insights into certain aspects of PM. To understand the formation and functionality of lipid rafts, several studies used simplified three-component biomimetic mixtures of lipids.[21] These ternary mixtures usually include cholesterol, a high melting lipid (saturated lipids such as DPPC, DSPC, or sphingomyelin), and low melting lipid (unsaturated lipids such as DOPC and POPC).[22] Liquid-liquid phase separation in ternary lipid mixtures serves as a model for studying lipid rafts (Fig 1.5).[23] These investigations involved analyzing the behavior of various ternary lipid mixtures at different temperatures. Ternary phase diagrams were solved for these mixtures at controlled temperatures.[24] Phase diagrams reveal the compositions for which Lo and Ld phases coexisted, and thus provide a summary of the conditions under which lipid rafts might form.[25] They can also provide insights into how changes in temperature or lipid composition can influence membrane fluidity and structure. This approach, based on physical chemistry, provides a more controlled study environment for a deeper understanding of lipid rafts.

## 1.3 Lipid bilayer phases

Lipid bilayers are polymorphic, undergoing dramatic structural transitions as a function of temperature, pressure, hydration, and lipid composition; here, we focus on the structure of the biologically relevant bilayer phases. Membranes composed of a single lipid type have a characteristic main transition temperature ($T_M$). Under typical biological conditions of full hydration and atmospheric pressure, bilayers are in a disordered fluid state above $T_M$ and an ordered, solid-like state at temperatures well below $T_M$ (Figure 1.6).

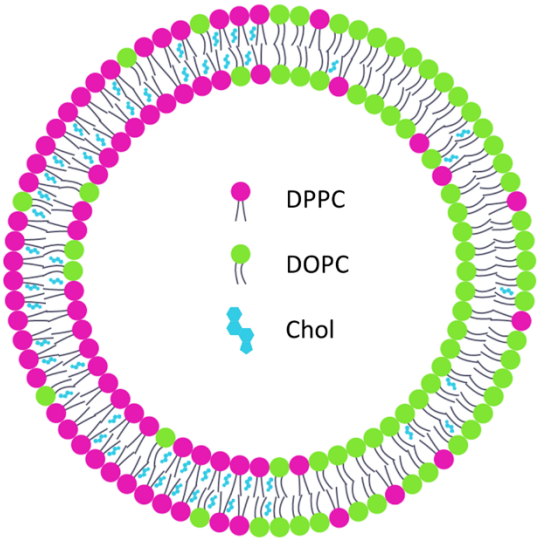


**Figure 1.5 Phase-separated model membrane.** Phase-separated vesicle composed of DPPC, DOPC, and Cholesterol.

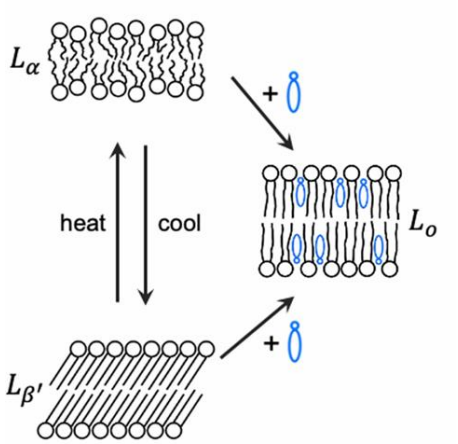


**Figure 1.6 Lipid bilayer phases and phase transitions.** Bilayers composed of PC lipids are in a gel state ($L_{\beta'}$) well below their main transition temperature and a fluid state ($L_\alpha$/Ld) above their main transition temperature. The addition of cholesterol converts both gel and fluid bilayers to a liquid-ordered phase (Lo).

The disordered fluid phase (termed $L_\alpha$, or Ld when the bilayer is composed of a mixture of lipids) is characterized by fast lateral lipid diffusion and highly disordered acyl chains (rapid trans-gauche isomerization). In contrast, lipids in a gel phase bilayer diffuse much more slowly, and their hydrocarbon chains are in a highly ordered, all-trans configuration and tilted with respect to the bilayer normal ($L_{\beta'}$ phase).[26]

In addition to sphingolipids and glycerophospholipids, the plasma membrane of eukaryotic cells also contains an abundance of cholesterol (30-50 mol%) that serves a critical role in modifying the phase behavior. When added to saturated lipid bilayers at concentrations of a few mole percent, cholesterol forces nearby lipids to align parallel with the bilayer normal, thus converting the $L_{\beta'}$ phase to an untilted $L_\beta$ gel phase.[27] At higher concentrations, cholesterol breaks up the long-range crystalline order that is characteristic of gel phases, allowing the lipids to diffuse rapidly while maintaining their high chain conformational order.[28] When added to lipids in the disordered Ld phases, cholesterol increases the probability of trans conformers, thus straightening the hydrocarbon chains. The ability of cholesterol to create and maintain high lipid chain conformational order while allowing for fast lipid lateral diffusion results in a unique state termed the liquid-ordered (Lo) phase.[29] Raft phenomena in cell membranes are thought to be a manifestation of Ld + Lo phase coexistence.[30]

### 1.4 Importance of studying lipid rafts

Lipid rafts are important for cell function, protein sorting, and signaling. It has been proposed that viruses can hijack lipid rafts to exploit the host cells.[31, 32] Studying the interactions of lipid rafts in both model and biological membranes can lead to the development of drugs and vaccines to prevent infections.[32] Lipid rafts are proposed to serve as biomarkers for certain diseases.[33] Abnormalities in lipid raft composition are associated with neurodegenerative disorders.[34] Therapies for the treatment of Alzheimer's disease can be designed to modify raft composition. Targeting lipid rafts in membranes presents a novel approach for drug design and development.[35] Nanoparticles can be designed to interact with lipid rafts for targeted delivery systems.[36] Lipid rafts have a great potential for developing innovative therapeutic and diagnostic tools.

## 1.5 Characterization of phase-separated systems and examples

Experimental characterization of phase-separated systems is extremely important since there are many unanswered questions.[37] Particularly, the biophysical properties of lipid rafts and the mechanism of their formation are unclear.[9] Rafts are small and transient in nature, therefore understanding the factors that control the size and stability of these rafts becomes challenging.[38] In living cells, lipid rafts are thought to form nanoscopic domains smaller than 200 nm. These domains cannot be resolved by conventional optical microscopy, which has a resolution limit of approximately 250 nm. Several methods and tools have been developed to elucidate their structure and some of the important ones are discussed below.

### 1.5.1 Fluorescence microscopy to study phase separation in giant unilamellar vesicles

Fluorescence microscopy utilizes fluorescent dyes to label specific components of the bilayer (e.g., lipids or proteins). When these labels are excited by light at a particular wavelength, they emit light at a longer wavelength, which can be detected and visualized. This method enables imaging of the spatial arrangement of lipids and proteins within the bilayer. Wide-field and confocal fluorescence microscopy (CFM) are very powerful optical imaging techniques. In wide-field fluorescence microscopy, a broad light source is used to illuminate the entire sample. It is simple to use and suitable for observing large micron-sized structures, but the large amount of out-of-focus light reduces the resolution. This is not a problem for CFM. CFM is selective illumination at a fixed wavelength and collects light from a specific focal plane within the sample (Fig 1.7). This eliminates out-of-focus light from any other plane, not under focus. This is achieved by scanning the sample using a focused laser beam and using a pinhole aperture in the detection path to block out-of-focus light. CFM gives a better resolution and contrast as compared to wide-field fluorescence microscopy. Giant unilamellar vesicles (GUVs) are the simplest model structure of PM. The typical diameter of a GUV ranges from 10-100 micrometers. They are significantly larger than most cell membranes and other types of vesicles.

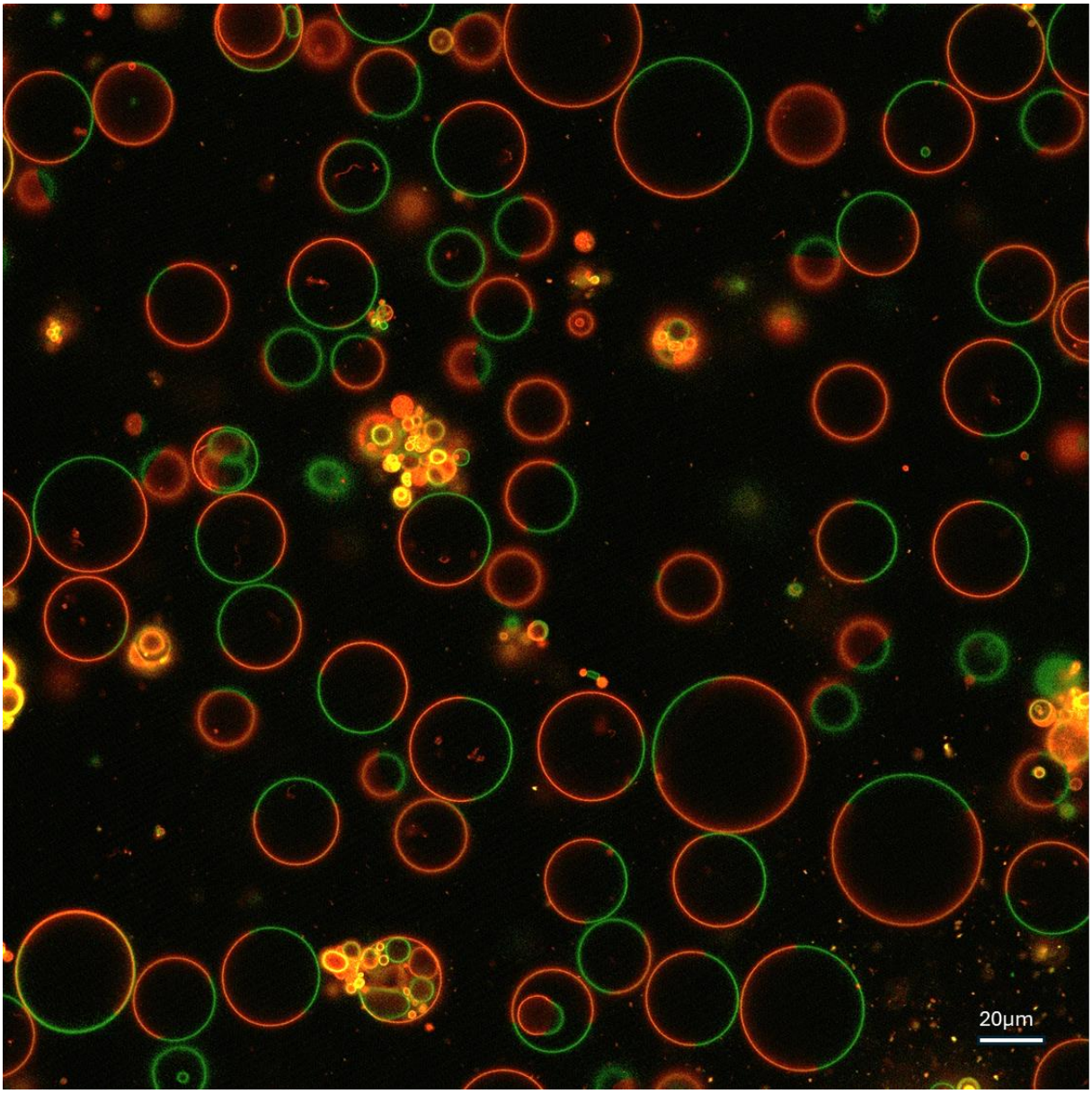


**Figure 1.7 A confocal image of a phase-separated GUV sample DPPC/DOPC/Chol (39/39/22) at room temperature.** The red dye, 1,2-dioleoyl-3-[16-N-(Lissamine rhodamine B sulfonyl) amino]palmitoyl-sn-glycerol] (LR-DOPE), predominantly partitions into the Ld phase, while the green dye, 1,2-distearoyl-sn-glycero-3-phosphoethanolamine-N-(7-nitro-2-1,3-benzoxadiazol-4-yl) (ammonium salt) (NBD-DSPE), shows a slight preference for the Lo phase over the Ld phase (LR-DOPE and NBD-DSPE at probe/lipid ratios of 1/2000 and 1/1000, respectively).

GUVs can be easily observed using fluorescence microscopy and have been great tools for studying phase behavior of ternary lipid mixtures (Fig 1.7). Fluorescent lipid probes can be designed to partition in specific lipid phases. GUVs have been widely used to study the distribution and dynamics of various phase-separated mixtures. Using fluorescence microscopy, we can directly observe liquid phases in giant unilamellar vesicles. In 2003 Veatch and Keller estimated the phase boundaries for the DPPC/DOPC/Chol mixtures using fluorescence microscopy.[39] They studied various compositions at controlled temperature conditions. In the following year, several studies were conducted to estimate phase boundaries in systems with different combinations of low and high melting lipids.[40-42] These studies on GUVs significantly impacted the potential development of drug delivery systems.[43, 44]

### 1.5.2 Fluorescence microscopy to study phase separation in giant plasma membrane vesicles (GPMVs)

GPMVs are cell-derived plasma membrane blebs. They can be induced chemically or by changing the osmotic pressure of the solution.[45] These blebs have a similar composition to the PM they are obtained from, being composed of lipids from both leaflets and both peripheral and membrane proteins. They are excellent model systems for studying various aspects of the plasma membrane using fluorescence microscopy.[46] GPMVs prepared from RBL mast cells showed liquid-liquid phase separation at room temperature.[47] At 37°C, these GPMVs appeared optically homogeneous which is also the case in many biomimetic lipid mixtures. Labeled lipids and membrane proteins were used to study the partition of these tagged molecules in the GPMVs. GPMVs are potential candidates in drug delivery research, either as a model for the plasma membrane or as delivery agents themselves.[48]

### 1.5.3 Fluorescence microscopy to study phase separation in the unperturbed cell system

The vacuole membranes of the yeast Saccharomyces cerevisiae have shown micron-sized liquid-liquid phase separation.[49] It is the only known biological membrane that shows phase separation in live unperturbed conditions. Given the large size of the domains, fluorescence microscopy with temperature control was used to study the phase

separation. The phase transition temperatures of the vacuole membranes were measured and were found to be directly proportional to the growth temperature of yeast cells. It was suggested the cells physiologically adapt to control this transition point. For example, yeast can adjust the level of ergosterol in the vacuole membranes to regulate the phase transition. Another interesting finding in this study was that the depletion of ergosterol in vacuole membranes induced phase separation. In model membranes, moderate levels of sterol are required for liquid phases to coexist. It was suggested that sterol content might be too high to allow phase separation and therefore, decreasing the sterol content in these membranes could potentially lead to the formation of coexisting liquid phases.

### 1.5.4 Fluorescence Resonance Energy Transfer (FRET) to study phase separation

FRET is another powerful fluorescence technique that is widely used to study molecular interactions. It has been widely used for investigating phase separation in ternary lipid mixtures.[50, 51] The basic principle of FRET is the non-radiative transfer of energy from a donor fluorophore to an acceptor fluorophore when they are in close proximity. This transfer only occurs when the emission spectrum of the donor fluorophore overlaps with the absorption spectrum of the acceptor fluorophore. A specific wavelength is selected to excite only the donor fluorophore. If the donor and acceptor fluorophores are in close proximity, energy transfer occurs, resulting in the emission of fluorescence from the acceptor. FRET occurs over very short distances (typically 1- 10 nm) making this process extremely sensitive to distance changes. FRET efficiency (E) is given by the following equation:

$$E = \frac{1}{1 + \left(\frac{R}{R_0}\right)^6}, \qquad (1.1)$$

where R is the distance between the donor and acceptor, and $R_0$ is the Förster radius. Förster radius is the distance at which the FRET efficiency is equal to 50%. Certain lipid species are labeled with donor and acceptor fluorophores and FRET efficiency is recorded.[52] When the FRET efficiency is high, the labeled lipids are in close proximity and suggesting that they are present in the same phase.[50, 53] Various FRET experiments study

changes in FRET efficiency over various lipid compositions over a temperature range.[54] FRET has also been used to study the interactions between proteins and lipids.[55]

### 1.5.5 Small-angle neutron scattering (SANS) to study phase separation

SANS is another method for investigating biological and model lipid bilayers. It covers length scales ranging from a few nm to over 100 nm.[56] SANS has the capability to distinguish between different isotopes of hydrogen giving it an advantage over other scattering techniques. This unique ability allows SANS to provide insights into membrane details that are not easily accessible using other techniques like small angle X-ray scattering. SANS intensity is evaluated as a function of scattering vector q in controlled temperature conditions.[57] For the detection of domains, a contrast between the scattering length density (SLD) of the coexisting phases is required. To achieve this contrast, a chain-deuterated high-melting lipid is used also with regular (i.e., non-deuterated) low-melting lipids. The SLD for deuterated lipids is significantly higher than that of regular lipids. Next, contrast matching strategies are used for detecting domains within lipid bilayers. The scattering properties of the aqueous solvent are matched to the average composition of the bilayer. As a result, the usually dominant transverse bilayer scattering contribution is minimized. This reduction allows for the clear observation of lateral SLD variation that occurs when chain-deuterated lipids segregate from regular lipids (i.e., domain formation). This technique reveals a peak in the form factor that shifts to higher q values as the domain size decreases.

### 1.5.6 Other techniques to study phase separation

All the techniques discussed previously are the ones that have been used in the upcoming sections. Various additional techniques have been used to study and characterize coexisting liquid phases in lipid bilayers. Among these are electron spin resonance (ESR) spectroscopy,[58] X-ray diffraction (XRD),[59] nuclear magnetic resonance (NMR) spectroscopy,[60] atomic force microscopy (AFM),[61] and electron microscopy.[62] Each of these techniques offers unique insights into the structural and dynamic properties of lipid bilayers. ESR is based on the behavior of paramagnetic spin probes embedded within the membrane. These spin probes exhibit distinct ESR spectra depending on their

microenvironment. Similarly, NMR can distinguish between different phases in a lipid bilayer based on the distinct chemical environments and mobility of lipid molecules in each phase.[63] Next, XRD is particularly effective at identifying ordered phases in lipid bilayers. Specific diffraction peaks are observed in ordered phases that correspond to the periodic arrangement of lipids in these regions. XRD can be used to measure the thickness of the lipid bilayer.[64] The repeat distances of multilamellar lipid bilayers are correlated to bilayer thickness. AFM can be used to directly visualize lipid domains.[58] The coexisting liquid phases appear as distinct regions of different heights or stiffness. It can be used to measure domain size, shape, and distribution.

### 1.6 Molecular dynamics (MD) simulation

MD simulation is a powerful and widely used computational technique used to study the structure, dynamics, and phase separation in lipid bilayers.[65] MD simulations provide atomic-level details that are difficult to capture through experimental methods alone. The positions and velocities of atoms/molecules are calculated using Newton's equations of motion. This allows researchers to observe the temporal evolution of the system. The interactions between particles are described by potential energy functions. Both bonded interactions such as bond stretching, angle bending, and dihedral torsions, and non-bonded interactions such as van der Waals forces, and electrostatic forces are included in the calculations.

Several parameters that describe the behavior of the lipid bilayer have been studied using MD simulations. Area per lipid, chain order parameter, and lateral diffusion are some of the most studied parameters.[66] Lipids in ordered phases tend to have a much lower area per lipid because of the higher packing density of lipids. The chain order parameter is higher for lipids in ordered phases as compared to disordered phases. Radial distribution functions are often calculated to characterize the spatial distribution of lipid molecules and cholesterol. Formation of clusters and lateral diffusion coefficients are other parameters that can be obtained from the MD simulation study. When combined with experimental data, MD simulations provide a deeper understanding of biological membranes.

## 1.7 Cryogenic electron microscopy (cryo-EM)

Cryo-EM is another high resolution technique to study phase separation in lipid bilayers.[67] Cryo-EM involves imaging samples at extremely low temperatures which are typically below -150°C. The rapid freezing of the sample in vitreous ice preserves the native structures or at least gives us near-native conditions. The short wavelength of electrons provides us with high resolution, and a small electron dosage prevents sample degradation. The use of cryo-EM for studying lipid membranes is discussed in detail in Chapter 2. We use machine learning for our analysis in the chapters that follow. A brief introduction to machine learning methods is given below.

## 1.8 Introduction to machine learning methods

Machine learning is a branch of artificial intelligence in which computers learn from data and perform various tasks without being explicitly programmed. The basic idea behind machine learning is to develop methods/algorithms that can recognize patterns and make predictions. Machine learning enables us to tackle complex problems within large and complex datasets. Further, it enables us to extract valuable insights from data that might not be apparent through traditional analysis methods. These insights can help us optimize and automate processes that are time-consuming or hard to perform manually. Various types of machine learning have been developed over time to cater to diverse applications. In our studies, we have particularly used supervised and unsupervised learning approaches. Our supervised approach will focus on binary classification. Binary classification is a fundamental machine learning task where the goal is to classify given data points into one of two classes. These classes are typically denoted as class 1 and class 0. Binary classification has wide-ranging applications across various fields such as information technology (spam vs. genuine emails), medicine (benign vs. malignant tumors), and finance (fraudulent vs. legitimate transactions). For the unsupervised approach, we will be performing binary clustering, where the goal is to partition the data into two clusters without any prior knowledge of class labels.

### 1.9 Supervised learning

In supervised learning, the algorithm learns patterns and relationships from labeled training data to make predictions or decisions about new data. The datasets consist of two main components: features and labels. Features are the most important component of a dataset. Features are the input variables or attributes that contain all the information or characteristics of the data. The labels are the output or the target variable that the model is trying to classify or predict.

To illustrate some essential aspects of machine learning, Table 1.1 presents a contrived example of six lipids, each characterized by distinct features such as saturation in lipid chains, the count of double bonds, chain length, melting point, and charge. Measurable features, such as chain length or the count of double bonds, as well as descriptive properties like the presence of unsaturation or chain asymmetry, are associated with each example in the dataset. Each row represents an individual example, and each column represents a particular feature. It's important to acknowledge that not all features carry equal significance or relevance to the study of interest. Certain features have a more pronounced impact on the model's ability to learn patterns and relationships within the data. Identifying and prioritizing these features is a critical aspect of refining the model's performance. In this limited dataset, the melting point turns out to be the feature with the most significant influence on the labels. DPPC and POPE are characterized by high melting points and are labeled as 1. The remaining lipids have lower melting points and are labeled as 0. In this scenario, features such as chain asymmetry and charge don't contribute significantly to the classification process. A larger dataset with hundreds of lipids and associated features will lead to more robust training of the model. As the model can learn from a wider range of examples, the model starts to identify subtle patterns and relationships among various features. Now, all the additional features beyond the melting point can also contribute meaningfully to the decision-making process.

Machine learning methods can only act on the data that is provided to it and the way it is provided. The data in the raw form may not be readily usable and may need formatting in a certain way. If there are any external parameters that can have a huge impact on the,

**Table 1.1** Lipids and their features are shown as a training dataset, along with labels.

| Lipid | Unsaturation | Number of double bonds | Chain Asymmetry | Carbon chain length | Melting point (C) | Charged | Labels |
|---|---|---|---|---|---|---|---|
| DPPC | No | 0 | No | 16/16 | 41 | Neutral | 1 |
| DLPC | No | 0 | No | 12/12 | -2 | Neutral | 0 |
| DOPC | Yes | 2 | No | 18/18 | -17 | Neutral | 0 |
| POPC | Yes | 1 | Yes | 16/18 | -2 | Neutral | 0 |
| POPG | Yes | 1 | Yes | 16/18 | -2 | Negative | 0 |
| POPE | Yes | 1 | Yes | 16/18 | 38 | Neutral | 1 |

outcome of the data, therefore the problem is not self-contained, and ML cannot accurately predict the results. It becomes clear that protocols and conditions in experimental data collection need to be kept as uniform as possible (e.g., sample preparation, storage, instrument settings and environment for data collection). Data collection is followed by data processing steps like cleaning, filtering, formatting, and labeling.

After the model is trained, the next step is assessing the quality of the model and determination of acceptable accuracy threshold. Underfitting and overfitting are major problems in machine learning. Underfitting happens when a model is too simple to capture the patterns in the data. It results in poor performance or accuracy. Adding more data points and additional features can be useful in reducing the underfitting. Overfitting happens when a model is very complex and captures noise along with the actual patterns. Such a model will perform very well on training data but poorly on unknown new data. The goal is to find a balance where the model learns from the more useful features without capturing noise. In our studies, we have used tens of thousands of examples for training various simple and complex models. The default setting for all the machine learning methods in Wolfram Mathematica 13.2 was used for classification tasks. All the default method details and hyperparameters for each method are mentioned in each method.

### 1.9.1 Decision Tree (DT)

Decision Tree is one of the most straightforward machine learning methods known for its ease of understanding and interpretation. DT can be used to handle both categorical and continuous data. Decision Tree constructs a model by learning decision rules from training data. It adopts a hierarchical tree structure that includes a root node, internal nodes, branches, and leaf nodes. The root node of the tree represents the entire dataset. Every node within the decision tree serves as a test for a specific attribute, and its branches represent outcomes for that test. The process is recursive and continues until nodes cannot be further divided or specific termination criteria are met. A decision tree divides a node using all available features or variables and selects the split that results in the most similar sub-nodes. When the recursive process stops, the leaf nodes of the tree

correspond to a specific class label. The accuracy of a decision tree is significantly influenced by the splitting criteria it uses. Mathematica uses the CART (Classification and Regression Trees) algorithm for decision tree classification. It uses Gini impurity as a criterion to determine the optimal attribute for splitting. Gini impurity represents the probability of misclassifying a randomly chosen data point in the dataset. It is given by Eq. 1.2:

$$Gini\ Impurity = 1 - p_1^2 - p_2^2. \qquad (1.2)$$

where $p_1$ and $p_2$ are probabilities for each of the two classes. The best split in a feature is chosen by minimizing the Gini Impurity. Decision trees are straightforward but not very flexible in nature. They are sensitive to small changes in the data and often lead to overfitting. To address these issues ensemble methods such as Random Forest and Gradient Boosted trees are used. These methods are based on decision trees and offer enhanced robustness and precision in their predictions.

### 1.9.2 Random Forest (RF)

Random Forest is an ensemble ML method that uses a combination of predictions from multiple decision trees. Random Forest is particularly known for its capability to effectively manage high-dimensional data sets. In the first step, Random Forest creates multiple subsets of the training data with allowed replacement. Each tree in the Random Forest is trained on a slightly different dataset, comprising randomly selected, duplicated data points at the expense of a few missing data points. Subsequently, each tree uses a random subset of features for node splitting, ensuring diversity among the trees and preventing dominance by a select few features. In classification studies, new data is independently evaluated by each tree for a class, and the final prediction is determined by the class that receives the most votes. Using multiple trees and randomized feature selection reduces overfitting and makes the model more flexible toward new data to produce more accurate and robust predictions.

### 1.9.3 Gradient Boosted Trees (GBT)

Gradient Boosted Trees is another ensemble machine learning method that constructs multiple decision trees sequentially in an adaptive manner to enhance accuracy. For classification tasks, GBT uses class distribution or class probabilities for making initial predictions. The majority class is used as the initial prediction. After initializing the model, GBT calculates residual errors at each step to construct an adaptive sequence of decision trees. Each new tree learns from the misclassifications made by its predecessors to minimize the residual error. This is known as the gradient descent algorithm. Each additional tree introduced in the boosting process is a weak learner, typically characterized as a shallow tree with limited depth. Ultimately, a robust classification model is built that captures complex patterns within the data. Each tree based on its performance is assigned a weight that determines its contribution to the final classification. GBT frequently performs better in classification tasks when compared to Random Forest, as it optimizes for correcting errors made by the previous trees.

### 1.9.4 Logistic regression (LR)

Logistic regression is a simple and powerful method particularly used for binary classification problems. Logistic regression uses the sigmoid function ($\sigma$) to model the probability as shown in Eq. 1.3. A set of input features is combined linearly with coefficients ($\beta_1, \beta_2, \beta_3$ ... $\beta_3$) and an intercept ($\beta_0$), Eq. 1.4. These coefficients are learned and optimized during the model training. Using the sigmoid function, for this linear combination a probability value between 0 and 1 is evaluated. This probability represents the likelihood of the target event occurring. The probability threshold is typically set at 0.5 to give a binary decision.

$$\sigma(z) = \frac{1}{1 + e^{-z}}. \qquad (1.3)$$

$$z = \beta_0 + \beta_1 x_1 + \beta_2 x_2 + \beta_3 x_3 \ldots\ldots\ldots\ldots + \beta_n x_n. \qquad (1.4)$$

### 1.9.5 Nearest Neighbors (NN)

The nearest neighbor algorithm is another straightforward and powerful machine learning method. It can be used for both classification and regression tasks. It measures the distances between the unknown data point and other data points in the training dataset. The unknown point is classified into the category with the shortest distances to the points used in training datasets. It doesn't require a training phase since it stores the training data.

## 1.10 Unsupervised Learning

Unsupervised learning involves training algorithms on unlabeled data. The goal is to find hidden patterns within the data and cluster the data as required. There are no predefined outputs or labels in this case. The model independently discovers patterns and structures within the data. Unsupervised learning is mainly used for clustering the data points based on similarity. In our studies, we have used k-means and k-medoids clustering on raw data as well as reduced data.

### 1.10.1 *k*-Means clustering

In *k*-means clustering, the data is partitioned into *k* clusters by minimizing the variance within each cluster. In *k*-means clustering the number of clusters '*k*' is predefined. Each data point belongs to the cluster with the nearest mean. The algorithm follows very simple steps. The initial cluster centroids are selected randomly. Then all data points are assigned to the nearest centroid based on the Euclidean distance. The centroids of the clusters are recalculated. The mean of all data points within a cluster becomes the new centroid. The goal is to minimize the sum of squared Euclidean distances between each data point and the nearest centroid. New centroids are evaluated until a minimum is reached and the cluster is as compact as possible.

### 1.10.2 *k*-Medoids

*k*-medoids is very similar to *k*-means but use medoids (like median) instead of means as cluster centers. A medoid is an actual data point from the dataset instead of the mean used in the previous case and the rest of the procedure is very similar. Both methods

have their advantages and disadvantages. *k*-medoids is considered more robust to noise and outliers compared to more efficient *k*-means. The choice between these two methods is dependent on the specific nature of the dataset and the problem we are trying to solve.

### 1.10.3 Principal component analysis

Principal Component Analysis (PCA) is a dimension reduction technique. It is used in machine learning and statistics to simplify complex datasets. In a dataset with many features, it becomes very hard to see patterns and trends. In such a case, PCA can be a very helpful tool. It reduces the number of features while keeping most of the important information. These new reduced features are linear combinations of original features and are referred to as principal components. The first principal component captures the most variation, followed by the second, and so on. The first few principal components can be used to analyze data without losing too much important information. PCA is often paired with *k*-means and *k*-medoids clustering after dimension reduction.

### 1.10.4 Challenges of unsupervised ML

Evaluating the performance of unsupervised algorithms is not straightforward, since we do not have any labels. In some cases, choosing the right number of clusters is challenging, particularly when there are no clear boundaries between the clusters. Next, the number of features or components required for clustering needs specific knowledge and experimentation. Another challenge is that unsupervised learning algorithms make assumptions about cluster data. *k*-means assumes clusters are spherical and equally sized. This is not always the case in real-world data.

## 1.11 Limitations and disadvantages of experimental techniques used to study phase behavior

Many studies combine multiple techniques to thoroughly investigate their hypotheses, as each method has its own set of limitations. Optical microscopy has a limited resolution compared to other techniques and cannot be used to observe nanoscopic domains. FRET and other fluorescence techniques require the addition of fluorescent labels to the system under study. These probes, although added in marginal fractions, may alter the actual behavior and interactions. Further, FRET, NMR, ESR, SANS, and XRD are indirect

methods for characterization. SANS requires access to neutron sources which are extremely limited. Further, SANS data is very challenging to analyze. Although AFM gives us high-resolution topographical images of lipid bilayers, it requires the immobilization of membranes on solid supports, potentially altering their structure and dynamics. There was a clear need for a technique that offers high resolution, non-destructive analysis and operates without the need for probes or support structures. Such a method would allow for the characterization of lipid bilayers in their native environment while preserving their structural integrity and dynamic properties. Although cryo-EM meets all the required criteria, it comes with its own set of challenges.

# Chapter 2

## Cryo-EM insights into lipid bilayers: Historical evolution, techniques, and visualization of lateral heterogeneity

Portions of this chapter have been modified from a review paper with permission: Sharma, K. D.; Heberle, F. A.; Waxham, M. N. Visualizing lipid membrane structure with cryo-EM: past, present, and future. Emerging Topics in Life Sciences 2023, 7 (1), 55-65. K.D.S., M.N.W., and F.A.H. conducted the literature survey. K.D.S., M.N.W., and F.A.H. wrote the manuscript.

## 2.1 Abstract

The development of cryogenic electron microscopy (cryo-EM) has evolved immensely in the last several decades and is now well-established in the analysis of protein structure both in isolation and in their cellular context. This chapter focuses on the history and application of cryo-EM to the analysis of membrane architecture. Parallels between the levels of organization of protein structure are useful in organizing the discussion of the unique parameters that influence membrane structure and function. Importantly, the timescales of lipid motion in bilayers with respect to the timescales of sample vitrification is discussed and reveal what types of membrane structure can be reliably extracted in cryo-EM images of vitrified samples. Appreciating these limitations, the application of cryo-EM to examine the lateral organization of ordered and disordered domains in reconstituted and biologically derived membranes is provided. Further, the optimization of experimental conditions and data analysis methods for quantitative analysis of cryo-EM images of lipid bilayers are discussed.

## 2.2 Introduction

Structure-function relationships are present at all levels of biological organization. These organizations can range anywhere from individual molecules to entire ecosystems. One crucial level in this hierarchy is the supramolecular organization of the four primary molecular building blocks of life: amino acids, nucleotides, sugars, and lipids. There have been major advances in the 20th century that enhanced our understanding of protein and nucleic acid structure. The development of powerful X-ray and neutron diffraction techniques has allowed us to resolve atomic-level structures. In the last 30 years, advancements in cryogenic electron microscopy (cryo-EM) and computational power have significantly accelerated the structural revolution.[68] Cryo-EM has provided new insights into protein structures that were difficult to crystallize and thus making them

recalcitrant to diffraction-based methods.[69] Additionally, cryo-preservation techniques now allow for the high-resolution structural analysis of macromolecular complexes and even intact cells in their native cellular environments.[70, 71]

As discussed previously, lipids self-assemble mainly through weak non-covalent interactions to form lipid bilayers. These bilayers form the plasma membrane of all living cells and the enclosing membranes of internal organelles in eukaryotes. While the structural biology revolution has mainly focused on proteins, understanding the structure and organization of lipid membranes is equally crucial for elucidating their function. Like proteins, lipid bilayers exhibit a hierarchy of organization: all the biological membranes have characteristic lipid compositions;[72] (b) these compositions can exist in different lamellar phases;[73] and (c) domains of different phases can coexist within the same membrane.[74, 75] This hierarchy of membrane organization can be analogized to the primary, secondary, and tertiary structures of proteins.

Advanced lipidomics and biophysical techniques have provided extensive knowledge about the primary and secondary structures of biological membranes.[4] The phase state of a bilayer and its associated chemical and physical properties has been characterized as a function of temperature and cholesterol concentration for many glycerophospholipids and sphingolipids. NMR and scattering techniques have played a prominent role in determining the detailed structure of the various bilayer phases.[76-78] Among the structural parameters obtained from these techniques are bilayer thickness, average area per lipid, and hydrocarbon chain order parameter profiles, while lateral diffusion has been measured with fluorescence correlation spectroscopy and fluorescence recovery after photobleaching.

There is a significant gap that remains in our understanding of membrane tertiary structure. The most prominent example of this is lipid rafts. Lipid rafts are enriched in sphingomyelin and cholesterol which makes them thicker and less compressible than the disordered sea of unsaturated lipids that surrounds them.[17] In resting cells, consensus estimates for raft size converge at tens of nanometers, making their structure difficult to characterize with conventional optical microscopy.[79, 80] As a direct imaging technique, cryo-EM holds great promise for answering questions about plasma membrane tertiary

structure—that is, the size, shape, and connectivity of membrane nanodomains—that will likely lead to novel functional insights.

### 2.3 Evolution of cryo-EM in unveiling lipid bilayer structures

#### 2.3.1 First cryo-EM investigation of model lipid membranes

To our knowledge, Lepault et al. were the first to focus a cryo-EM study entirely on lipid bilayer structure.[81] They prepared unilamellar liposomes from PC lipids by controlled detergent dialysis and vitrified the samples with liquid nitrogen-cooled propane. Three saturated lipids — DLPC (1,2-dilauroyl-sn-glycero-3-phosphocholine), DMPC (1,2-dimyristoyl-sn-glycero-3-phosphocholine), and DPPC (1,2-dipalmitoyl-sn-glycero-3-phosphocholine) — were investigated, covering a wide range of main chain transition temperatures ($T_M$ = –2, 24, and 42ºC, respectively). The unsaturated lipid DOPC (1,2-dioleoyl-sn-glycero-3-phosphocholine; $T_M$ = –17ºC) was also studied to determine the influence of a *cis* double bond in the lipid chains. Cryo-EM projection images showed quasi-spherical vesicles characterized by two high-density, roughly concentric rings that were attributed to the electron-dense polar headgroups of the inner and outer bilayer leaflets. The bilayer thickness, estimated as the distance between the high-density lines, was found to be sensitive to sample temperature immediately prior to vitrification: vesicles showed a uniform thickness if vitrified from a temperature well above $T_M$ but a faceted appearance with variable thickness if vitrified from well below $T_M$. For all bilayers, the measured thickness was 40 $\pm$ 5 Å regardless of vitrification temperature.

Further investigation with electron diffraction measurements revealed characteristic reflections of an $L_{\beta'}$ phase for bilayers vitrified from below $T_M$, suggesting that gel phase bilayers are structurally preserved during cryo-preservation. Remarkably, DMPC and DLPC bilayers vitrified from well above $T_M$ (i.e., in the $L_\alpha$ phase) showed reflections consistent with an *untitled* gel ($L_\beta$) phase, rather than the single broad reflection characteristic of $L_\alpha$. In contrast, the electron diffraction pattern of vitrified DOPC samples was consistent with an $L_\alpha$ phase, although the 4.4 Å chain-chain spacing was smaller than expected, indicating slightly tighter chain packing. This suggests that the kink caused by the *cis* double bond is sufficient to prevent conformational reorganization of the chains

into a gel phase during vitrification, although some degree of ordering does occur. This important study raises a caveat to interpreting cryo-EM images of lipid membranes due to the relative timescales of lipid motions with respect to cryo-preservation, discussed in more detail below.

### 2.3.2 Detailed bilayer thickness investigation of model lipid membranes using cryo-EM

Tahara et al. were the first to demonstrate the sensitivity of cryo-EM to sub-nanometer changes in average bilayer thickness using vesicles composed of PC lipids vitrified from room temperature.[82] For each composition, thickness histograms were constructed by measuring the distance between the high-density lines at 4 nm intervals around the projected vesicle circumference. Vesicles composed of the unsaturated lipid DOPC were visually uniform with a correspondingly narrow thickness distribution. In contrast, thickness distributions for the saturated acyl chain species DLPC, DMPC, and DPPC were broad, reflecting variability within individual vesicles that was clearly visible in images. The observations of (a) smooth DOPC vesicles and (b) faceted saturated lipid vesicles were consistent with the findings of Lepault et al. a decade earlier and suggest either an incomplete transition to $L_{\beta}$ or a full transition to $L_{\beta'}$ for DLPC and DMPC during vitrification (the lack of electron diffraction data precludes a definitive interpretation). Though not commented on by the authors, vesicles of the mixed-chain lipid POPC were visually heterogeneous, and the width of the POPC thickness distribution was intermediate between that of DOPC and the saturated lipids.

Although the thickness distributions for saturated lipids were broad, their averages showed a linear relationship between acyl chain length and thickness (Fig. 2.1a, solid black squares) that is consistent with trends in the bilayer headgroup-to-headgroup distance measured by X-ray scattering.[83] These comparative data are shown in Fig. 2.1a for saturated lipids in the $L_{\beta'}$ phase (open blue squares) and $L_{\alpha}$ phase (open red squares). Interestingly, the addition of 30 mol% cholesterol to each of the saturated lipids produced visually uniform vesicles and narrowed the thickness distributions. This observation is consistent with the known influence of cholesterol on saturated lipid bilayers above their $T_M$: cholesterol orders the chains, converting the $L_{\alpha}$ phase to an $L_o$ phase in which the

chains are in an all-trans conformation and therefore would not be sensitive to further straightening during vitrification. The average thickness of cholesterol-containing DLPC and DMPC bilayers was slightly larger than the non-cholesterol-containing bilayers, reinforcing that the non-cholesterol-containing bilayers undergo an ordering transition during vitrification. More recently, a cryo-EM study by our group found a linear trend between chain length and thickness for unsaturated PC lipids (Fig. 2.1b, solid black circles) in agreement with the trend reported from a joint analysis of SANS and SAXS data Fig. 2.1b, red circles[67].

Despite similar thickness trends, the data compiled in Fig. 2.1 reveal significant differences in absolute thicknesses measured by cryo-EM and scattering methods. Even though the physical origin of both measurements is electron density variation across the bilayer, a direct comparison is inherently problematic for several reasons. In the case of X-ray scattering, the bilayer's electron density profile is directly connected to the reciprocal space scattering intensity through a 1D Fourier transform and is thus relatively straightforward to extract through a modeling procedure. In contrast, the electron density imaged with cryo-EM is transformed by 2D projection and corrupted with a contrast transfer function (CTF) that itself depends on parameters such as the electron energy and chosen defocus length; changing these parameters can change the apparent thickness. In principle, these complications can be computationally reversed to recover the true electron density profile (and thus, a thickness that is directly comparable to values measured with scattering), but this relies on sufficiently spherical vesicles and an accurate estimation of the CTF. In practice, recovered density profiles are broader than those derived from scattering experiments and become comparable only after smearing the latter with a Gaussian of 5-6 Å standard deviation, implying a substantially lower resolution of cryo-EM-derived profiles and a loss of fine structural features.[86] More importantly, even if high-resolution, de-smeared profiles could be obtained from cryo-EM data, the vitrification-induced chain ordering described above would preclude an exact correspondence between transverse structural parameters (including thicknesses) derived from cryo-EM and scattering data.

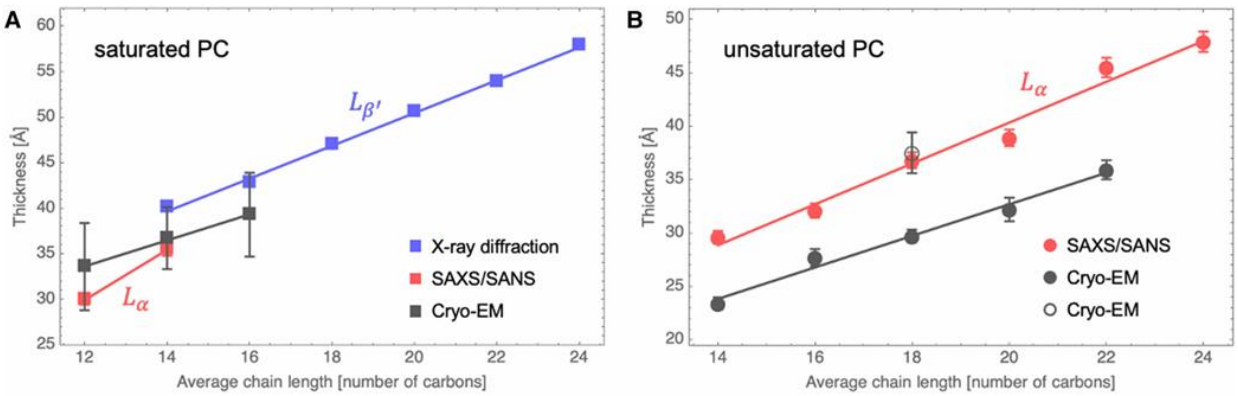


**Figure 2.1 Cryo-EM is sensitive to bilayer thickness.**[26] Bilayer thicknesses measured by cryo-EM compared with scattering techniques for saturated ((a)[82]) and unsaturated (b) PC lipids (open circle[82], closed circles[67]). For scattering-derived thicknesses of saturated lipids, 12:0-PC and 14:0-PC in the $L_\alpha$/Ld phase were measured at 30°C[77], 14:0-PC in the $L_{\beta'}$ phase was measured at 10°C[83], and all other lipids were measured in the $L_{\beta'}$ phase at 25°C[84]. For scattering-derived thicknesses of unsaturated lipids, thickness values in the $L_\alpha$ phase were measured at 30°C[85].

Despite these caveats, cryo-EM is clearly sensitive to composition-dependent differences in membrane thickness at the level of a few angstroms. In the following section, we describe recent efforts that exploit this sensitivity as a contrast mechanism for detecting tertiary structure in vesicles composed of lipid mixtures.

### 2.4 Timescales of vitrification and lipid motions

The results presented in the previous section highlight the importance of the timescales of various lipid motions relative to the vitrification time for cryo-preserving samples, demonstrated schematically in Figure 2.2. The temperature of a thin sample plunged into liquid ethane drops at a rate of $10^5 - 10^6$ K/s.[87] Accounting for the exponential decrease in lipid motional rates with decreasing temperature[88], motions with μs or faster correlation times may occur to an extent that would measurably alter membrane structure as cooling proceeds. Among the fastest motions is trans-gauche isomerization in the lipid chains that occur with a characteristic timescale of 10-100 ps at biological temperatures.[89] Indeed, the Lepault[81] and Tahara[82] results for saturated lipids above $T_M$ suggest that the cooling rate, while fast, nevertheless allows for the ordering of lipid chains through gauche-to-trans isomerization that drives the bilayer into the gel phase. This raises the question: why was the untilted $L_\beta$ phase observed with electron diffraction, rather than the tilted $L_{\beta'}$ phase that forms when these bilayers are slowly cooled through $T_M$?[81] Though not speculated by the authors, a possible answer is that the slower dynamics of axial rotation and wobble that would be required to convert the nascent $L_\beta$ bilayer to $L_{\beta'}$ are effectively frozen out or at least significantly hindered early in the cooling process. While the factors discussed above can lead to artifacts in membrane secondary structural features, a different set of dynamics must be considered for understanding the potential influence of vitrification on membrane tertiary structure, where the timescale of lipid lateral diffusion is key. Potential vitrification-induced artifacts (i.e., cooling-induced demixing or other changes in domain composition or structure) would require sufficient time for lipids to sample their translational degrees of freedom. The diffusion distance of lipid during vitrification can be estimated from published values of the temperature dependence of lipid diffusion coefficients and vitrification cooling rates noted previously.[88]

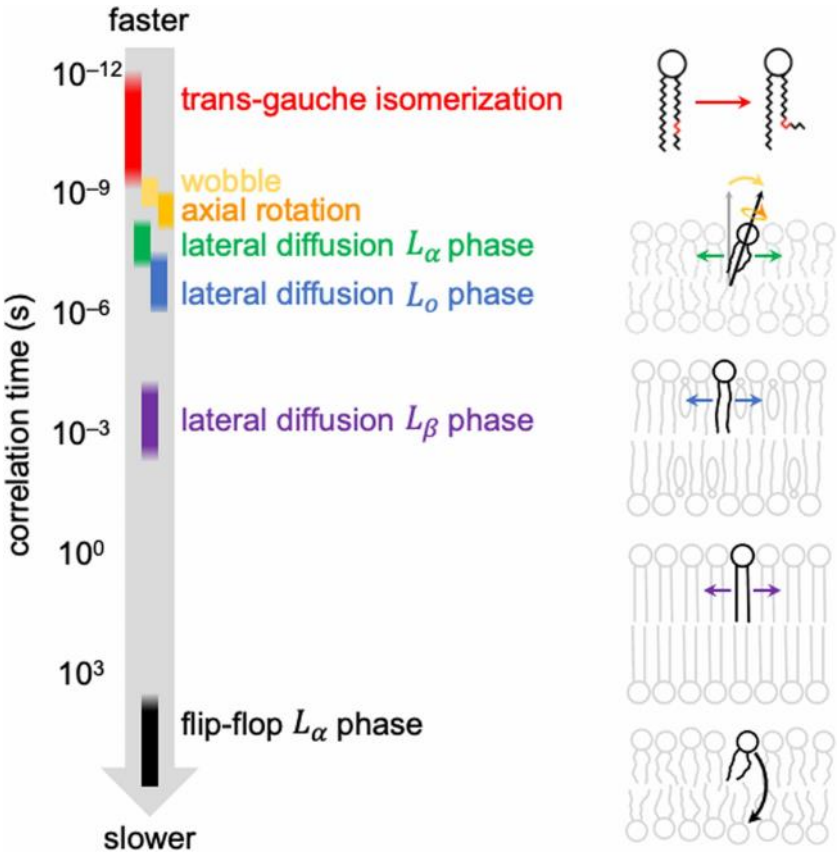


**Figure 2.2. Timescales of lipid motions.**[26] Correlation times of various lipid motions relevant to the vitrification timescale as discussed in the text. Lateral diffusion correlation times are calculated from published diffusion coefficients[88] as the time required for a mean squared displacement of 1 nm (i.e. a distance corresponding to the nearest neighbor lipid exchange). Additional references: trans-gauche isomerization[89], wobble, and axial rotation[90], and flip-flop[91].

Such estimates produce ranges of 5-20 nm depending on the composition and phase state of the bilayer immediately prior to vitrification. One inference is that a composition that is initially uniformly mixed but near a phase boundary in temperature could demix locally at the onset of cooling. The maximum cluster size that could result from this is half the diffusion distance estimate or ~ 2.5-10 nm. This suggests that the lateral organization of lipids in a mixture should be essentially preserved in a vitrified sample, possibly with local lipid reorganization at domain boundaries. It also suggests that the lateral structure should be visible in a cryo-EM image provided there is a sufficient difference either in thickness or electron density of coexisting membrane phases.

### 2.5 Tertiary bilayer structure from cryo-EM images

#### 2.5.1 Visualizing nanodomains using cryo-EM

The first studies to provide visual evidence of membrane phase coexistence were published simultaneously in 2020. In one of these studies, our group used cryo-EM for direct probe-free imaging of domains in vitrified biomimetic and biological membranes.[67] To probe lateral heterogeneity, bilayer thickness was measured at 5 nm increments around the projected vesicle circumference and binned to produce thickness histograms similar to the analysis of Tahara et al.[82] A comprehensive explanation of thickness measurements for the vesicles is provided in section 2.6. As noted above, a consistent increase in average bilayer thickness with increasing chain length was found for single-component bilayers of unsaturated lipids (Fig 2.3). The same analysis was then applied to vesicles of a canonical domain-forming model membrane mixture, DPPC/DOPC/cholesterol (40/40/20), revealing a bimodal thickness distribution consistent with phase separation. The thickness difference between the two peaks of the distribution was 6.3 Å, consistent with the thickness difference of $L_o$ and $L_d$ phases measured with X-ray and neutron scattering.[57, 92] Importantly, similar analyses performed on giant plasma membrane derived vesicles (GPMVs) isolated from eukaryotic cells provided the first direct visualization of phase separation in bilayers derived from the complex lipid mixture of mammalian plasma membranes.

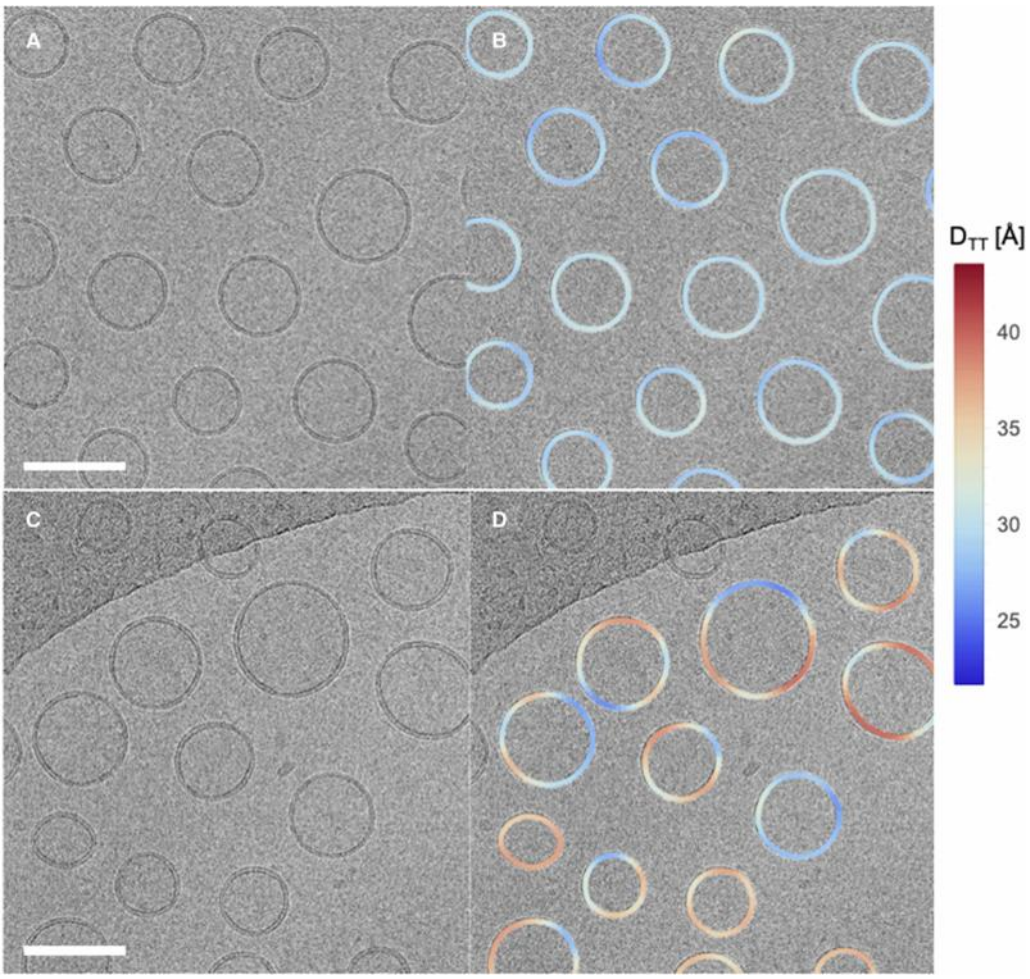


**Figure 2.3. Lateral phase separation in cryo-EM images.**[26] (a and b) a field of DOPC vesicles exhibiting a uniform thickness distribution centered at 29.7 Å. c and d, vesicles composed of DPPC/DOPC/POPG/Chol 40/35/5/20 show a bimodal distribution with peaks at 28.7 Å and 36.1 Å. Scale bars are 100 nm.

### 2.5.2 Visualizing nanodomains using cryo-ET

In a parallel study, Cornell et al. developed two visualization methods to characterize and analyze nano-sized domains in cryo-preserved vesicles composed of ternary mixtures of DPPC, diphytanoyl-phosphocholine, and cholesterol.[93] They employed cryo-electron tomography for data acquisition to generate 3D reconstructions of isolated vesicles. They then measured the bilayer thickness through a central slice of the tomograms by analyzing pixel-by-pixel profiles of filtered and edge-detecting algorithms. Similar to the results of Heberle et al., the thickness of the bilayers with Lo composition was larger compared to that of vesicles with Ld composition.[67] In the second method, a visual tag was produced using a trimer of the fluorescent protein mCherry that was targeted to the Ld domain by binding the His-tagged mCherry construct to Ni-NTA-dioleoylglycerosuccinylimino-diacetic acid (a lipid that preferentially distributes to Ld domains). This creative approach enabled the visualization of macroscopic domain formation with fluorescence microscopy to confirm phase separation. Parallel samples processed by cryopreservation and cryo-tomography revealed a “brush” of electron density representing his6-mCherry molecules evident along portions of the bilayers thought to represent Ld phases. This use of protein density targeted to unique domains is one of several potential ways to increase contrast in the electron microscopic images that is yet to be fully exploited. Importantly however, acknowledged by the authors, is that the probes themselves can have unpredicted impacts on lipid packing density, or their physical/chemical properties.

## 2.6 Intensity profiles and bilayer thickness measurement

Within projection images, the first step is locating the vesicle contours. In this first study, the vesicle contours were manually drawn.[67] The contours were smoothed and subdivided to obtain spatially resolved intensity profiles in the direction normal to the bilayer, referred to here as $I(w)$ profiles, with $w = 0$ corresponding to the bilayer midplane (Fig 2.4). For each polygon face, all pixels within a 5×20 nm rectangular region of interest centered at the face were selected, and their intensities binned at 1 Å intervals in the long dimension (i.e., normal to the face) and subsequently averaged in the short dimension to produce a local $I(w)$ profile. One of the unusual features of a local $I(w)$ profile is its

asymmetry across the bilayer midplane. Two separate and independent mechanisms potentially contribute to the asymmetry observed in $I(w)$ profiles of spherical lipid vesicles. The first mechanism is asymmetry due to differences in lipid packing between the inner and outer bilayer leaflets, which is unlikely to be important for vesicles larger than 50 nm in diameter. The second (and likely dominant) mechanism is a consequence of the spherical geometry of the vesicle. When the 3D phase shift density is projected onto a 2D plane, it leads to a radially averaged $I(w)$ profile that displays inherent asymmetry across the bilayer midplane. This asymmetry persists even if the electron phase shift density is assumed to be uniform throughout the vesicle.

A key measurement obtained from $I(w)$ is the spatially resolved bilayer thickness $D_{TT}$, details of which are provided in previous work.[67] Briefly, $D_{TT}$ was calculated as the distance between the two minima in $I(w)$. Two methods were used to locate the minima: (1) a 'model-free' method, in which a local 5-point Gaussian smoothing was first performed, and the distance between the two absolute minimum intensity values on either side of $w = 0$ was calculated; (2) a 'model-fit' method that fits the profile as a sum of four Gaussians and a quadratic background, with the troughs corresponding to the two absolute minimum intensity values on either side of $w = 0$. The two methods generally agree to within 1 Å, and the $D_{TT}$ values reported were the average of the two measurements.

### 2.7 Optimization of cryo-EM experimental conditions

The initial study by our group demonstrated the potential of cryo-EM in assessing membrane structure based on bilayer thickness.[67] In the following study, a wide range of parameters that need optimization and the development of specialized analytical tools are discussed.[94] The goal of the study was to minimize artifacts and maximize the information content obtained from the cryo-EM images of lipid bilayers. There are a few constraints in this methodology that should be noted. First, no two vesicles exhibit the same profile in 2D projection images due to differences in diameter and curvature (impact of the size of the vesicle, discussed in detail in Chapter 3). Second, even in well-controlled vesicle preparation, the size of domains varies among individual vesicles (heterogeneity in vesicle composition, discussed in detail in Chapter 4).

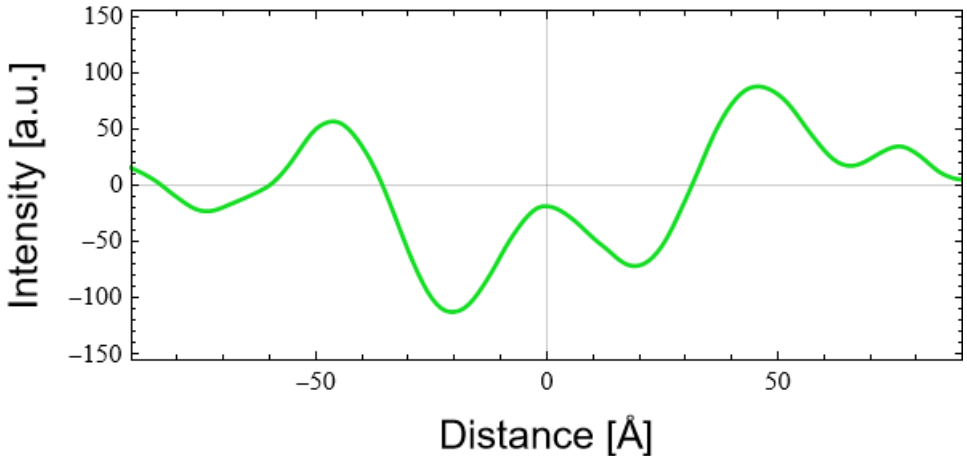


**Figure 2.4 Example bilayer intensity profile obtained from cryo-EM images of liposomes.** Intensity profiles where distance ($w$), $w = 0$ corresponds to the bilayer midplane.

Third, the vesicles are cryo-preserved in random orientations relative to the electron beam. This further increases the heterogeneity in the projection of domains in the vesicle images. On top of these constraints, instrument parameters such as electron dose, defocus length, and energy filtering contribute to differences in signal intensity and contrast-to-noise ratios in different samples. Finally, postprocessing steps including high-pass filtering, phase-flipping, and contrast transfer function corrections also have an impact on final analysis.

To prevent specimen damage and maintain accurate membrane thickness measurements, the total electron dose should remain below 20 $e^{-}/Å^{2}$. An underfocus of 2 μm is recommended to achieve good contrast without causing smearing or introducing artifacts such as blurring or defocus gradient. Energy filtering of primary data did not show significant benefits for membrane analysis. Image processing techniques such as high-pass filtering and phase-flipping improved data quality and contrast-to-noise ratio and are thus recommended.[94]

### 2.8 Closing the gap: Exploring lipid bilayers with cryo-EM

#### 2.8.1 Untapped potential: Lipid bilayer structure elucidation

In a relatively short time, cryo-EM has contributed enormously to solving high-resolution structures of isolated proteins and protein assemblies in vitro and in situ, but its application to the study of membrane structure has lagged. This is despite work decades ago, highlighted in this chapter, that provided tantalizing hints of its potential. After a hiatus, recent advancements in cryo-EM instrumentation and automation—combined with interest sparked by the debate over the existence of lipid rafts—have brought the analysis of membrane structure back to the forefront. Our group and others have demonstrated that cryo-EM can resolve differences in membrane thickness as small as a few angstroms in synthetic or biologically derived vesicles.[67, 93] Further, the thickness and contrast differences between ordered and disordered domains can be reliably discerned. These efforts have provided the first visual evidence of nanoscopic phase separation in unsupported lipid bilayers and paved the way for new investigations.

### 2.8.2 Seeing is believing

To take one example, a debate has emerged within the field of membrane biophysics regarding the physical origin of nanoscopic domains. Among the proposed explanations are curvature-induced microemulsions,[95] first-order phase coexistence,[96] line active lipids,[97] and Ising-like critical fluctuations,[98] but experimental data for testing these theories is scant as few techniques have the resolution needed to detect nanoscopic structure. The real-space images of nanodomains provided by cryo-EM should enable direct determination of correlation functions that are the signatures of the underlying physics. Establishing a robust cryo-EM workflow for characterizing these domains as a function of composition and liposome size will likely lead to new insights from synthetic vesicle studies.

Among the most significant challenges remaining is to apply these (and other) tools to the investigation of rafts in the membranes of living cells. Remarkably, the existing tools for imaging and analysis can be applied to cryo-preserved cells grown directly on EM grids. Our group has had success in imaging organelle structure in the processes of cryo-preserved cells and neurons (Figure 2.5).[71] Despite the greater complexity of cellular membranes, these initial efforts clearly identify thickness differences among membranes of different organelles and the plasma membrane. Existing tools for analysis are presently being employed to quantify these differences.

### 2.8.3 Potential advancements

Several potential advancements further brighten the outlook for cryo-EM applied to membrane structure. Data acquisition parameters continue to be refined, and existing hardware such as energy filters can reduce noise in the images that degrades contrast.[94] Even larger gains may be within reach with the use of Volta phase plates that have the potential to significantly increase image contrast. There also remain significant opportunities in image restoration and analysis to extract the maximum amount of information from cryo-EM experiments. Image restoration involves post-processing steps to restore the image of the original object by correcting for artifacts introduced by phase-contrast imaging in the electron microscope.

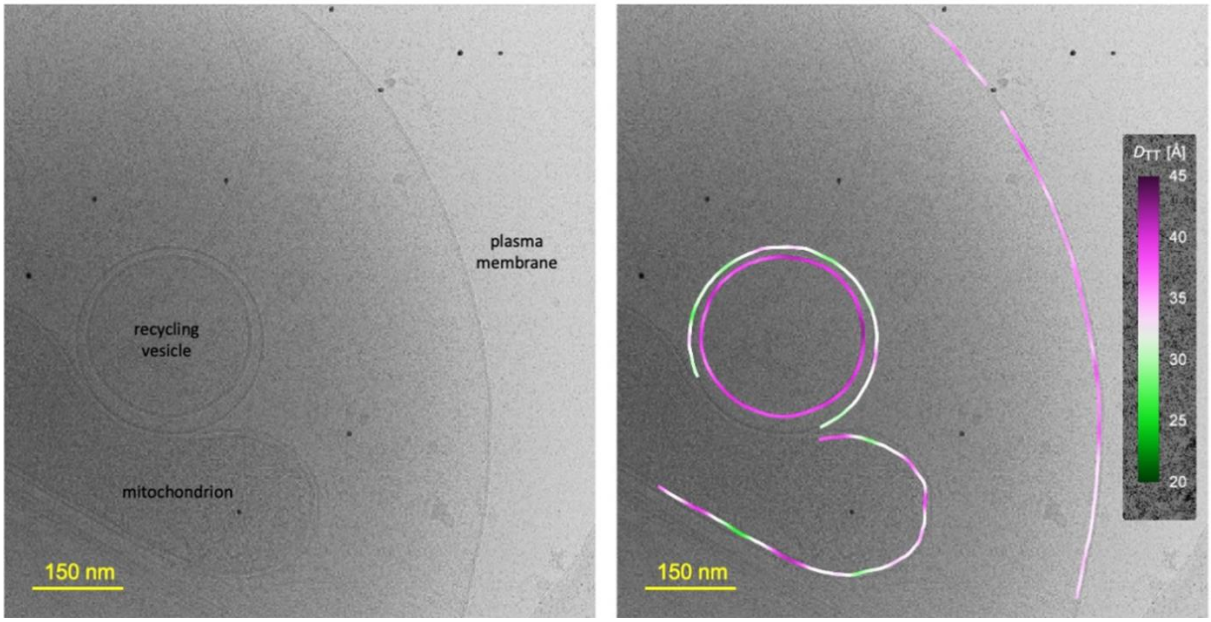


**Figure 2.5. Imaging membranes of cryopreserved cells with cryo-EM.[26]** Example image of an area of a hippocampal neuron cryopreserved after 10 days of growth from plating directly on an EM grid.[71] The image on the left identifies the plasma membrane, a vesicle, and a mitochondrion at the edge of a neuronal process. Using methods developed by Heberle et al.,[67] the thickness of the membrane was determined in each of the membranes and is displayed in the pseudo-colored overlays on the right.

These are well-established techniques in the single particle reconstruction field and can be easily applied to optimize images of vesicles or cellular membranes for subsequent analysis.[99] Perhaps most exciting is the potential to employ machine learning algorithms to help automate analyses. These automated methods were in the following chapters for analysis. Further developments in training networks to recognize contrast and thickness differences (or both) in lipid bilayers has immense potential for high throughput analyses with an associated increase in statistical power. These advancements, either separately or in tandem, should further enhance the ability to discriminate boundaries between ordered and disordered phases and refine the ability to differentiate domains on the spatial scale of nanometers.

There are also unique opportunities in sample preparation that have yet to be fully exploited. Strategically employed lipids tagged with contrast-enhancing properties (Br, I, gold, or other electron-dense elements) have the potential to further increase contrast. Finally, environmentally controlled automated sample preparation has yet to be fully exploited. Control of temperature is fundamental to the study of bilayer properties and present semi-automated blotting apparati exist to provide this control. In addition, avoiding the step of blotting with filter paper to reduce sample thickness before vitrification can now be avoided. Jet vitrification of thinly painted samples in well-controlled environmental chambers has the potential to further improve sample preparation. The combination of creative sample preparation and vitrification, high-throughput data acquisition in optimally configured cryo-EM microscopes, and advances in image processing will all be employed to lead the field of membrane structure and biophysics forward.

# Chapter 3

## Simulated cryo-EM images of phase separated lipid bilayer vesicles analyzed with a machine learning approach

A version of this chapter was originally published by Karan D. Sharma, et al.: Sharma, K. D.; Doktorova, M.; Waxham, M. N.; Heberle, F. A. Cryo-EM images of phase separated lipid bilayer vesicles analyzed with a machine learning approach. *Biophysical Journal* **2024**. K.S., M.D., M.N.W., and F.A.H. designed the research. M.D. performed molecular simulations. F.A.H. generated the synthetic datasets. K.S. and F.A.H. analyzed the datasets. K.S., M.D., M.N.W., and F.A.H. wrote the manuscript.

### 3.1 Abstract

Lateral lipid heterogeneity (i.e., raft formation) in biomembranes plays a functional role in living cells. Three-component mixtures of low- and high-melting lipids plus cholesterol offer a simplified experimental model for raft domains in which a liquid-disordered (Ld) phase coexists with a liquid-ordered (Lo) phase. Using such models, we recently showed that cryogenic electron microscopy (cryo-EM) can detect phase separation in lipid vesicles based on differences in bilayer thickness. However, the considerable noise within cryo-EM data poses a significant challenge for accurately determining the membrane phase state at high spatial resolution. To this end, we have developed an image processing pipeline that utilizes machine learning (ML) to predict the bilayer phase in projection images of lipid vesicles. Importantly, the ML method exploits differences in both the thickness and molecular density of Lo compared to Ld, which leads to improved phase identification. To assess accuracy, we used artificial images of phase-separated lipid vesicles generated from all-atom molecular dynamics simulations of Lo and Ld phases. Synthetic ground truth datasets mimicking a series of compositions along a tieline of Ld+Lo coexistence were created and then analyzed with various ML models. For all tieline compositions, we find that the ML approach can correctly identify the bilayer phase with > 90% accuracy, thus providing a means to isolate the intensity profiles of coexisting Ld and Lo phases, as well as accurately determine domain size distributions, number of domains, and phase area fractions. The method described here provides a framework for characterizing nanoscopic lateral heterogeneities in membranes and paves the way for a more detailed understanding of raft properties in biological contexts.

## 3.2 Introduction

The membranes that surround and partition living cells can play both structural and functional roles. The latter is exemplified by the lipid raft hypothesis, which proposes the existence of plasma membrane (PM) domains enriched in sphingolipids and cholesterol that are thought to direct the spatial organization of membrane proteins and thus mediate processes such as cell signaling.[19] Multiple lines of evidence have converged on a picture of raft domains as small (< 20 nm) and highly dynamic in resting conditions but with the ability to coalesce into larger structures in response to certain stimuli.[80] The structural and elastic properties of the raft and non-raft environments can differ substantially, with the latter being thinner, easier to bend, less viscous, and more compressible owing to a greater proportion of unsaturated lipids.[57, 100, 101] These local membrane properties influence the free energy of protein conformations and can result in distinct phase preferences for different proteins.[4, 102] In the raft model of PM organization, the size, connectivity, and composition of both raft and non-raft domains are all variables that can affect the local concentrations of membrane proteins and thus, the frequency of encounters between interaction partners.

One of the great challenges in studying lipid rafts is their small size, which precludes direct observation by conventional optical microscopy. Instead, researchers have relied heavily on biochemical and spectroscopic data to infer the presence or absence of multiple membrane environments in cell membranes. While the lack of visual evidence initially provided fuel for controversy, those concerns have been largely put to rest by the sheer quantity of indirect data that consistently points toward heterogeneous membranes as a rule rather than an exception.[51] Yet even as the "seeing is believing" debate recedes into the background, a fact often lost in the discussion is that the utility of image data extends far beyond visual confirmation of rafts. To take one example, images can reveal spatial domain patterns that might help distinguish between competing theories of raft formation.[103] Image data also opens a window to heterogeneity in domain structures that are often obscured in ensemble-averaged spectroscopic or scattering measurements, thus providing a more complete picture of rafts and their role in specific biological processes.

The great wealth of information contained in sub-optical images is exemplified by the emergence of single-particle cryo-electron microscopy (cryo-EM) as a pre-eminent tool in structural biology. A crucial breakthrough that has accelerated its rise is the use of machine learning (ML) at multiple stages of the experimental workflow[104] including image denoising[105], particle picking[106], image segmentation[107], and 3D reconstruction[108, 109]. Far from being limited to water-soluble proteins, cryo-EM is increasingly being used to determine structures of membrane proteins in native or near-native environments.[110-114] As the focus of these studies has been fixed squarely on the protein, their membrane hosts have received less attention, yet bilayers also appear in images at a resolution high enough to observe density variation in the separate leaflets. This raises the possibility that, when visualized with cryo-EM, relatively thicker raft domains might be distinguishable from the thinner “sea” of mostly unsaturated lipids that surround them.

To this end, we recently developed a method for obtaining local intensity profiles along the projected circumference of lipid vesicles in cryo-EM images[67], which we then used to measure the local bilayer thickness at 5 nm lateral resolution in liposomes and vesicles derived from cell plasma membranes as well as HIV pseudoviral membranes[115]. When thicknesses from a large population of vesicles were plotted as a histogram, the appearance of the distribution (i.e., uni- or multi-modal) was consistent with the number of coexisting phases determined in independent experiments. Concurrently with our study, the Keller group performed similar analyses and reached similar conclusions using tomographic reconstructions of cryo-preserved liposomes.[93] These outcomes were expected since it is well established that ordered phases are 5-10 Å thicker than disordered phases.[57, 92, 116] However, while those studies demonstrated critical proof-of-principle for using cryo-EM to investigate lipid phase separation, its unique capabilities as an imaging technique have not yet been fully realized. Most importantly, the development of a robust, automated method for determining the membrane phase state with high spatial resolution would enable additional valuable characterization including domain size distributions and an assessment of heterogeneity within the sample.[26]

Although the local phase state of the membrane can in principle be determined from spatially resolved bilayer thickness measurements[67], in practice, this is hampered by the substantial noise inherent to cryo-EM images (Fig. 3.1)., which results in broad and overlapping thickness distributions for Ld and Lo phases. One consequence is that a relatively large portion of the projected bilayer cannot be unambiguously classified as Ld or Lo by thickness alone. However, bilayer thickness is not the only characteristic that distinguishes ordered and disordered phases. Equally important from the perspective of electron scattering in image formation is the difference in molecular packing density, which manifests as a greater intensity contrast for ordered phases compared to disordered phases.[94] Here, we show that ML models trained to recognize both thickness and intensity contrast can predict the local bilayer phase state with significantly greater fidelity than methods based on thickness measurements alone. Key to this conclusion is the use of *in silico* data that allows us to establish a ground truth for assessing the accuracy of phase determination for a variety of methods, including both unsupervised and supervised ML techniques. We also describe additional structural information that can be gleaned from segmented images such as phase area fractions, average intensity profiles of ordered and disordered phases, and measurements of domain size and number.

### 3.3 Analysis software

The analyses described in the following sections were implemented in Wolfram Mathematica 13.2 (Wolfram Research, Champaign, IL).

### 3.4 Molecular dynamics (MD) simulations of Ld and Lo bilayers

All-atom molecular dynamics simulations of three-component mixtures containing 1,2-distearoyl-sn-glycero-3-phosphocholine (DSPC), 1,2-dioleoyl-sn-glycero-3-phosphocholine (DOPC), and cholesterol were performed with NAMD[117] using the CHARMM36 force field parameters[118, 119]. Two compositions were simulated, corresponding to the endpoints of a tieline in the Ld+Lo region of the room temperature phase diagram (Fig.3. 2). Each bilayer contained 100 lipids per leaflet, 50 waters per lipid, and no ions, and was constructed and equilibrated with the CHARMM-GUI protocols.[120-122]

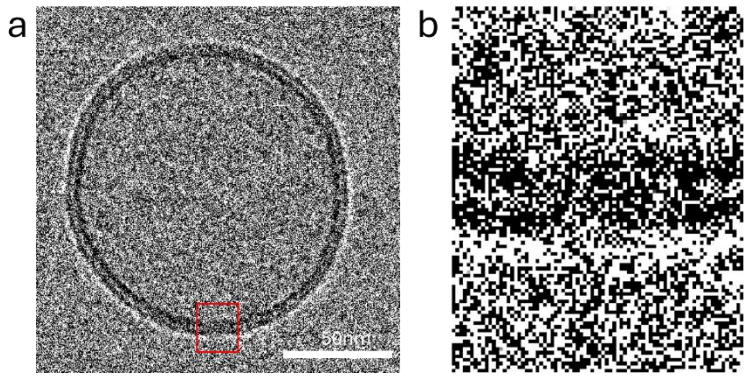


**Figure 3.1 Inherent noise in cryo-EM images.** a) The projected bilayer structure of a vesicle shows substantial noise in a Cryo-EM image. Clear bilayer boundaries are missing in some parts of the contour. b) A 20 nm zoomed-in segment of the vesicle. The dark and bright bands lack well-defined boundaries, making thickness estimation difficult.

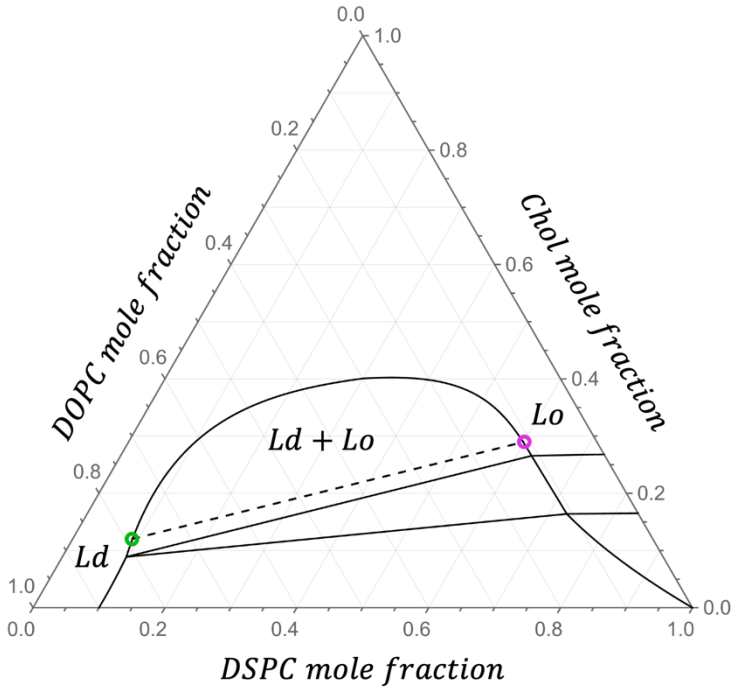


**Figure 3.2 Experimental phase diagram used in this study.** The 20°C phase diagram of DSPC/DOPC/Chol showing the Ld+Lo coexistence region and the Ld and Lo endpoints (green and magenta circles, respectively) of the tieline that passes through the composition $\chi_{DSPC} = 0.39$, $\chi_{DOPC} = 0.39$, $\chi_{Chol} = 0.22$.

The production runs for the two bilayers (917 ns for Ld and 1345 ns for Lo) were performed at constant temperature of 293 K and constant pressure of 1 atm using the same simulation parameters as in previous study.[123] Table 3.1 lists the compositions and some properties of the simulated Lo and Ld phase bilayers. Number and charge density profiles of each lipid and water atom in the systems were calculated from the last 480 ns of the centered bilayer trajectories with the Density Profile tool in VMD.[124] The dipole potential profile for each system was calculated from the charge density profile following the same approach in previous study.[125] The protocol is based on Poisson's equation and utilizes a double integral calculation, setting the potential to be the same on the opposite sides of the simulation box, which is a good approximation for symmetric bilayers.[126]

### 3.5 Generation of synthetic cryo-EM images

Synthetic cryo-EM images of lipid vesicles were generated following a previously described method that we summarize here.[67] In phase contrast imaging mode, the observed signal is related to variation in the electrostatic potential $\Phi$ within the lipid bilayer, which depends on lipid composition and packing density and is therefore different for Lo and Ld phases. We approximated $\Phi(w)$ (where $w$ denotes position along the direction normal to the plane of the bilayer) as a sum of contributions from individual lipid and water atoms with an additional contribution from the membrane dipole potential $\Phi_d$, i.e.,

$$\Phi(w) = \sum_i V_i \rho_i(w) + \Phi_d(w). \qquad (3.1)$$

In Eq.3.1, the sum is over individual lipid atoms, $\rho_i(w)$ is the atom's time-averaged atomic number density profile (units of $\text{Å}^{-3}$) calculated from the MD simulation trajectory, and $V_i$ is the spatially integrated, shielded coulomb potential for an isolated neutral atom ($V_i =$ 25, 130, 108, 97, and 267 $V\text{Å}^3$ for H, C, N, O and P, respectively). The phase shift experienced by an electron wave passing through the bilayer is given by:

$$g(w) = \sigma_e \Phi(w), \qquad (3.2)$$

where $\sigma_e$ accounts for the dependence of the electron phase on the projected potential and is equal to 0.65 $mrad\, V^{-1}\text{Å}^{-1}$ for 300 keV electrons.

**Table 3.1** Compositions and structural parameters of simulated Ld and Lo phases at 20°C.

| Mixture | $\chi_{DSPC}$ | $\chi_{DOPC}$ | $\chi_{CHOL}$ | $A_L$ [Å$^2$] | $D_B$ [Å] |
|---|---|---|---|---|---|
| Ld | 0.09 | 0.79 | 0.12 | 59.9 | 40.0 |
| Lo | 0.60 | 0.11 | 0.29 | 40.0 | 52.8 |

Following Wang et al., we refer to $g(w)$ as the electron 'scattering profile' of the flat simulated bilayer; as $\Phi$ has units of $V$, the scattering profile has units of $mrad\,\text{Å}^{-1}$.[86] A cryo-EM image of a liposome corresponds to a projection of the vesicle's spherical scattering profile, $\gamma(r,\theta,\phi)$, onto a plane, followed by convolution with a contrast transfer function (CTF). For a compositionally uniform and spherically symmetric liposome of radius $R$, $\gamma$ has no angular dependence and can be approximated with the flat bilayer scattering profile $g(w)$ using the coordinate transformation $r = w + R$, such that $\gamma(r,\theta,\phi) = \gamma(r) = g(r-R)$. In this case, the projected density $\Gamma(\boldsymbol{r})$ is easily obtained by the Abel transform:

$$\Gamma(\boldsymbol{r}) = 2\int_{\boldsymbol{r}}^{\infty} \frac{g(a-R)}{\sqrt{1-(r/a)^2}}\,da. \qquad (3.3)$$

Eq. 3.3 is not straightforward to evaluate for a phase-separated liposome where $\gamma$ may have a complicated angular dependence. Instead, we used a Monte Carlo technique to approximate $\Gamma(\boldsymbol{r})$. Briefly, a three-dimensional representation of the vesicle was constructed as a set of discrete points whose spatial density was proportional to $\Delta\gamma(r,\theta,\phi) = \gamma(r,\theta,\phi) - \gamma_s$, where $\gamma_s$ is the electron phase shift caused by vitreous ice under given imaging conditions and is equal to 3.28 $mrad\,\text{Å}^{-1}$ here. We used a geometrical model for the vesicle in which the Ld and Lo phases each comprised a single spherical cap centered on opposite poles of the vesicle. For this domain arrangement, the position of the domain boundary is specified by the polar angle $\theta_b = \cos^{-1}(1-2a_{Lo})$, where $a_{Lo}$ is the area fraction of the Lo phase. With the Lo and Ld domains centered at $\theta = 0$ and $\pi$, respectively, the azimuthally symmetric spherical scattering profile is

$$\gamma(r,\theta;R,\theta_b) = \begin{cases} g_{Lo}(r-R) & for\ 0 \le \theta < \theta_b \\ g_{Ld}(r-R) & for\ \theta_b \le \theta < \pi \end{cases}. \qquad (3.4)$$

To generate images of phase-separated vesicles, the vesicle radius was drawn from a Schulz distribution centered at 25 nm with a width of 5 nm, consistent with experimentally observed vesicle size distributions after extrusion through a 50 nm pore size filter. Random points were then generated within the Lo and Ld domains delineated by $\theta_b$ and further subdivided radially into thin (0.2 Å-width) concentric shells, with the shell radii $r_j$

chosen to span the full thickness of the simulated flat Lo and Ld bilayers. Within the Lo and Ld shells, the point density was proportional to $\gamma(r_j, \theta)$ given by Eq. 3.4, with the constant of proportionality chosen to generate a total of $\sim 10^8$ points in the vesicle. The full set of points thus generated was then randomly rotated in 3D, projected onto the $xz$ plane, and binned into 2.5 Å square pixels to create the image $\Gamma(\boldsymbol{r})$ where the intensity at each pixel was proportional to the density of projected points. At this step, the fraction of signal in each pixel originating from Lo and Ld domains was recorded and used to generate ground truth maps of the bilayer phase state in the projection image. These maps were subsequently used to assess the accuracy of machine learning analyses as described in the following sections.

To mimic experimental images, $\Gamma(\boldsymbol{r})$ must be convolved with a contrast transfer function (CTF) $c(\boldsymbol{s})$ and associated phase perturbation factor $\chi(\boldsymbol{s})$:

$$c(\boldsymbol{s}) = [\sin \chi(\boldsymbol{s}) - Q \cos \chi(\boldsymbol{s})] \exp(-B|\boldsymbol{s}|^2), \qquad (3.5)$$

$$\chi(\boldsymbol{s}) \approx -\pi\lambda\Delta Z|\boldsymbol{s}|^2 + \tfrac{\pi}{2} C_s \lambda^3 |\boldsymbol{s}|^4. \qquad (3.6)$$

In Eqs. 3.5-6, $\boldsymbol{s}$ is the spatial frequency, $B$ is the amplitude decay factor, $Q$ is the dimensionless amplitude contrast factor, $\lambda$ is the electron wavelength, $\Delta Z$ is the defocus length (defined such that positive values indicate underfocus), and $C_s$ is the spherical aberration coefficient. Figure 3.3 plots the CTF for our simulated parameter set (Table 3.2) with and without the spherical aberration correction term in Eq. 3.6, demonstrating that the effects of spherical aberration are negligible for simulated imaging conditions, and thus justifying our choice to omit the second term in Eq. 3.6 in our calculations. We also note our use of a single electron wavelength, which carries the implicit assumption of zero chromatic aberration. Although chromatic aberration exists in any real electron microscope, the effects can be partially corrected by energy filtering. We previously showed that energy filtering has minimal effects on bilayer intensity profiles that are used in the present analyses.[94]

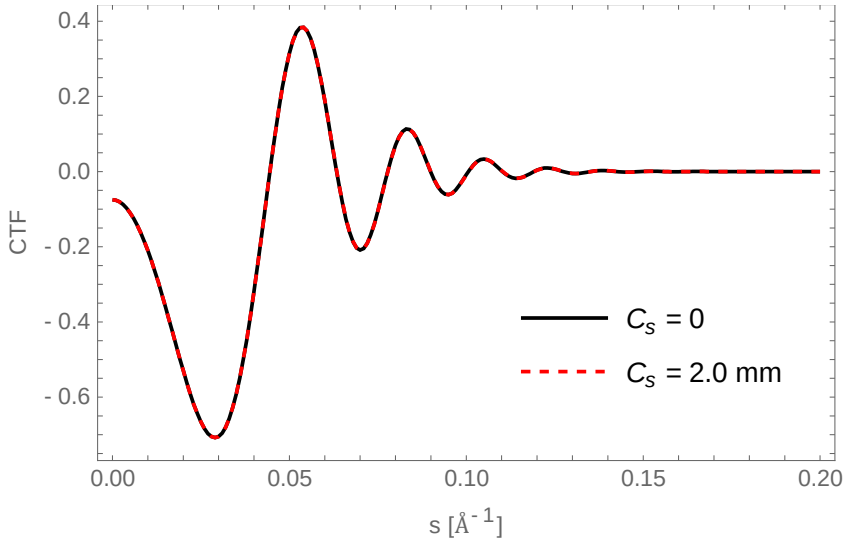


**Figure 3.3 Effect of spherical aberration on the contrast transfer function (CTF) for simulated imaging conditions.** The CTF (Eqs. 3.5-6 in Methods) is plotted using the simulated parameter set given in Table 3.2 and either $C_s$ = 0 (black solid line) or 2.0 mm (red dashed line). We note that, although spherical aberration has a negligible influence for these imaging conditions, the effect can be substantial for lower defocus values and larger magnifications.

**Table 3.2** Parameters used to generate simulated images (see Methods for details).

| *Electron* | | | *contrast transfer function* | | |
|---|---|---|---|---|---|
| Energy | $\lambda$ | $\Delta Z$ | $Q$ | $B$ | $m$ |
| 300 keV | 1.97 pm | 2.5 μm | 0.075 | 300 Å$^2$ | 400 |

Accounting for the effects of the CTF, the reciprocal space image is calculated as:

$$I(\boldsymbol{s}) \propto 1 + mc(\boldsymbol{s})\mathcal{F}_s[\Gamma(\boldsymbol{r})](\boldsymbol{s}), \qquad (3.7)$$

where $\mathcal{F}_s$ is the Fourier transform of the projected 2D phase shift image $\Gamma(\boldsymbol{r})$ and $m$ is a scale factor that adjusts the intensity contrast in the spatial domain (we define contrast as the difference between maximum and minimum values of bilayer intensity profiles. We chose a value of $m = 400$ that resulted in average contrasts of 85-110 a.u. depending on vesicle size and bilayer composition; these values are consistent with ranges observed in experimental images collected at 300 keV and 2.5 $\mu m$ underfocus. The corresponding real-space image $I(\boldsymbol{r})$ is the inverse Fourier transform of $I(\boldsymbol{s})$,

$$I(\boldsymbol{r}) = \mathcal{F}_r{}^{-1}[I(\boldsymbol{s})](\boldsymbol{r}). \qquad (3.8)$$

Finally, zero-mean and frequency-independent (i.e., white) Gaussian noise with a standard deviation of 120 a.u. was added to simulated images, resulting in final image contrast-to-noise ratios of ~ 0.7-0.9 that fall within the range of values observed in experimental images (~ 0.7-1.05) collected under the simulated conditions. The complete sequence of steps for generating synthetic images described in this section is graphically summarized in Fig. 3.4, while Fig. 3.5 demonstrates how the profiles depend on vesicle size. For the analyses presented here, a total of 1000 vesicle images were generated for each of the two tieline endpoint samples, and a total of 490 vesicle images were generated for each of the nine phase-separated compositions.

As shown in Fig. 3.6, intensity contrast in cryo-EM images of liposomes depends on both the bilayer phase state and the vesicle size. Our goal is to correct for vesicle size effects while preserving the component of the contrast that depends on phase state. To this end, we first fit the contrast vs. vesicle diameter data for the tieline endpoint datasets S1 (Fig. 6c green points) and S10 (Fig. 3.6c pink points) to quadratic functions; the best-fit curves are shown as solid lines in Fig. 3.6c. The contrast for each individual vesicle was then normalized by dividing by the best-fit contrast of a 50 nm diameter vesicle, which effectively collapsed the Ld and Lo data to a single curve as shown in Fig. 3.6d.

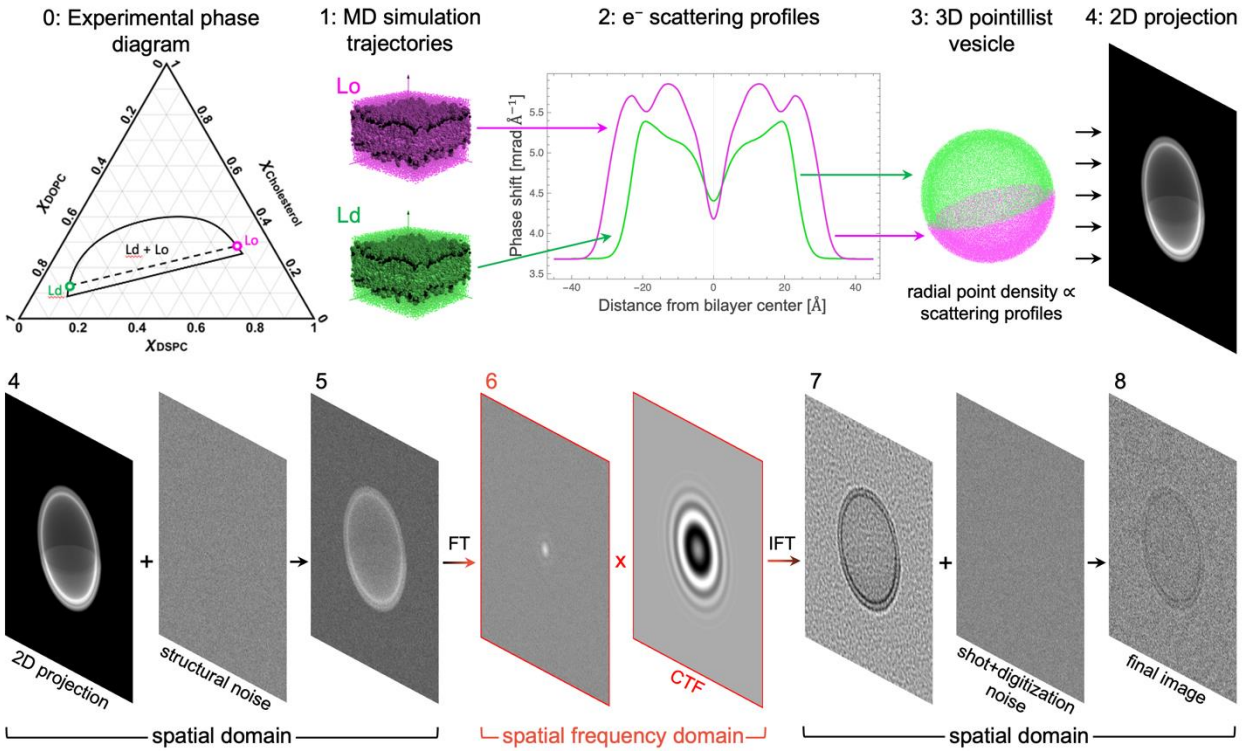


**Figure 3.4 Schematic of the workflow for generating synthetic cryo-EM images of lipid bilayer vesicles.** Step 0: The experimental phase diagram showing the Ld and Lo compositions (green and magenta circles, respectively). Steps 1 and 2: MD simulation trajectories are used to generate electron scattering profiles. Step 3: A 3D model of a phase separated vesicle is generated in which the density of points in each domain is proportional to the scattering profile of the respective phases. Step 4: the vesicle is rotated randomly about its origin (a single orientation is shown) and the points are projected onto a plane. Step 5: zero-mean Gaussian structural noise is added to the projection image. Step 6: the noisy projected image is Fourier-transformed and convolved with the instrument's contrast transfer function (CTF) in the spatial frequency domain. Step 7: the CTF-smeared image is inverse Fourier-transformed back to the spatial domain. Step 8: zero-mean Gaussian shot and digitization noise is added to produce the final image.

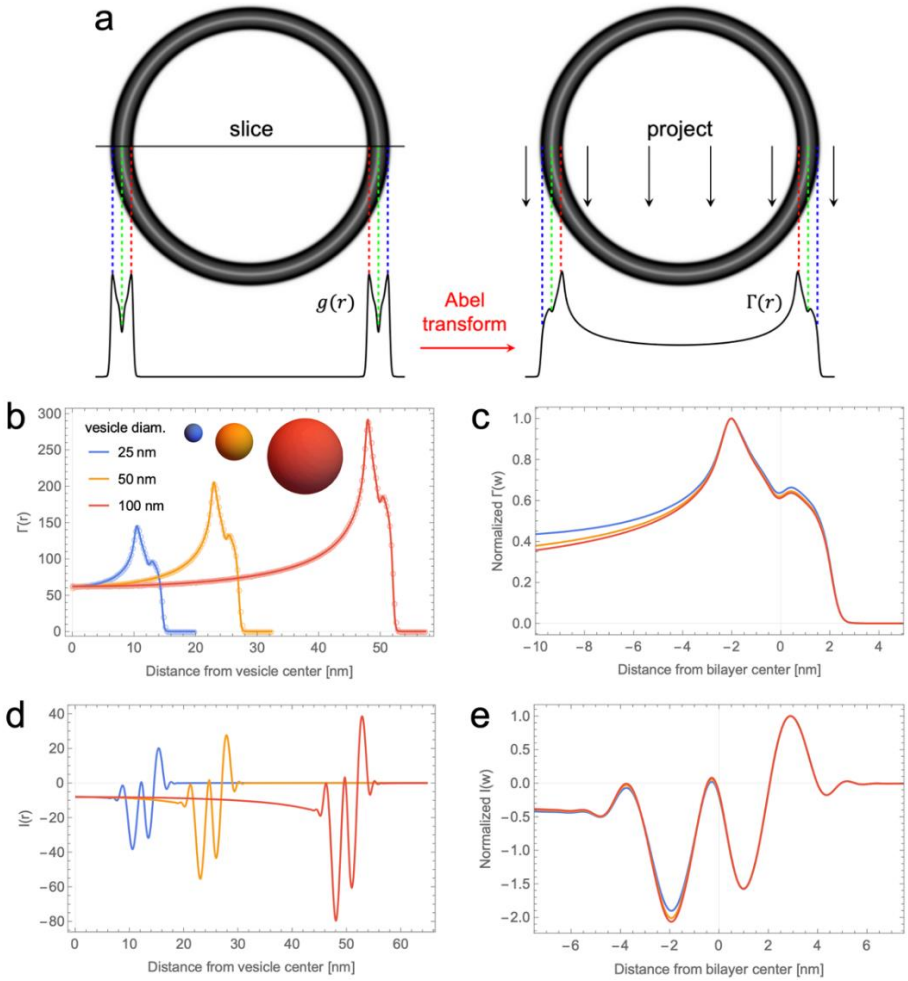


**Figure 3.5 Influence of vesicle size on projected intensity profiles.** (a) Schematic illustration of the Abel transform for a spherically symmetric liposome with electron scattering density indicated by grayscale shading. A slice through the vesicle corresponds to the 1D electron scattering profile $g(r)$, as shown on the left. The summed density of a slice corresponds to a point in the 1D projection $\Gamma(r)$, as shown on the right. Mathematically, $\Gamma(r)$ is the Abel transform of $g(r)$. (b) A comparison of $\Gamma(r)$ for three vesicle sizes calculated either by the Monte Carlo technique described in Methods (symbols) or by numerical integration of Eq. 3.3 (solid lines). (c) Profiles in panel b, after centering to bilayer midplane and normalizing to the height of the maximum peak, reveal differences as a function of vesicle size (see panel b legend). (d) CTF-corrupted intensity profiles $I(r)$ for the three vesicle sizes (see panel b legend), using CTF parameters in Table 3.2. (e) Profiles in panel d, centered and normalized, show minor differences for the smallest vesicle.

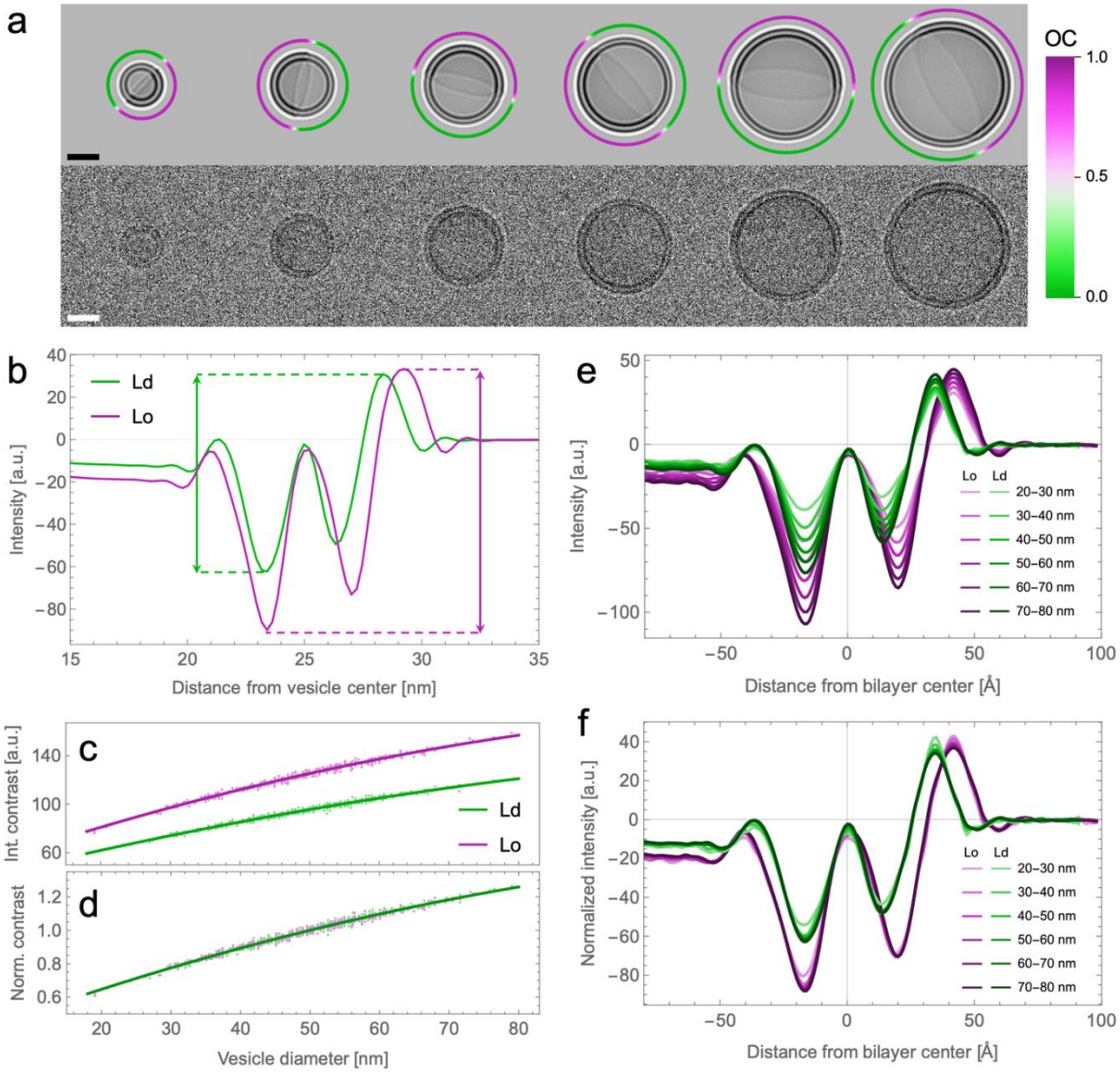
a
OC
1.0
0.5
0.0
b
Ld
Lo
Intensity [a.u.]
Distance from vesicle center [nm]
c
Int. contrast [a.u.]
Ld
Lo
d
Norm. contrast
Vesicle diameter [nm]
e
Intensity [a.u.]
Lo Ld
20–30 nm
30–40 nm
40–50 nm
50–60 nm
60–70 nm
70–80 nm
Distance from bilayer center [Å]
f
Normalized intensity [a.u.]
Lo Ld
20–30 nm
30–40 nm
40–50 nm
50–60 nm
60–70 nm
70–80 nm
Distance from bilayer center [Å]

**Figure 3.6 Influence of vesicle size on intensity contrast.** (a) Shown are pairs of images of selected vesicles from dataset S5. In each pair, the upper and lower images are before and after the addition of Gaussian noise, respectively. The ring surrounding the vesicle in the noise-free images plots the ground truth $OC$ value along the projected circumference as indicated by the color scale. Scale bar 20 nm. (b) Ground truth IPs for Ld (green) and Lo (magenta) phases of a 50 nm diameter vesicle. Internal contrast is defined as the intensity difference between the outer peak and inner trough as indicated in the figure. (c) Scatter plot of internal contrast for the 490 vesicles of the Ld (green) and Lo (magenta) datasets. The solid lines are the best fit to a quadratic function. (d) Data points from panel c after normalizing to the best-fit contrast of a 50 nm diameter vesicle. The solid line is the best fit to a quadratic function; the reciprocal of this function is used as a normalization factor in the IP pre-processing method as described in Methods. (e) Average IPs of Ld and Lo phases binned by size as indicated in the legend. (f) Average IPs of Ld and Lo phases after correcting for size.

This curve was then fit to another quadratic function, the reciprocal of which gives the appropriate scale factor for normalizing any vesicle (i.e., Ld, Lo, or phase separated) as a function of its measured diameter. This function was then applied to all training and testing data prior to ML analysis. Fig. 3.6 shows average IPs for different vesicle size bins calculated from datasets S1 and S10 before (Fig. 3.6d) and after (Fig. 3.6e) IP pre-processing, demonstrating the efficacy of this normalization procedure.

Within projection images, vesicles were identified and subdivided as previously described to obtain spatially resolved intensity profiles in the direction normal to the bilayer, referred to here as $I(w)$ profiles, with $w = 0$ corresponding to the bilayer midplane.[67] Briefly, vesicle contours (i.e., the set of points approximating the midplane of the projected bilayer as defined by a relatively bright central peak) were first generated using a neural network-based algorithm (MEMNET) developed and kindly provided by Dr. Tristan Bepler (MIT). While we retain the original MEMNET nomenclature, these algorithms (and others) are now part of the TARDIS software package.[127] The MEMNET contour was resampled at arc length intervals of ~ 5 nm, resulting in a polygonal representation of the 2D contour. For each polygon face, all pixels within a 5×20 nm rectangular region of interest centered at the face were selected, and their intensities binned at 1 Å intervals in the long dimension (i.e., normal to the face) and subsequently averaged in the short dimension to produce a local $I(w)$ profile.

### 3.6 Machine learning (ML) classification of bilayer phase state

We tested all previously discussed unsupervised and supervised learning methods for identifying the phase state of the bilayer, using the spatially-resolved IPs as features for discriminating Lo and Ld phases. Each profile can be considered as a 201-dimensional vector of intensities for input to the ML algorithm (where noted, the dimensionality of the input vectors was first reduced using principal component analysis). For unsupervised learning, we used k-means and k-medoids clustering with the number of clusters (k) set to two. For supervised learning, we used five methods as implemented in Mathematica v13.2: Decision Tree (DT), Gradient Boosted Trees (GBT), Random Forest (RF), Nearest Neighbors (NN), and Logistic Regression (LR). The default settingS for all the machine

learning methods in Wolfram Mathematica 13.2 were used for classification tasks. Additional details are provided below.

In DT, the CART algorithm was used for construction of the decision tree. The regularization parameter (specified as “DistributionSmoothing”) was set to 1. The fraction of features that are randomly selected for training (“FeatureFraction”) was set to 1.

In GBT, the LightGBM framework was used for classification. “BoostingMethod” was set to “Gradient”. The number of boosting rounds (specified as “MaxTrainingRounds”) was set to 50. The number of leaves (terminal nodes) in each tree of the ensemble (“LeavesNumber”) was set to 25. The minimum number of data samples in one leaf (“LeafSize”) was set to 15. The learning rate used in gradient descent (“LearningRate”) was set to 0.2. The maximum depth of each tree (“MaxDepth”) was set to 6. Both L1 and L2 regularization were set to 0.

In RF, the fraction of features that were randomly selected to train each tree (“FeatureFraction”) was set to $1/\sqrt{201}$, where 201 is the total number of features in each datapoint. The number of trees in the forest (“TreeNumber”) was set to 100. The maximum number of examples in each leaf (specified as “LeafSize”) was set to 2. The regularization parameter (specified as “DistributionSmoothing”) was set to 0.5.

In LR, the optimization method was the Limited memory Broyden-Fletcher-Goldfarb-Shanno algorithm (LBFGS). L1 Regularization was set to 0 and L2 regularization was set to 0.0001.

In NN, the method (specified as “NearestMethod”) was set to “Scan”. The regularization parameter (specified as “DistributionSmoothing”) was set to 0.5. The number of neighbors to consider (specified as “NeighborsNumber”) was set to 20.

Models were trained on IPs from vesicles in the pure Lo and Ld datasets, with vesicle sizes drawn from a uniform distribution to minimize size-dependent bias. As shown in Fig. 3.6, IP contrast depends on both the bilayer phase state and the vesicle size. Therefore, to maximize the ability of machine learning models to predict the former, is it necessary to account for the effects of the latter. We investigated two ways of addressing this issue: (i) In the “IP pre-processing” procedure (described in section 3.5), intensity profiles were

normalized prior to model training using an empirically determined scale factor that corrects for vesicle size-dependence. (ii) In the “size training” procedure, vesicle size was included as a second feature (along with the un-normalized IP) at the stage of model training. In both cases, trained models were then used to predict the phase state of IPs from the validation datasets.

### 3.7 Results and Discussion

#### 3.7.1 Model system and generation of image datasets

The primary inputs for generating images of phase separated vesicles are the electron scattering profiles of Ld and Lo phases, which we calculated from MD simulations as described in Methods. We chose the three-component mixture DSPC/DOPC/Chol as a model system because the room temperature phase diagram has been determined experimentally at high compositional resolution.[128, 129] As shown in Fig. 3.2, the phase diagram contains a region of coexisting Ld and Lo phases that serve as a model for lipid rafts. We simulated the endpoints of a tieline that includes the composition DSPC/DOPC/Chol 39/39/22 mol%, in part because this composition has been extensively studied with confocal microscopy[130], FRET[53], X-ray scattering[92], and neutron scattering[57]. The large line tension for this mixture results in essentially complete coalescence of domains in giant unilamellar vesicles that can be easily visualized with fluorescence microscopy, such that each vesicle has a single domain of each phase.

Table 3.1 lists bilayer structural parameters of Ld and Lo phases obtained from the molecular simulations. Most important for cryo-EM are the substantial differences in bilayer thickness $D_B$ and area per lipid $A_L$, the latter being inversely related to lipid packing such that the smaller $A_L$ of Lo phase indicates greater lipid packing density compared to Ld phase. The large differences in bilayer thickness and lipid packing result in markedly different electron scattering profiles for Ld and Lo bilayers, as shown in Fig. 3.5. We used these electron scattering profiles to generate image datasets as a function of Lo area percentage ranging from 0 to 100% in increments of 10%, as shown in Fig. 3.7, with the workflow for image generation demonstrated schematically in Fig. 3.5. Throughout the text, we refer to these compositions as S0-S10.

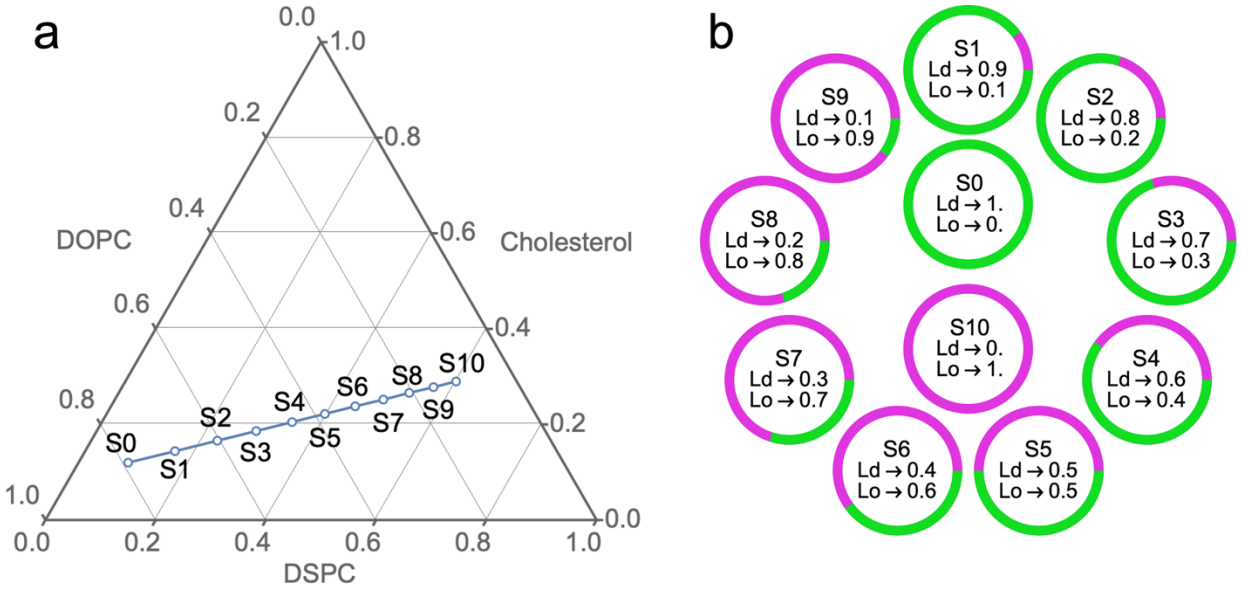


**Figure 3.7 Lipid compositions of synthetic image datasets.** (a) All compositions in this study lie on a thermodynamic tieline of the mixture DSPC/DOPC/Chol at 20°C (40). On this tieline, an Ld phase of fixed composition (S0) coexists with an Lo phase of fixed composition (S10) and only the relative amounts of Ld and Lo change. (b) The compositions S1-S9 represent a series of increasing Lo area percentage in increments of 10%.

For each composition, the size of individual vesicles was randomly drawn from a distribution consistent with extrusion through a 50 nm pore size filter and thus producing diameters ranging from ~ 20-80 nm. Each vesicle object was given a different random 3D orientation prior to projection. Projection images were convolved with a contrast transfer function (CTF) assuming an electron energy of 300 keV and using typical values for CTF parameters (Table 3.2). We note that a defocus range of 2.0-3.0 $\mu m$ was previously found to be optimal for determining bilayer thickness.[94] Figure 3.8 shows representative images from each simulated composition before and after the addition of white Gaussian noise. For most of the phase separated vesicles (i.e., S1-S9), distinct domains of different thickness and intensity are visible in the noisy images.

Datasets of noisy images were then analyzed to obtain intensity profiles (IPs) around the vesicle circumference at 5 nm resolution as detailed in Methods. Figure 3.9 compares the ground truth profiles (obtained by convolving the Ld and Lo electron scattering profiles with the CTF) to representative IPs obtained from synthetic images of pure Ld and Lo vesicles. The ground truth IPs of Ld and Lo phases (Fig. 3.9b) are characterized by significant differences in both the position and depths of the “troughs” on either side of the bilayer center. These features, which arise from differences in bilayer thickness and molecular packing density of Ld and Lo phases, are partially obscured by noise at 5 nm resolution but are precisely recovered when IPs from many segments are averaged (Fig. 3.9c-d). As we now describe, the spatially resolved IPs constitute the raw data that we used to classify the bilayer phase state.

### 3.7.2 Phase classification based on bilayer thickness

As a baseline for comparing the performance of machine learning methods, we employed a simple classification scheme for phase state based on bilayer thickness measured from segment IPs as described in Methods. Figure 3.10 shows probability distributions of segment thicknesses $D_{TT}$ for each dataset. As expected, the distributions are approximately Gaussian for the single-phase Ld and Lo datasets S0 and S10, while datasets S1-S9 show non-Gaussian character owing to Ld+Lo coexistence within the vesicles. The mean $D_{TT}$ was 29.7 Å for S0 and 35.8 Å for S10, closely matching the ground truth values of 30.6 Å and 36.4 Å for Ld and Lo phases, respectively.

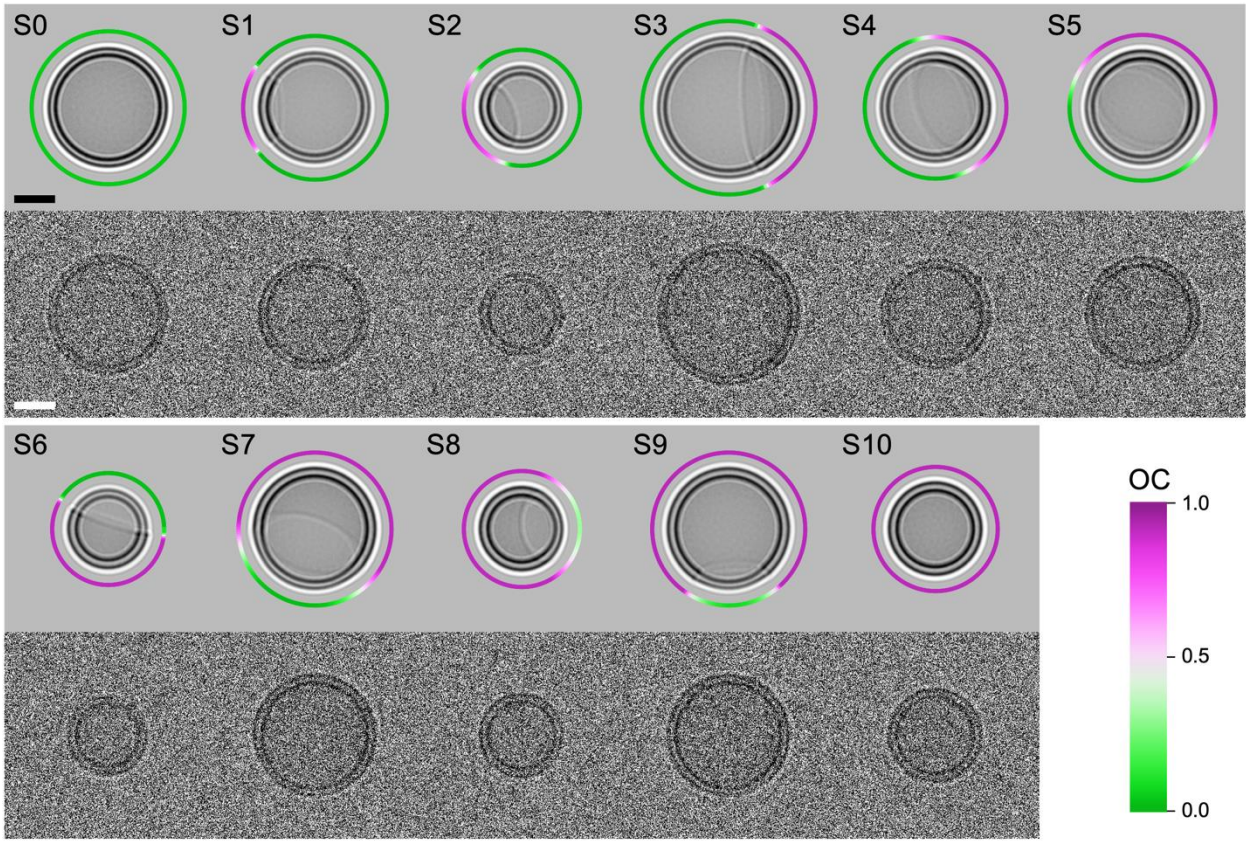


**Figure 3.8 Representative vesicle images.** A pair of images of a representative vesicle from each uniform (S0, S10) and phase separated (S1-S9) dataset is shown (see Fig. 3.7 for compositions). For each pair, the top and bottom images are before and after addition of Gaussian noise, respectively. The ring surrounding the vesicle in the noise-free images shows the angular dependence of the $OC$ value in the projection, which quantifies the fraction of signal arising from the Lo domain. Scale bar 20 nm.

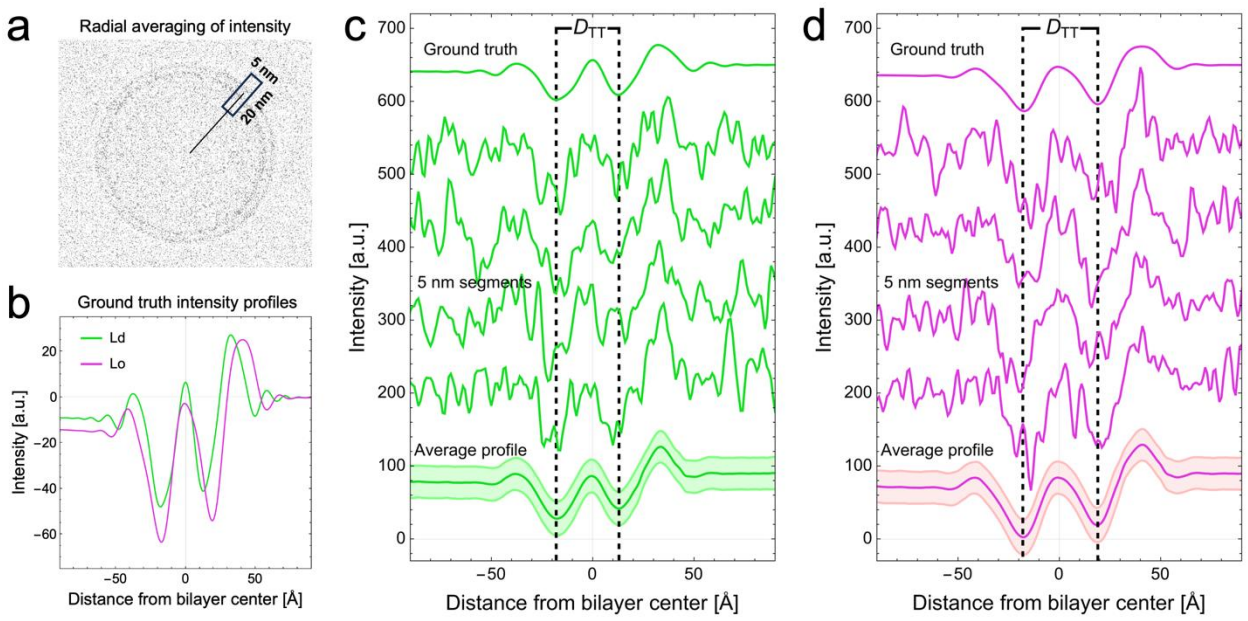


**Figure 3.9 Segment intensity profiles.** (a) Spatially resolved intensity profiles (IPs) are obtained by radial averaging of the intensity within segments of ~ 5 nm arc length centered at the projected vesicle contour. (b) Ground truth IPs of Ld and Lo phases show significant differences in the position and depth of the troughs on either side of the bilayer center. (c and d) Comparison of Ld (c) and Lo (d) IPs: ground truth (top), four randomly chosen 5 nm segments (middle), and the average of all segments in all vesicles (bottom, with shaded area denoting $\pm 1$ standard deviation). IPs in panels c and d are offset vertically for clarity.

Two different approaches used for thickness-based classification. A confounding problem for this classification scheme is the broad and overlapping $D_{TT}$ distributions of Ld and Lo phases, which precludes a straightforward determination of an appropriate cutoff, $D_{TT}^{*}$. For example, using the midpoint between the mean Ld and Lo $D_{TT}$ values (i.e., $D_{TT}^{*} = 33$ Å) resulted in an overestimation of the Lo percentage for samples S1-S6 and an underestimation for samples S8-S9 (Fig.3.10 left). This discrepancy is a direct result of the narrower distribution of measured $D_{TT}$ values for Lo compared to Ld segments. Using a larger value of $D_{TT}^{*} = 34$ Å maximized the overall accuracy of phase classification at the level of individual segments (Fig. 3.10 middle), achieving an average accuracy of 82% for all 11 systems. It is notable that no cutoff value was able to accurately predict phase area percentages for all tieline samples (Fig. 3.10), a fact that severely limits the utility of this approach to phase classification.

In the second approach, to classify the phase state of individual segments, we first fit the thickness distributions for the tieline endpoint datasets S0 and S10 to gaussians (Fig. 3.11, upper left). Thickness distributions for phase separated datasets S1-S9 were then modeled as a weighted sum of the endpoint gaussians (i.e., with the mean and standard deviation values fixed), and the obtained weights were used to calculate the phase fractions for each dataset, which resulted in excellent agreement with ground truth phase fractions (Fig. 3.11 and Table 3.3). For each dataset, the best fit phase fraction $f_{Lo}$ was then combined with the cumulative thickness distribution function (CDF) to determine a cutoff thickness $D_{TT}^{*}$ satisfying the relationship $CDF(D_{TT}^{*}) = f_{Lo}$, which was then used to classify the phase state of each segment (i.e., a segment whose thickness was greater than or equal to $D_{TT}^{*}$ was classified as Lo). The accuracy of this thickness-based classification scheme, shown in Fig. 3.11c and Table 3.3, is slightly greater than 80% for samples near the middle of the tieline where substantial fractions of both phases are present, and increases for samples closer to the tieline endpoints.

### 3.7.3 Phase classification by unsupervised ML

We next used unsupervised learning (*k*-means and *k*-medoids) to group the segment IPs into two clusters (we note that for this analysis, segments from all 11 samples were pooled prior to clustering).

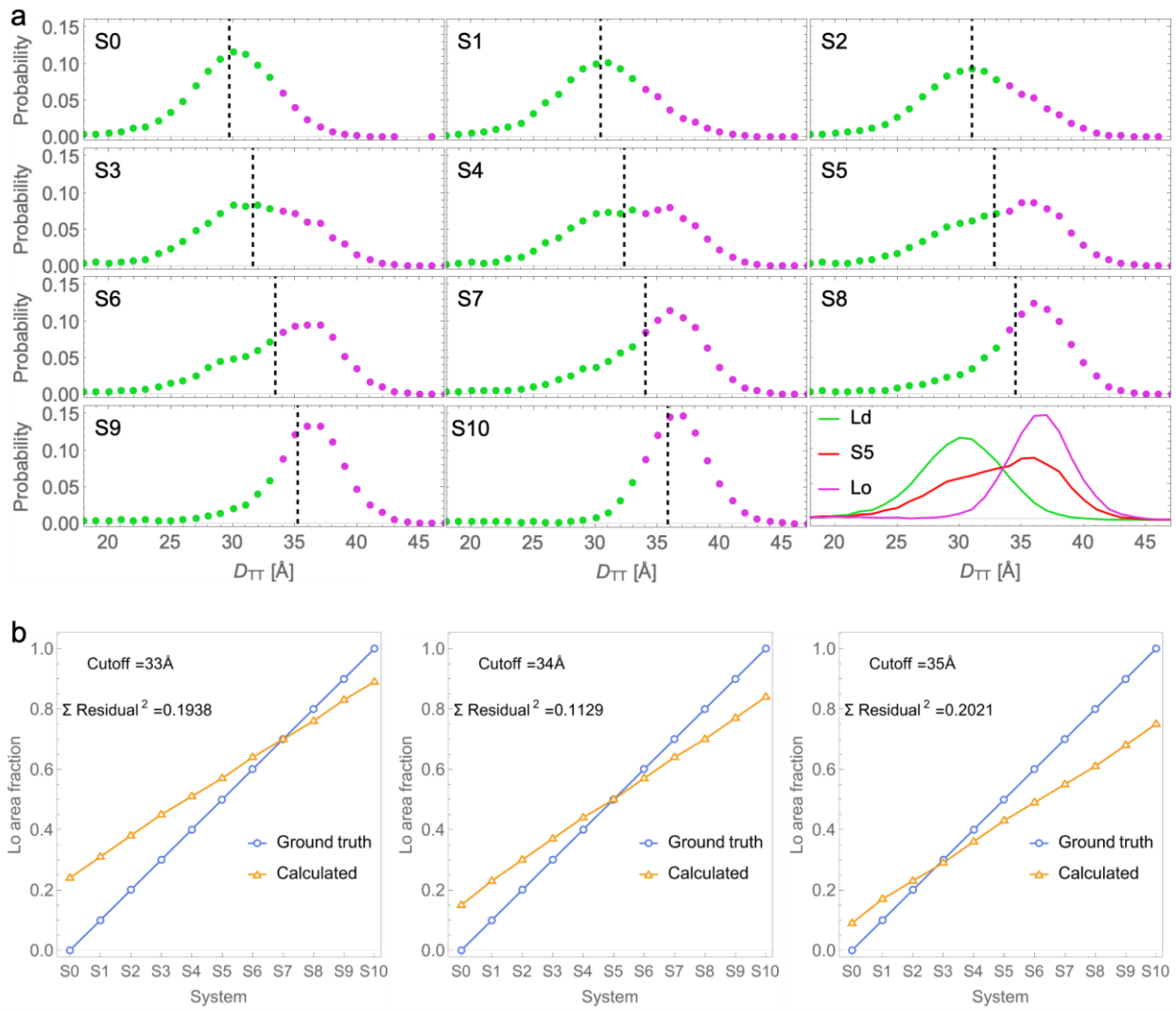


**Figure 3.10 Phase classification by segment thickness.** (a) Probability distribution of segment $D_{TT}$ values for datasets S0-S10. Segments with $D_{TT}$ values less than 34 Å are shown in green, while those exceeding this threshold are shown in pink. The mean segment $D_{TT}$ value is represented by a dashed line, providing a visual reference in various systems with systematic increase in $D_{TT}$ as we move from S0 to S10. (b) Predicted Lo area percentage using different thickness cutoffs for segment classification as indicated on the figure.

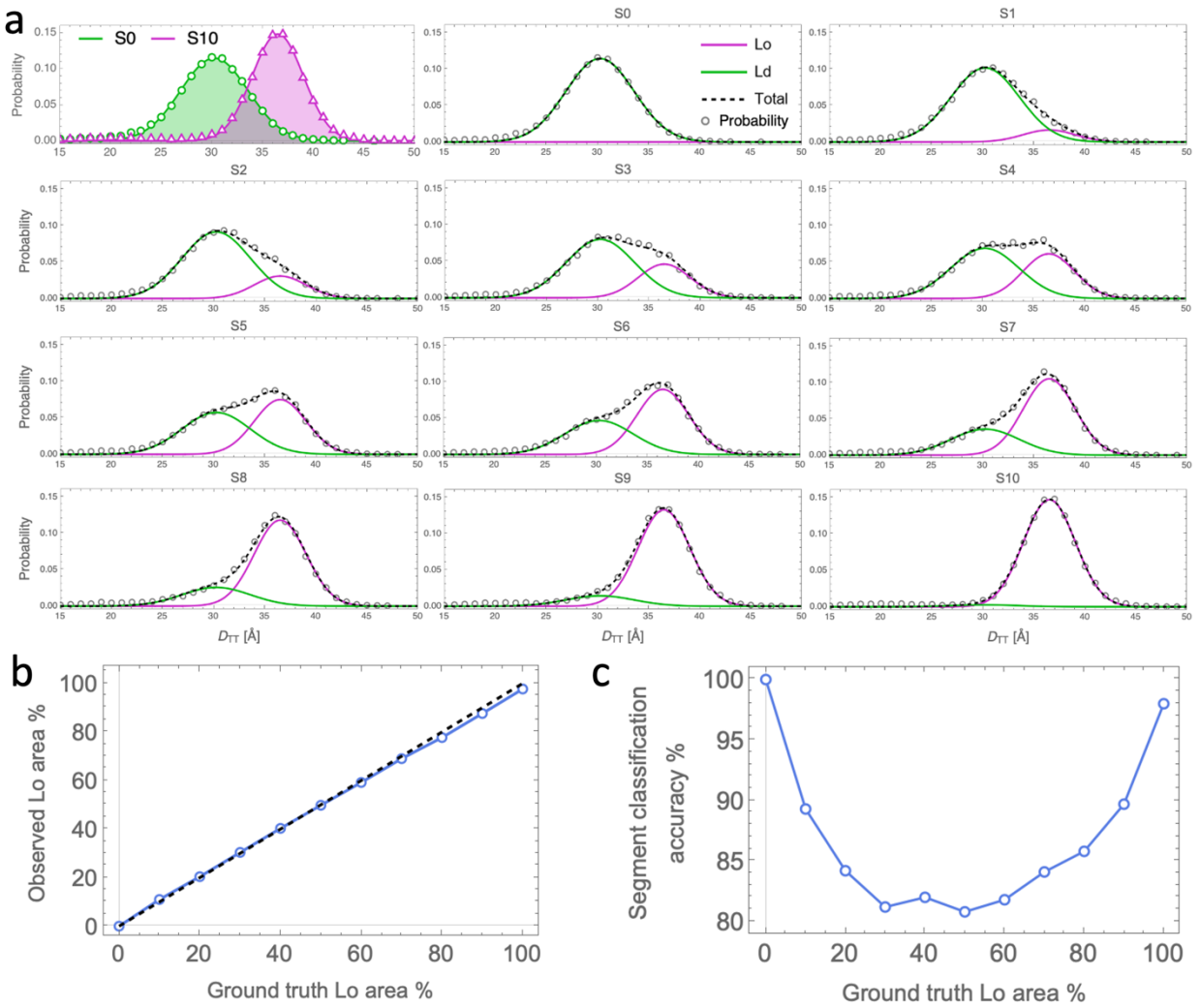


**Figure 3.11 Phase classification by segment thickness.** (a) Probability histograms of segment $D_{TT}$ values for tieline endpoint datasets S0-S10 (open symbols). The upper left plot shows data from the tieline endpoints S0 and S10 fitted to Gaussian distributions (solid lines). The remaining plots show the result of fitting the $D_{TT}$ distribution as a weighted sum of the Lo and Ld endpoint distributions (black dashed line). The weighted Ld and Lo components are shown as green and pink curves, respectively. (b) Comparison of the ground truth Lo area percentage (black dashed line) to the percentage calculated from the fitted weights (blue symbols) for datasets S0-S10. (c) Percentage of accurately classified segments vs. Lo area percentage.

As shown in Table 3.3, both clustering methods resulted in reasonable area percentage predictions for all compositions, deviating by < 5% from ground truth values. Both methods also achieved good accuracy (> 90%) at the level of individual segment classification (Table 3.4). The accuracy was correlated with the position of the sample on the tieline, with the lowest accuracy consistently occurring near the middle of the tieline (i.e., sample S5). To assess the impact of dimensionality reduction, we also performed clustering after first subjecting the IPs to a global principal component analysis. Figure 3.12 reveals that segment accuracy exceeds 90% for all datasets even when only the first two principal components are used for clustering. We note that for datasets of the size used here, *k*-means and *k*-medoids clustering are computationally inexpensive and fast on a desktop computer even when the full 201-dimensional IP is used.

### 3.7.4 Phase classification by supervised ML

We next tested five supervised ML algorithms as described in Methods. Models were trained on segment IPs from the Ld and Lo datasets, around 1000 vesicles of uniform size distribution. Table 3.3 compares the Lo area percentage predicted by these models to predictions from thickness-based and unsupervised methods, while Table 3.4 compares the overall accuracy of binary phase classification for the various datasets and methods at the level of individual segments. Like the unsupervised methods, accuracy is strongly correlated with the position of the sample on the tieline (Fig. 3.13a). Comparing different methods, Gradient Boosted Trees (GBT) and Logistic Regression (LR) emerged as the most accurate overall, followed closely by Nearest Neighbors (NN) and Random Forest (RF): Decision Tree (DT) was significantly less accurate. Figure 3.14 shows an example of the confusion matrices that were used to calculate binary accuracy. Because supervised methods yield probability-based predictions (i.e., the probability that a given segment is Lo phase), we can further assess the ability of these models to recognize domain boundaries that are inherently weighted superpositions of Lo and Ld IPs. For each segment, we first calculated the fraction of total intensity originating from the Lo phase, termed as the segment's ordered character ($OC$). The residual $OC - OC'$, where $OC$ is the ground truth value and $OC'$ is the probability determined by a supervised model.

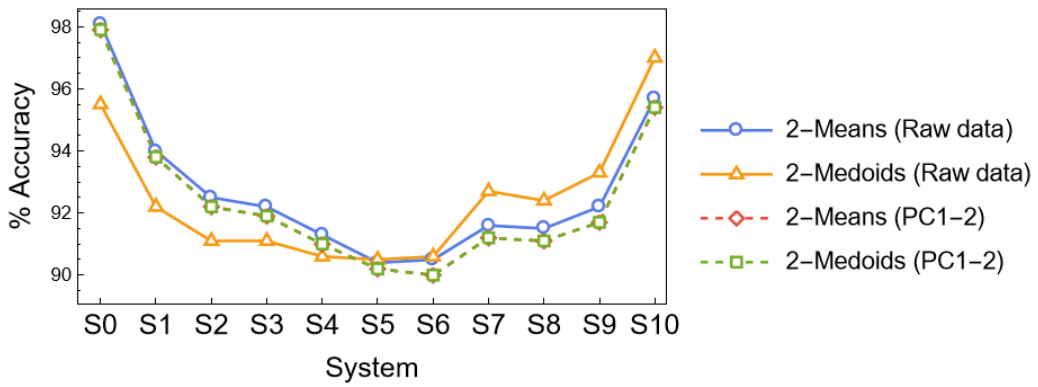


**Figure 3.12 Phase classification accuracy of unsupervised ML methods.** Shown is the segment-level accuracy for datasets S0-S10 from *k*-means (blue) or *k*-medoids (orange) clustering using the full IP (solid shading) or the first two principal components (hatched shading). When considering the first two principal components, the centroids for 2-means and medoids for 2-medoids were found to be in close proximity to each other.

**Table 3.3** Area percentage of Lo phase determined by different phase classification methods.

| | | *Thickness* | *Unsupervised ML* | | *Supervised ML with size training* | | | | |
|---|---|---|---|---|---|---|---|---|---|
| Sample | Ground truth | | 2-means cluster | 2-medoids cluster | DT | GBT | RF | LR | NN |
| S0 | 0.0 | 0 | 2 | 4 | 4 | 1 | 2 | 1 | 1 |
| S1 | 10.0 | 11 | 11 | 14 | 13 | 11 | 11 | 11 | 10 |
| S2 | 20.0 | 20 | 20 | 24 | 22 | 21 | 21 | 21 | 19 |
| S3 | 30.0 | 30 | 30 | 34 | 32 | 31 | 31 | 31 | 30 |
| S4 | 40.0 | 40 | 39 | 43 | 40 | 40 | 40 | 40 | 38 |
| S5 | 50.0 | 50 | 48 | 52 | 49 | 50 | 49 | 50 | 48 |
| S6 | 60.0 | 59 | 57 | 60 | 58 | 60 | 58 | 60 | 57 |
| S7 | 70.0 | 69 | 67 | 70 | 68 | 70 | 69 | 71 | 68 |
| S8 | 80.0 | 78 | 76 | 79 | 76 | 79 | 78 | 80 | 77 |
| S9 | 90.0 | 88 | 86 | 88 | 85 | 89 | 87 | 90 | 87 |
| S10 | 100.0 | 98 | 96 | 97 | 94 | 99 | 97 | 99 | 97 |

**Table 3.4** Segment-level accuracy determined by different phase classification methods.

| Sam. | $D_{TT}$ | *Unsup. ML* | | *Supervised ML* | | | | | | | | | |
|---|---|---|---|---|---|---|---|---|---|---|---|---|---|
| | | 2-mean | 2-med. | DT | | GBT | | RF | | LR | | NN | |
| | | | | ST[a] | PP[b] | ST[a] | PP[b] | ST[a] | PP[b] | ST[a] | PP[b] | ST[a] | PP[b] |
| S0 | 100 | 98 | 96 | 96 | 96 | 99 | 99 | 98 | 99 | 99 | 99 | 99 | 99 |
| S1 | 89 | 94 | 92 | 92 | 93 | 96 | 96 | 95 | 95 | 96 | 96 | 95 | 95 |
| S2 | 84 | 92 | 91 | 91 | 92 | 95 | 95 | 94 | 94 | 95 | 95 | 94 | 94 |
| S3 | 81 | 92 | 91 | 90 | 91 | 94 | 95 | 93 | 94 | 95 | 95 | 94 | 94 |
| S4 | 82 | 91 | 91 | 90 | 91 | 94 | 94 | 93 | 94 | 94 | 94 | 93 | 94 |
| S5 | 81 | 90 | 90 | 89 | 90 | 93 | 93 | 92 | 93 | 93 | 93 | 92 | 93 |
| S6 | 82 | 90 | 91 | 90 | 90 | 94 | 94 | 92 | 94 | 94 | 94 | 92 | 94 |
| S7 | 84 | 92 | 93 | 91 | 92 | 95 | 95 | 93 | 94 | 95 | 95 | 93 | 95 |
| S8 | 86 | 92 | 92 | 91 | 92 | 95 | 95 | 93 | 94 | 95 | 95 | 93 | 95 |
| S9 | 90 | 92 | 93 | 91 | 93 | 96 | 96 | 94 | 95 | 96 | 96 | 94 | 96 |
| S10 | 98 | 96 | 97 | 94 | 97 | 99 | 99 | 97 | 99 | 99 | 99 | 97 | 99 |

[a]Size training; [b]IP pre-processing

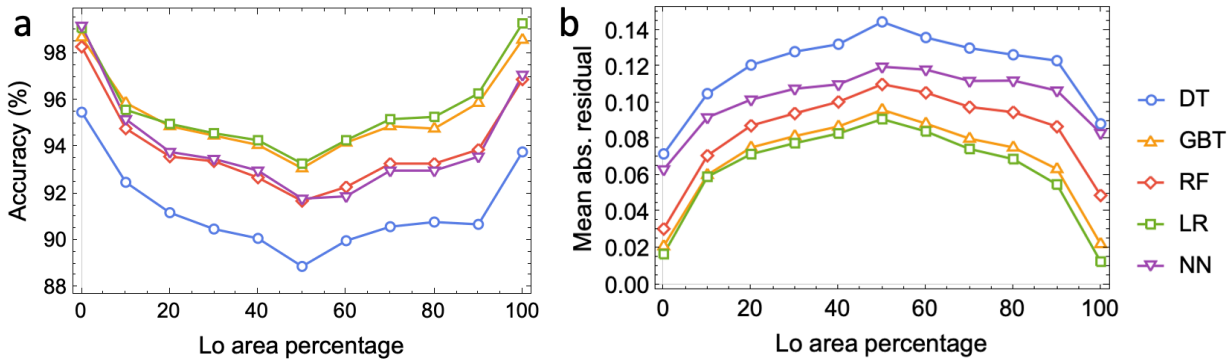


**Figure 3.13 Accuracy of phase classification by supervised ML methods.** (a) Percentage of correctly predicted segments vs. Lo area percentage. (b) Mean absolute residual of segment ordered character as defined in the text. Methods used: Decision Tree (DT), Gradient Boosted Trees (GBT), Random Forest (RF), Logistic Regression (LR), and Nearest Neighbors (NN).


**Figure 3.14 Confusion matrices.** Shown are the confusion matrices for each dataset from the GBT model. Diagonal elements (top-left and bottom-right) represent correct classifications whereas off-diagonal elements (top-right and bottom-left) represent misidentification.

It is a natural alternative metric for quantifying accuracy, with smaller values indicating greater accuracy. The mean absolute residual (i.e., averaged over all segments in a dataset) is plotted vs. Lo area percentage in Fig. 3.13b for the different supervised methods, revealing similar overall trends compared to the binary phase classification.

### 3.7.5 Visualizing phase classification accuracy

It is instructive to visualize the accuracy of phase classification at the vesicle level. Figure 3.15 presents ring plots of representative vesicles in which ground truth $OC$ values of individual segments are found in the innermost ring and $OC'$ values predicted by the various supervised models are arranged concentrically. The green-pink color scale facilitates the identification of misclassified segments (i.e., an Lo segment identified as Ld or vice versa), in this case when a binary cutoff of $OC^* = 0.5$ was used, as described in Methods. A few such misclassified segments are found in each of the phase separated vesicles shown in Fig. 3.15. The probability of misclassification is greater near domain boundaries where both phases contribute to the projected signal. The representative examples of pure Ld and Lo vesicles shown in Fig. 3.15b and 3.15g contain no misclassifications, consistent with the absence of confounding boundary segments in these datasets, although misclassifications in the bulk do occasionally occur in both uniform and phase-separated vesicles and can be seen in Fig. 3.15c, 3.15e and 3.15f. The trends in accuracy shown in Fig. 3.13 can be explained by the difficulty of classifying boundary segments. The lowest overall accuracy occurs in system S5, which has equal area fractions of the two phases and thus the largest number of boundary segments. Indeed, every projection image for this sample—regardless of the vesicle's 3D orientation—is assured to have boundary segments, as demonstrated in Fig. 16a-f. However, as the vesicle composition moves toward the ends of the tieline in either direction, the size of one domain increases at the expense of the other, and the total domain boundary length in the projected images decreases. Consequently, there is a non-zero probability of observing only the majority phase at the edges of a projected vesicle, as demonstrated in Fig. 3.16l for sample S2. Such projections are relatively common for compositions near the ends of the tieline (Fig. 3.17), and as a result, the accuracy of phase identification is higher than for samples near the middle of the tieline.

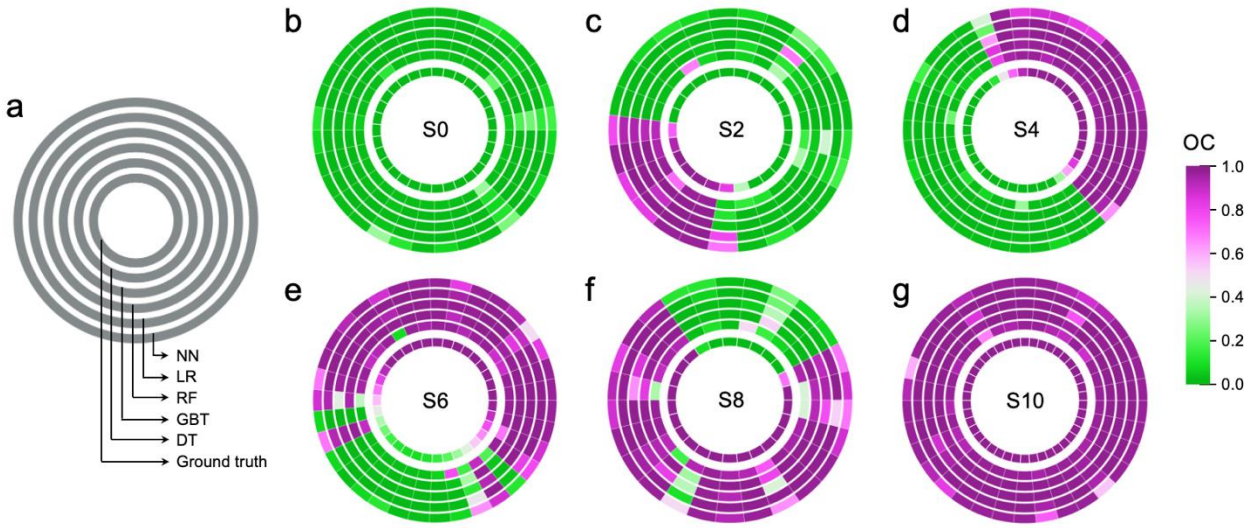


**Figure 3.15 Visualizing the accuracy of phase classification for individual vesicles.** (a) Legend: the inner ring gives the ground truth $OC$ for individual 5 nm segments of a vesicle, with model predictions $OC'$ arranged concentrically as indicated. (b-g) Ring plots of representative vesicles for different datasets as indicated. Methods used: Decision Tree (DT), Gradient Boosted Trees (GBT), Random Forest (RF), Logistic Regression (LR), and Nearest Neighbors (NN).

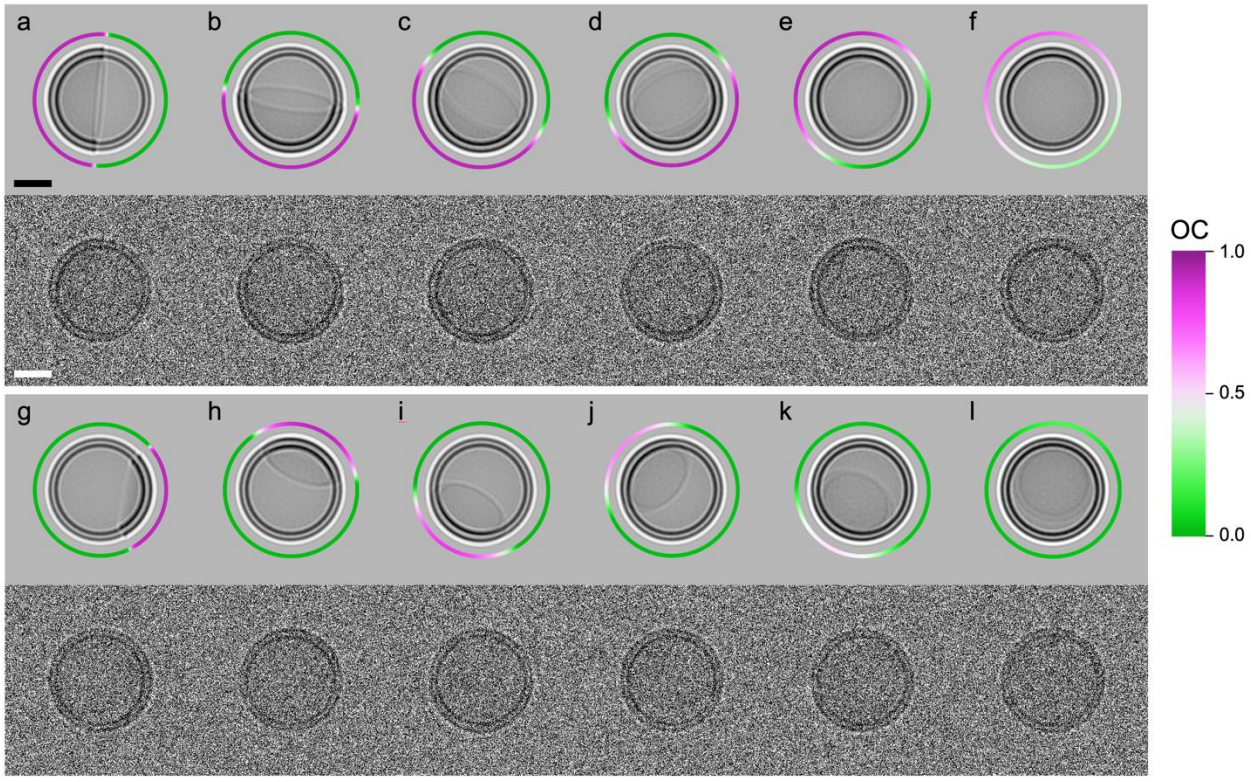


**Figure 3.16 Selected images demonstrating the influence of vesicle orientation on apparent phase behavior.** Show are pairs of images for several orientations of ~ 50 nm diameter vesicles from datasets S5 (a-f) and S2 (g-l). In each pair, the upper and lower images are before and after the addition of Gaussian noise, respectively. The ring surrounding the vesicle in the noise-free images plots the ground truth $OC$ value along the projected circumference as indicated by the color scale. Scale bar 20 nm.

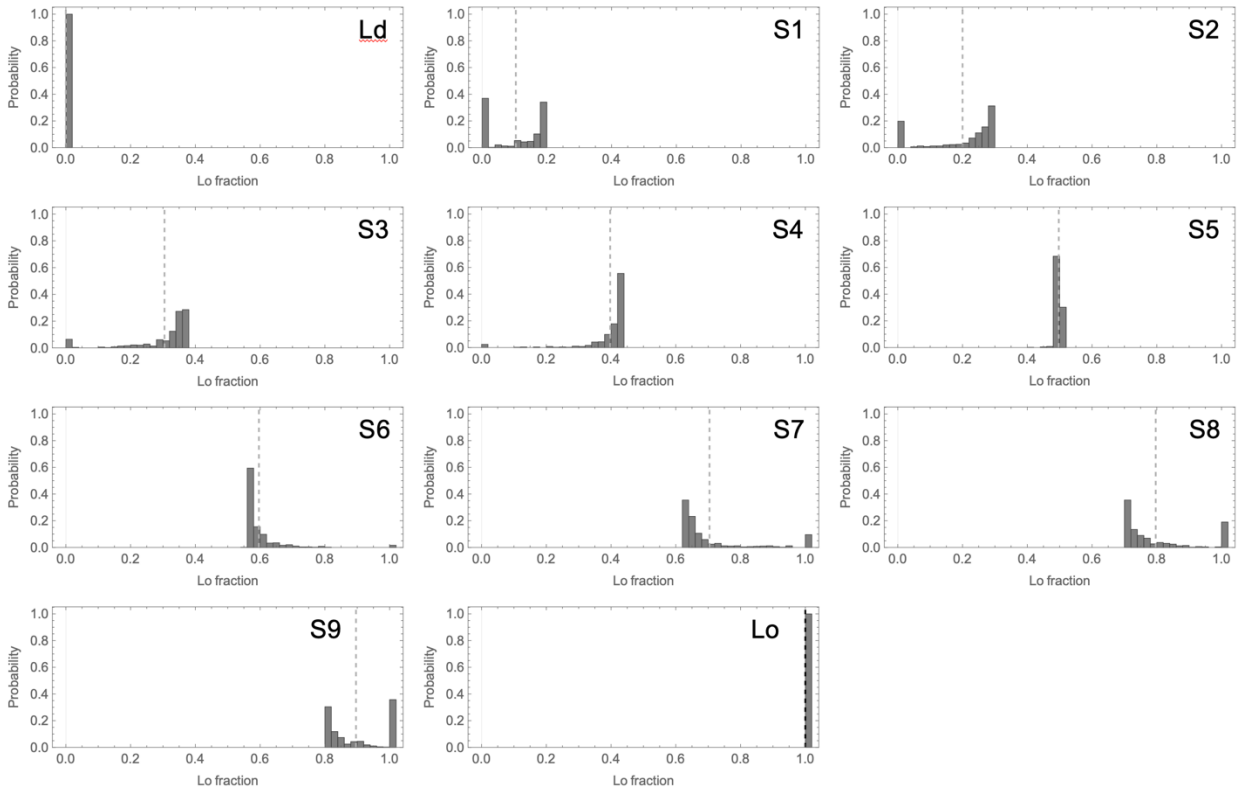


**Figure 3.17 Variability of apparent phase fraction for randomly oriented vesicles.** Shown are histograms of the ground truth Lo phase fraction for the 490 vesicles in each dataset as indicated in the figure. The mean Lo fraction is shown as a dashed line.

Further insight can be gained by visualizing segment classification accuracy for an entire dataset. For this purpose, we generated matrix plots in which rows correspond to individual vesicles (arranged from smallest to largest diameter, top to bottom) and columns correspond to individual segments (arranged such that the middle of the minority-phase domain is centered within the row), as shown in Fig. 3.18 for system S4. Several interesting aspects of the datasets become apparent in these plots. For example, the ground truth $OC$ values plotted in Fig. 3.18b explicitly show how the fraction of boundary segments (i.e. those with lighter shades) varies widely between vesicles due to differences in their random 3D orientations prior to projection (cf. Fig. 3.16). In a few cases, the vesicle was oriented such that the domain boundary was nearly parallel to the projection plane, resulting in every segment containing intensity contributions from both phases. Figure 3.18a plots the corresponding $OC'$ values predicted by GBT, revealing a strong tendency for the model to predict values close to 0 or 1 and eschew intermediate values, even for boundary segments whose ground truth $OC$ values are in fact intermediate. This tendency is emphasized in Fig. 3.18c, which plots the signed residual $OC - OC'$ and thus makes clear the outsized contribution of boundary segments to overall accuracy. The relatively poor performance in boundary identification is likely caused by the fact that the models were not trained to recognize boundary segments. Adding such segments to the training dataset will almost certainly improve the predictions and may prove to be important for real-world data analysis, where the likelihood of encountering multiple smaller domains within vesicles is greater.

### 3.7.6 Average IPs of coexisting phases

Among the most important information obtained from cryo-EM analysis is the average IP of the bilayer. In principle, the bilayer's electron scattering profile can be recovered from the IP by deconvolution[86], raising the possibility of using cryo-EM to complement well-established neutron and X-ray based methods for bilayer structure determination.[78] A significant advantage of cryo-EM compared to traditional scattering methods is the ability to classify individual segments by their phase and thus separately determine the IPs of coexisting phases.

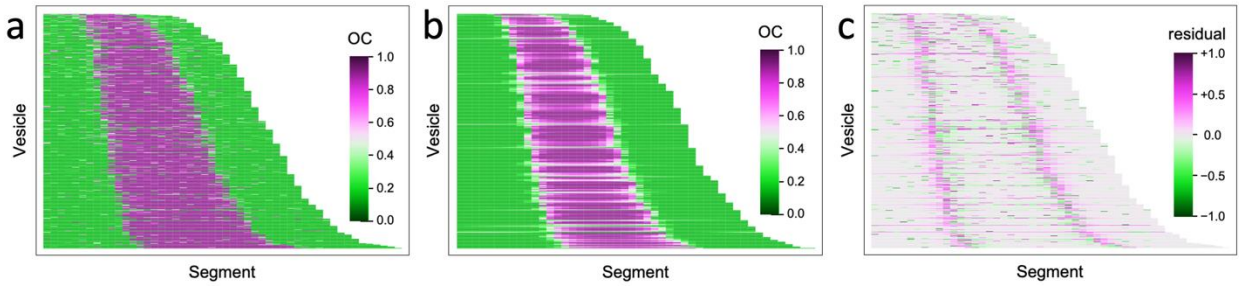


**Figure 3.18 Matrix plots of ordered character.** Each row represents one of 490 vesicles in dataset S4, where the columns are individual 5 nm segments of the vesicle. Plotted are: (a) the $OC'$ prediction from the GBT model; (b) the ground truth $OC$ value; (c) the signed residual $OC - OC'$.

Figure 3.19a compares the mean IPs for Ld and Lo phases (i.e., averaged over all segments classified as Ld or Lo) for samples S0-S10 using predictions from GBT. As expected, agreement with ground truth profiles (Fig. 3.9) is better for the majority phase in each dataset, although the overall agreement for both phases is reasonable in all datasets. Figure 3.19b shows that $D_{TT}$ values calculated from the IPs of phase separated samples S1-S9 are generally in excellent agreement with the values calculated from the pure Ld and Lo datasets (dashed lines) although deviations occur for the minority phase near tieline endpoints.

### 3.7.7 Isolating vesicle size effects

It is well established that nanoscopic membrane curvature plays a vital role in many biological processes.[131, 132] Curvature is influenced by intrinsic factors such as lipid composition and the presence of integral membrane proteins, as well as by external factors including cytoskeletal attachments and the binding of peripheral membrane proteins.[133] Even in simple liposomes with nominally identical leaflet compositions, it is likely that substantial structural perturbations emerge in the presence of high membrane curvature. This has been observed in coarse-grained molecular dynamics simulations of 20 nm diameter vesicles, which showed changes in the headgroup and acyl chain packing of inner and outer leaflets that depended both on lipid headgroup type and tail saturation.[134] In this context, another major advantage of cryo-EM compared to neutron and X-ray scattering is the ability to isolate membranes of different average curvature within the sample and separately interrogate their structure.

As a proof-of-principle demonstration, we binned vesicles in each dataset by size and calculated several properties for the different bins (we note that all vesicles in our simulated datasets have identical bilayer structure irrespective of their size). Figure 3.20 shows the apparent phase area fractions for systems S1-S9 calculated separately for each vesicle size bin. We also attempted to determine the average linear extent and number of domains as a function of vesicle size. This was complicated by the non-negligible frequency of segment misclassifications far from domain boundaries (cf. Fig. 3.15), which have the effect of erroneously dividing a continuous domain into two or more discontinuous domains.

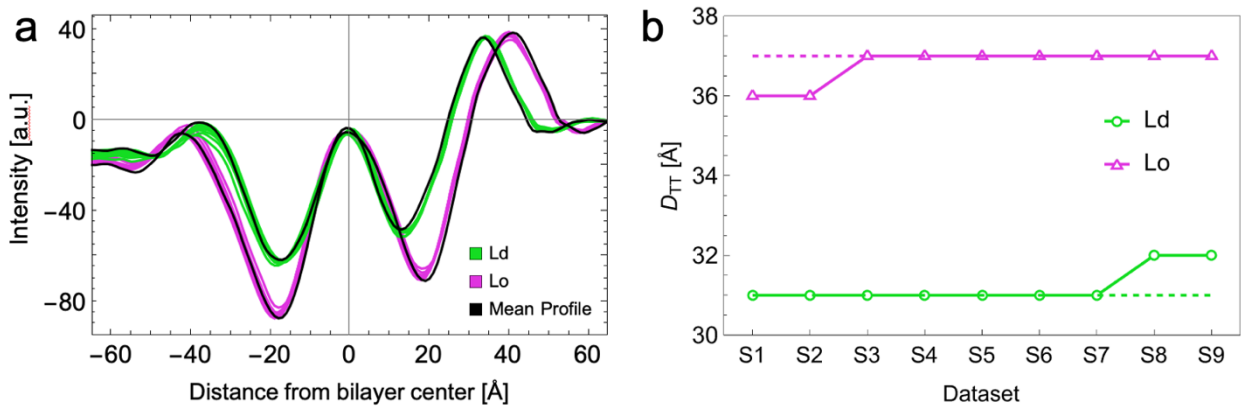


**Figure 3.19 Average intensity profiles and $D_{TT}$ values.** (a) After classification by GBT, the mean intensity profile for all Lo (Ld) segments is depicted in pink (green) for each phase separated dataset (i.e., S1-S9), while the mean intensity profiles of pure Ld and Lo (datasets S0 and S10, respectively) are shown in black. (b) $D_{TT}$ values evaluated from the mean intensity profiles shown in (a). Dashed pink and green lines represent the $D_{TT}$ value of the pure Ld and Lo datasets.

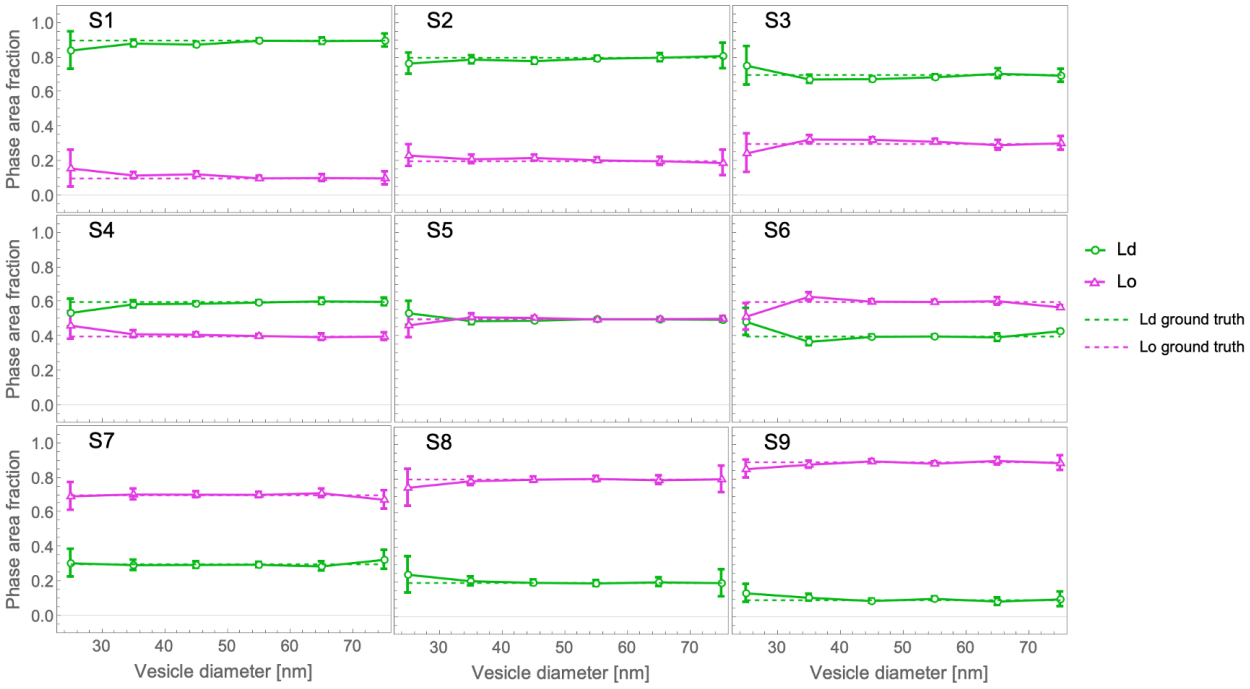


**Figure 3.20 Influence of vesicle size on apparent phase area fractions.** The area fraction of Ld (green) and Lo (pink) phases predicted by LR is shown as a function of vesicle size for each of the phase separated datasets. Error bars are 95% confidence intervals.

To counteract this artifact, we implemented a correction that eliminated isolated segments (i.e., those whose phase classification was different than its two nearest neighbors) as illustrated in Fig. 3.21. With this correction, the average domain size calculated from images was similar to ground truth values (Fig. 3.22). Reasonably good agreement between the average number of domains per vesicle calculated from images and the ground truth value (i.e., 2 domains per vesicle) was also obtained from this analysis (Fig. 3.21b-c).

### 3.7.8 Simulating noise in synthetic images

It is often noted that the signal-to-noise ratio (SNR) of cryo-EM is among the lowest of any imaging technique, with the noise power typically exceeding the signal power by more than an order of magnitude.[105] When ground-truth datasets are used to assess the performance of classification methods, it is therefore reasonable to question whether the simulated noise characteristics accurately reflect real-world noise, and how any simplifying assumptions might influence the outcome. Baxter et al. have identified three independent sources of noise in cryo-EM projection images: (1) “structural noise” originating from variability in the local background structure (e.g., ice thickness) of individual vitrified particles as well as particle-to-particle conformational variability; (2) shot noise originating from the quantum nature of electron radiation; and (3) digitization noise arising from processes associated with image capture (e.g., CCD readout noise).[135] Through a careful analysis of paired projection images of ribosomes, the same authors were able to disentangle these noise sources and separately determine their magnitude, finding that shot noise is ~ 10-fold larger than structural noise, which in turn is over 10-fold larger than digitization noise.[135] Clearly, shot noise is the dominant contributor to the low SNR of cryo-EM images.

In addition to having different magnitudes, the factors responsible for the independent noise sources act at different stages of the image generation process. Because the factors that give rise to structural noise are present in the vitrified sample itself, structural noise is affected by the CTF and is thus frequency dependent. In contrast, shot noise and digitization noise originate at the detector and can be considered as white (i.e., frequency-independent) noise sources.

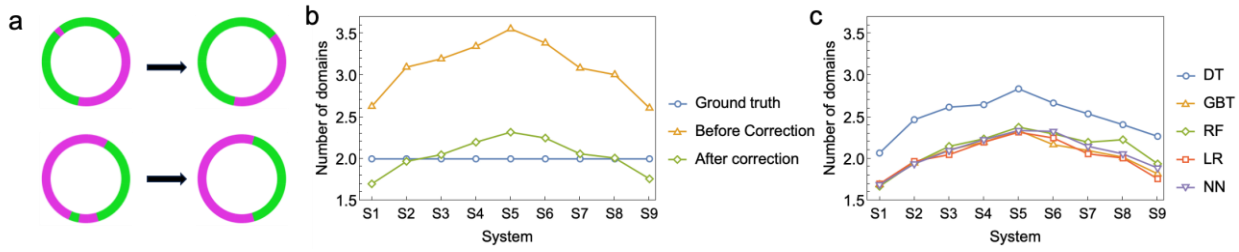


**Figure 3.21 Predicting the number of domains per vesicle.** (a) Schematic illustration of the correction used to eliminate isolated segments that are likely to be misclassified. (b) Number of domains calculated using LR before and after the correction, shown for each dataset. (c) Number of domains calculated using each supervised method, shown for each dataset.

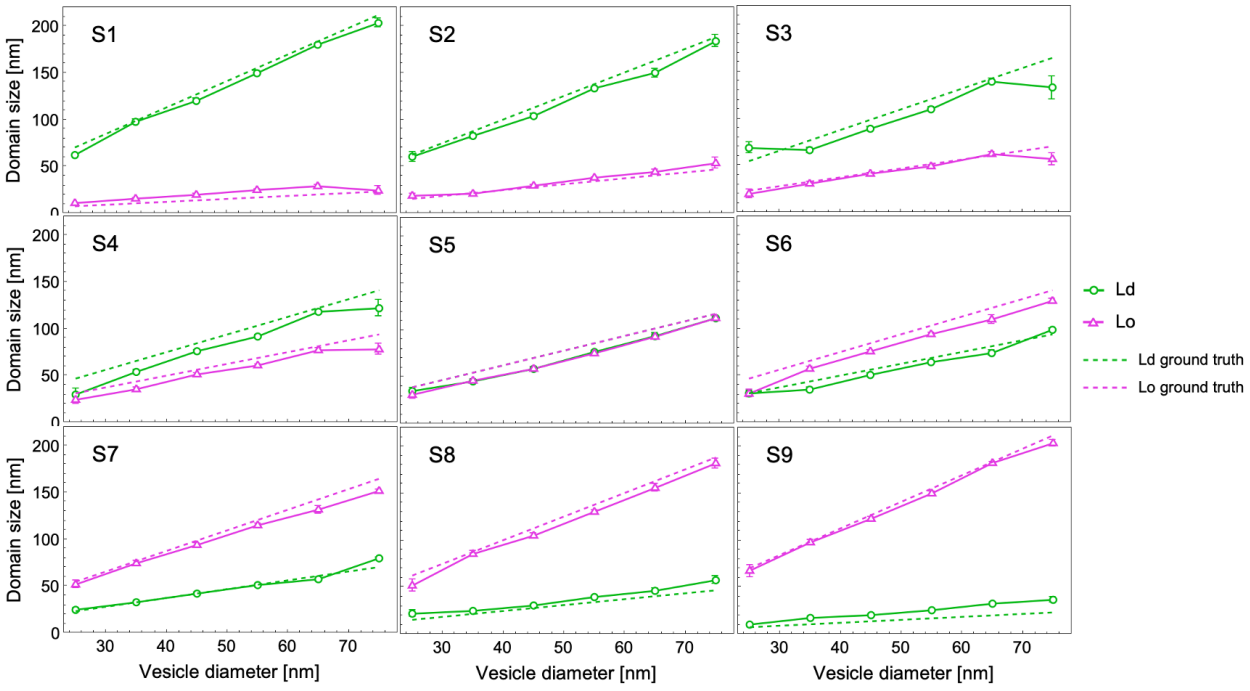


**Figure 3.22 Influence of vesicle size on apparent domain size.** The computed domain size across all nine systems is presented to examine the impact of vesicle sizes on area fractions. Logistic Regression (LR) is employed as the classification technique.

When generating synthetic images, it follows that structural noise (typically modeled as a zero-mean Gaussian noise image) must be added to the projection image prior to convolution with the CTF, while the effects of shot noise and digitization noise can be combined in a single zero-mean Gaussian noise image that is added to the CTF-corrupted particle image.[135] We note that, although shot noise is inherently governed by Poisson statistics, the use of a Gaussian distribution is justified by the relatively high electron counts per pixel[136].

The use of zero-mean Gaussian noise in simulated liposome datasets is further validated in Fig. 3.23, which shows that histograms of pixel intensities in particle-free regions of a representative experimental image are well-described by Gaussian distributions.

The full procedure for generating synthetic images of liposomes in the presence of both frequency-dependent and frequency-independent noise sources is outlined schematically in Fig. 3.4. As described in Methods, we omitted the frequency-dependent structural noise in our simulated datasets and included only frequency-independent zero-mean Gaussian noise with a standard deviation that was adjusted to mimic experimentally observed contrast-to-noise ratios of vitrified liposomes. It has previously been suggested that for synthetic cryo-EM images of ribosomes to be 'realistic', a frequency-dependent noise component with SNR ~ 1 should be included.[135] Although the magnitude of the structural noise for liposomes has not been reported to our knowledge, we tested whether including a structural noise component with a magnitude similar to that of vitrified ribosomes would affect the classification of segment phase state. Table 3.5 shows that including structural noise in both the training and testing datasets resulted in negligible differences in prediction accuracy compared to the case where training and testing data both lacked structural noise. We are therefore confident that our reported prediction accuracies reflect outcomes that would be obtained in real-world analyses of similar samples, provided that the training and testing data are subject to the same sources of noise with comparable SNR.

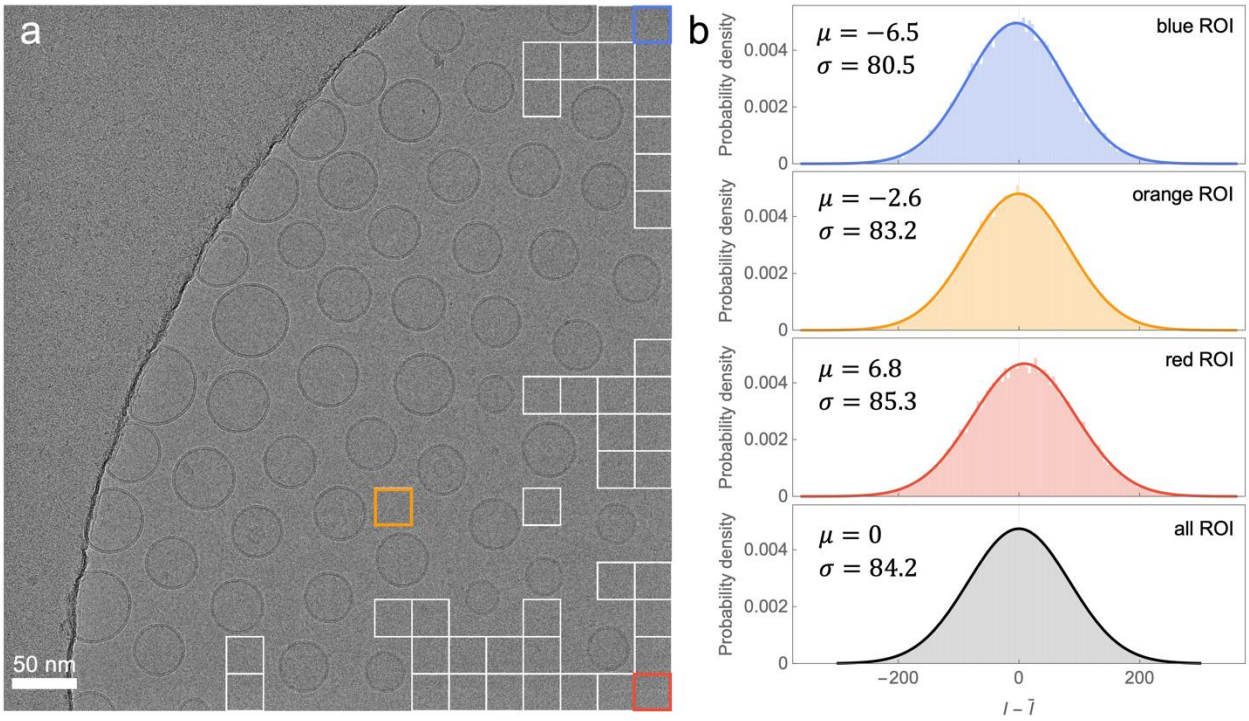


**Figure 3.23 Examining background noise in experimental cryo-EM images.** (a) A representative image of a field of vesicles composed of DOPC and POPG (95/5 mol%). The image was acquired on an FEI Polara G2 operating at an accelerating voltage of 300 kV and equipped with a Gatan K2 Summit detector operated in counting mode. The defocus length calculated for this image was 2.00 μm and the pixel size was 2.73 Å. Boxes are 200x200 pixel regions selected for background noise analysis using the criteria that the region contains only vitrified water (i.e., it is inside the well and free of vesicles and debris). (b) From top to bottom, histograms of pixel intensity values for three ROIs highlighted in blue, orange, and red in panel a, and the total histogram from all boxed regions in panel a (black). The mean ($\mu$) and standard deviation ($\sigma$) of the pixel values are shown for each ROI, and the solid line is a plot of the Gaussian probability density function for the corresponding values of $\mu$ and $\sigma$.

**Table 3.5** Area percentage of Lo phase and segment-level accuracy determined by different phase classification methods for the S5 dataset with and without structural noise.

| Sample | Ground truth | DT | GBT | RF | LR | NN |
|---|---|---|---|---|---|---|
| | | | *Area percentage of Lo phase* | | | |
| S5 | 50.0 | 50 | 50 | 49 | 50 | 49 |
| S5-struct[1] | 50.0 | 50 | 50 | 49 | 50 | 49 |
| | | | *Segment-level accuracy* | | | |
| S5 | 50.0 | 88 | 93 | 92 | 93 | 92 |
| S5-struct[1] | 50.0 | 87 | 93 | 91 | 93 | 92 |

[1]Images included a structural noise component as described in Section 3.8 of the main text.

### 3.8 Sampling the vesicle orientational distribution

Because projection images capture only a relatively small portion of the total vesicle surface, phase fractions calculated from individual vesicles can vary substantially depending on the orientation of the vesicle (Fig.3.17). This can result in large uncertainties in the mean area fraction calculated from a sparse dataset where the orientational distribution may be under sampled. To estimate the uncertainty in reported phase fractions, we simulated experiments in which the mean phase fraction was calculated from a dataset of $N$ vesicles with random orientations; repeating the experiment a large number of times provides an adequate sampling from which to calculate the standard deviation of the mean and thus estimate the uncertainty inherent to a single dataset. Figure 3.24 demonstrates this procedure for vesicles with a ground truth Lo fraction of 0.3 and varying $N$ from 1 to 1000, in each case simulating the experiment 1000 times. Consistent with Fig. 3.17, the Lo fraction measured from individual vesicles is broadly distributed between 0 and 0.37. As the number of vesicles in the dataset increases, the distribution of the mean phase fraction narrows considerably; for $N = 500$ (Fig. 3.24), the standard deviation is ~ 0.005. Figure 3.25 plots the standard deviation as a function of $N$ for datasets S1-S5 (corresponding to domain area fractions 0.1-0.5). For datasets with 490 vesicles, the standard deviation is less than 0.005.

### 3.9 Summary and Conclusions

We report on a new application of machine learning to classify the phase state of lipid bilayers in cryo-EM images. To mimic the scenario of lipid rafts in eukaryotic plasma membranes, we analyzed synthetic images of phase separated vesicles constructed from MD simulations of Ld and Lo phases. The use of ground truth datasets allowed us to compare the accuracy of different methods, in addition to testing the performance of the models in the presence of heterogeneities in both vesicle size and domain size. Our most important finding is that ML methods can classify the phase state of the bilayer at accuracies exceeding 90% for the conditions that were simulated. Supervised methods such as Logistic Regression and Gradient Boosted Trees showed the highest accuracy, while unsupervised methods such as *k*-means and *k*-medoids closely followed.

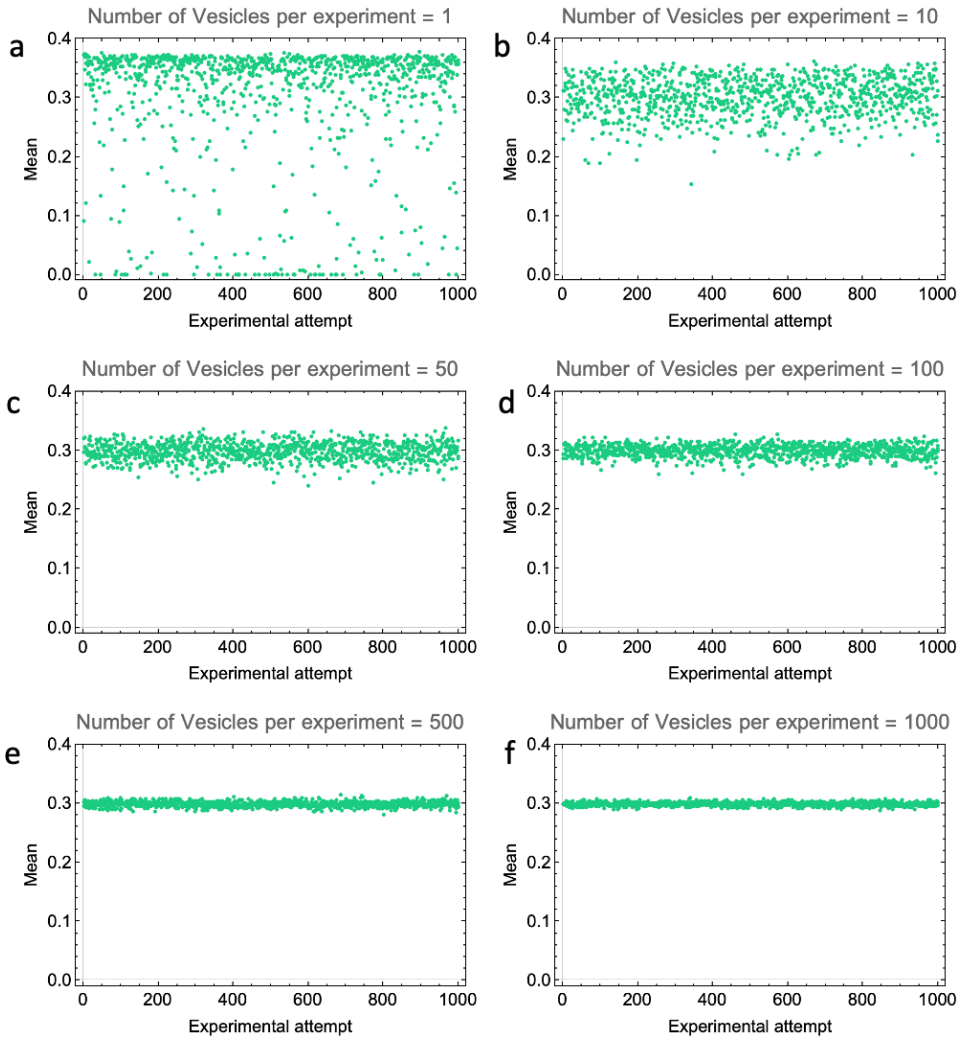


**Figure 3.24 Uncertainty in the mean Lo area fraction from simulated datasets.** Simulated vesicles with Lo fraction equal to 0.3 were given random 3D orientations, and the apparent Lo phase fraction was then calculated from corresponding projection images. Shown in panels a-f is the mean Lo fraction calculated from the stated number of vesicles for $10^3$ replicate simulation experiments.

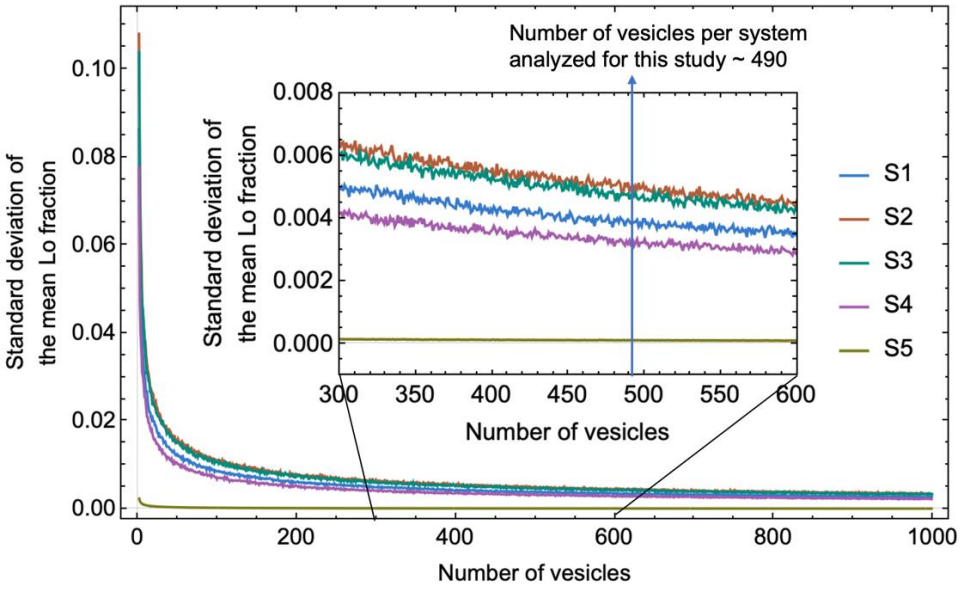


**Figure 3.25 Uncertainty in the mean Lo phase fraction depends on composition and number of observed vesicles.** Shown is the standard deviation of the apparent Lo area fraction calculated from $10^3$ replicate simulation experiments, for true Lo phase fractions 0.1 (blue), 0.2 (red), 0.3 (green), 0.4 (purple), and 0.5 (olive), i.e., with compositions corresponding to datasets S1-S5. The inset expands the plot to reveal detail.

Notably, unsupervised methods exhibited greater accuracy than some supervised methods, showcasing their potential for analyzing standalone experimental datasets and characterizing nanodomains in the absence of training data. In comparing results from supervised and unsupervised ML methods, we do not wish to imply that one is intrinsically superior to another; indeed, compared to classification based on segment thickness alone, each of the ML methods showed significantly improved performance. Instead, the choice between methods depends on the scientific questions being asked and the data that are available.

We observed that prediction accuracy decreased for samples positioned in the middle of a tieline where approximately equal fractions of each phase are present, owing to the presence of domain boundaries that are particularly prone to misidentification in a binary classification scheme. Extensive domain interface is a hallmark of nanoscopic phase separation, and the ability to correctly classify boundary segments is thus a key target for future development. It must also be recognized that additional challenges are encountered *in vitro* and *in vivo* that are not accounted for in our *in silico* datasets; these include variability in physical parameters such as vesicle composition and ice thickness, as well as instrumental parameters like defocus length (26). Despite these limitations, the ability to directly image and decode nanoscopic membrane features will likely position cryo-EM at the leading edge of membrane biophysics in the years to come.

# Chapter 4

# Cryo-EM of laterally heterogeneous lipid vesicles: Supervised machine learning analysis of samples on a thermodynamic tieline.

A version of this chapter is in preparation to be submitted.

This chapter describes research designed by Karan D. Sharma, Deeksha Mehta, M. Neal Waxham, and Frederick A. Heberle. Experiments and data collection were performed by Karan D. Sharma, Deeksha Mehta, and M. Neal Waxham. Data analysis and writing of the manuscript was performed by Karan D. Sharma, Deeksha Mehta, M. Neal Waxham, and Frederick A. Heberle.

### 4.1 Abstract

Lipid rafts are thought to be crucial for cellular functions including signaling, but questions about their structure persist due to their small, nanoscopic size. Simplified model membranes containing low- and high-melting lipids along with cholesterol can be used to study the properties of raft-like domains. These mixtures typically show the coexistence of liquid-disordered (Ld) and liquid-ordered (Lo) phases over a range of compositions and temperatures. Spectroscopic and scattering methods can provide ensemble averaged domain sizes but lack the ability to resolve features of individual vesicles. Recently, cryogenic electron microscopy (cryo-EM) has been used to directly image nanoscale phase separation in lipid vesicles, using differences in the bilayer thickness of Ld and Lo phases as the primary source of contrast. In Chapter 3 of this dissertation, we developed an alternative image analysis pipeline based on supervised machine learning (ML) that takes advantage of both thickness and intensity differences between Ld and Lo. Using artificial images of vesicles as ground truth datasets, we showed that ML models trained on synthetic images of Ld and Lo phase vesicles achieved nearly 95% accuracy in predicting the phase state of vesicles where Ld and Lo domains coexisted. Here, we extend this proof-of-concept to experimental data: a set of vesicle samples known to lie on the same thermodynamic tieline at room temperature. The rules of thermodynamics dictate that the same Lo and Ld phases are present in each of these samples (i.e., the compositions of the phases are invariant). This constraint allowed us to use supervised learning, i.e., to train models on the two tieline endpoint samples, and then use those models to predict the phase state of vesicles in the remaining samples. For each analyzed vesicle, we were able to determine the number of domains, the domain size, and the phase area fractions. Our results reveal a surprisingly large vesicle-to-vesicle

heterogeneity and thus highlight the inadequacy of ensemble averages in capturing the complete landscape of nanoscale phase separation.

### 4.2. Introduction

Images of nanoscopic phase domains in lipid bilayers cannot be obtained using conventional optical microscopy. Indeed, much of our existing knowledge of these elusive structures comes from indirect biochemical measurements and spectroscopic data that often require complicated modeling. The lack of visual evidence has provided fuel for controversy about the physical origins (and even the very existence) of nanoscopic phase separation. A recent milestone in this debate was the use of cryo-electron microscopy (cryo-EM) [67] and cryo-electron tomography [93] to image nanoscopic liquid-liquid phase separation in liposomes and giant plasma membrane vesicles. Using cryo-EM, lipid membranes can be visualized at a resolution high enough to discern density variations in the individual leaflets of the bilayer, which enables local measurements of the bilayer thickness [26]. Within individual vesicles, these spatially resolved bilayer thickness measurements can then be used to infer the local phase state [67], since ordered phases are typically 5-10 Å thicker than disordered phases [57, 92, 116]. One limitation of this approach is the substantial noise in cryo-EM images, which results in broad and overlapping thickness distributions for liquid-disordered (Ld) and liquid-ordered (Lo) phases (Fig. 4.1). This makes it challenging to definitively classify the bilayer phase state based solely on thickness measurements. Thus, while previous studies have provided critical proof-of-principle for utilizing cryo-EM to probe lipid phase separation, the information contained in the images has yet to be completely mined [67].

Besides bilayer thickness, another characteristic that distinguishes ordered and disordered phases is the difference in molecular packing density. In cryo-EM images, these density differences create an intensity contrast (Fig. 4.2). In chapter 3, we showed that both the thickness and intensity differences of Ld and Lo phases are embedded in their intensity profiles (IPs) [94, 137].

Using simulated images as ground truth datasets, we developed a supervised machine learning (ML) pipeline in which models trained on Ld and Lo IPs were used to classify the local bilayer phase state in vesicles with coexisting Ld and Lo domains.

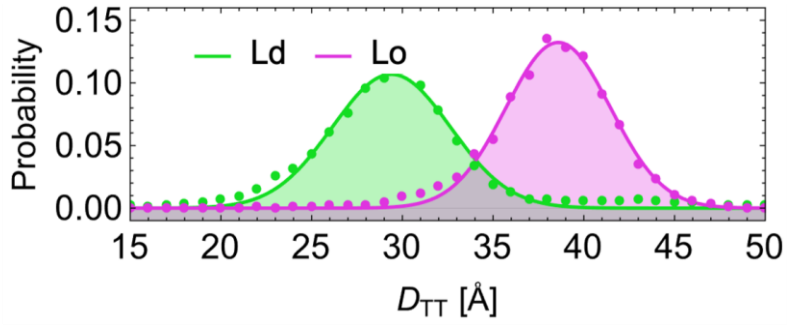


**Figure 4.1 Bilayer thickness distribution.** Bilayer thickness distribution for tieline endpoint compositions.

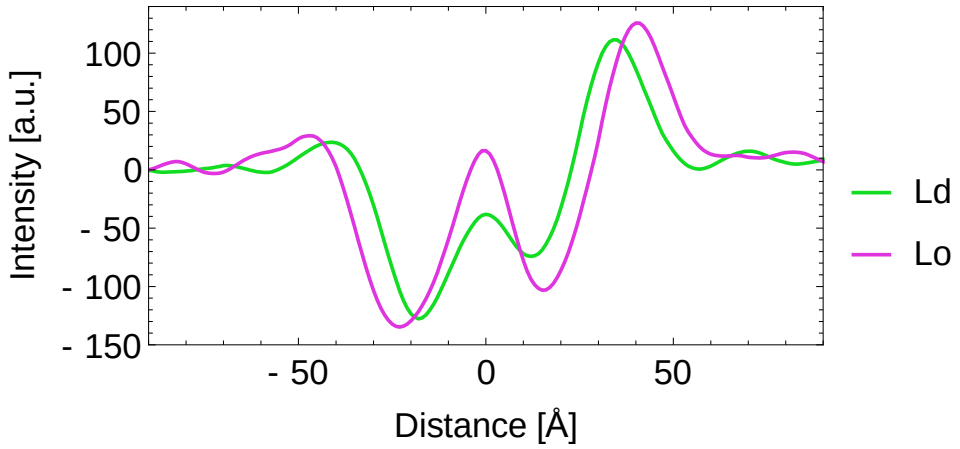


**Figure 4.2 Average intensity profiles for tieline endpoints.** Lo profile has higher trough to distance and contrast.

The ML method was significantly more accurate than methods that relied solely on thickness measurements, and enabled us to characterize phase area fractions, and distributions of domain sizes and numbers. In this chapter, we extend our machine learning approach from in silico to in vitro. By preparing liposome samples along a known thermodynamic tieline of a 3-component lipid mixture, we are able to use supervised learning to classify the bilayer phase state with 5 nm lateral resolution [137]. We find that real-world samples present greater variability in sample conditions (e.g., vesicle composition, ice thickness) and instrument parameters (e.g., defocus length) that complicate analyses compared to the highly controlled in silico datasets. At the same time, these data offer unique insight into the heterogeneity of domain structures in phase-separated systems that is obscured in ensemble-averaged spectroscopic or scattering measurements. These advancements offer potential for enhancing our understanding of membrane organization at a more detailed spatial resolution.

## 4.3 Material and methods

### 4.3.1 Materials

Phospholipids 1,2-dioleoyl-sn-glycero-3-phosphocholine (DOPC), 1,2-distearoyl sn-glycero-3-phosphocholine (DSPC), and 1-palmitoyl-2-oleoyl-sn-glycero-3-[phospho-rac-(1-glycerol)] (sodium salt) (POPG) were purchased from Avanti Polar Lipids (Alabaster, AL). Cholesterol was purchased from Nu-Chek Prep (Elysian, MN). All phospholipids and cholesterol were dissolved in HPLC-grade chloroform and stored at -20°C until use. The concentration of lipids and cholesterol was determined gravimetrically assuming two tightly bound waters for phospholipids. Ultrapure water was obtained from a Milli-Q IC 7000 purification system (Millipore Sigma, Burlington, MA).

### 4.3.2 Sample compositions

For our investigation, we chose DSPC/DOPC/Chol [128, 129], a three-component mixture that has been extensively studied with a wide variety of experimental techniques including confocal microscopy [130], FRET [53], X-ray scattering [92], and neutron scattering [57]. The room temperature phase diagram contains a region where the Ld and Lo phases coexist, making it a useful model for lipid rafts. In the study described in Chapter 3, we simulated

cryo-EM images of vesicles along a tieline that included the composition DSPC/DOPC/Chol 39/39/22 mol% and developed ML methods to analyze the data. Our goal here was to deploy this methodology on real-world data. To this end, we examined seven extruded liposome samples along the same tieline, referred to here and throughout as samples A1-A7 (Table 4.1 and Fig 4.3). The tieline endpoint compositions A1 and A7 were expected to show uniform Ld and Lo vesicles, respectively, while compositions A2-A6 were expected to show the coexistence of Ld and Lo, with the fraction of Lo increasing upon moving rightward along the tieline. To ensure unilamellarity of the vesicles, 5 mol% of the low-melting lipid DOPC was replaced with the low-melting lipid POPG.

### 4.3.3 Preparation of LUVs for cryo-EM

Aqueous lipid dispersions with a total lipid concentration of 3 mg/mL were created by combining appropriate volumes of lipid stocks in chloroform using a glass Hamilton syringe. The solvent was evaporated using an inert gas stream, and the sample was kept under vacuum overnight. The dry lipid film was hydrated with ultrapure water at 55°C. The samples were kept at 55°C for approximately 1 hour with intermittent vortex mixing. The resulting multilamellar vesicle (MLV) suspension underwent five freeze/thaw cycles between a -80°C freezer and a 55°C water bath. Large unilamellar vesicles (LUVs) were generated by extruding the suspension through a 0.1 mm polycarbonate filter using a handheld mini extruder (Avanti Polar Lipids) heated to 55°C. The suspension was extruded through the filter 31 times. The size and polydispersity of each LUV preparation were evaluated using dynamic light scattering (LiteSizer 100, Anton Paar USA, Vernon Hills, IL) immediately after preparation and immediately before cryo-preservation, which typically occurred 2-3 days after preparation.

### 4.3.4 Cryo-EM data collection

LUV samples were cryopreserved by applying a 4 µL aliquot to a Quantifoil 2/2 carbon-coated 200 mesh copper grid (Electron Microscopy Sciences, Hatfield, PA) that was glow-discharged for 30 sec at 20 mA in a Pelco Easi-Glow discharge device (Ted Pella, Inc., Redding, CA). After manual blotting at room temperature (~ 22°C), the grids were plunged into liquid ethane cooled with liquid $N_2$. Cryo-preserved grids were stored in liquid $N_2$ until use.

**Table 4.1.** Sample compositions in this study (in mole percent).

| Sample | DSPC mol% | DOPC mol % | POPG mol% | Chol | Lo mole% |
|---|---|---|---|---|---|
| A1 | 9 | 74 | 5 | 12 | 0 |
| A2 | 17 | 63 | 5 | 15 | 17 |
| A3 | 26 | 52 | 5 | 17 | 33 |
| A4 | 34 | 41 | 5 | 20 | 50 |
| A5 | 43 | 29 | 5 | 23 | 67 |
| A6 | 51 | 18 | 5 | 26 | 83 |
| A7 | 60 | 6 | 5 | 29 | 100 |

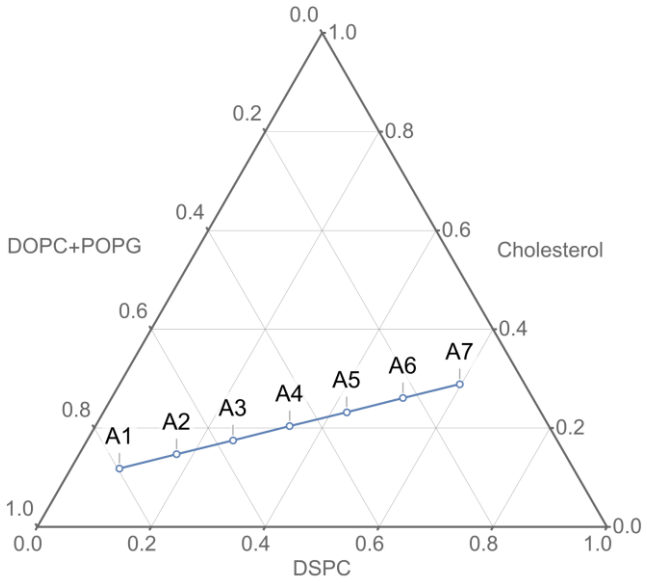


**Figure 4.3 Lipid compositions of systems under study.** All seven compositions lie on a thermodynamic tieline of the mixture DSPC/DOPC+POPG/Chol at 20°C. The tieline endpoints are denoted as A1 (representing a pure Ld phase of fixed composition) and A7 (representing a pure Lo phase of fixed composition). For the intermediate points along the tieline (A2-A6), the only variation occurs in the relative amounts of the Ld and Lo phases.

Cryo-EM image collection was performed at ~ 2 μm under focus on a FEI Polara G2 operated at 300 keV equipped with a Gatan K2 Summit direct electron detector operated in counting mode. Data collection was conducted in a semi-automated fashion using Serial EM software operated in low-dose mode. Briefly, areas of interest were identified visually and 8×8 montages were collected at low magnification (2400×) at various positions across the grid and then individual areas were marked for automated data collection. Data was collected at 2.7 Å/pixel. Movies of 30 dose-fractionated frames were collected at each target site with the total electron dose being kept to < 20 $e^{-}/Å^2$. Dose-fractionated movies were drift-corrected with MotionCor2.

### 4.3.5 Bilayer intensity profiles

Vesicles were identified and subdivided as previously described to obtain spatially resolved intensity profiles in the direction normal to the bilayer, referred to here as $I(w)$ profiles, with $w = 0$ corresponding to the bilayer midplane [67]. A set of points approximating the midplane of the projected bilayers were generated using a neural network-based algorithm known as MEMNET which is part of TARDIS software package [127]. The contour obtained from these points was divided into 5 nm segments along the arc length and 10 nm normal to the contours in each direction, resulting in a polygonal representation of the 2D contour. In the resulting 5×20 nm rectangular region, all pixels were selected. The average intensities of the pixels were binned at 1 Å interval in the direction normal to the contour to generate a local *I(w)* profile.

### 4.3.6 Bilayer thickness measurement

A crucial metric derived from $I(w)$ profile is the spatially resolved bilayer thickness, denoted as $D_{TT}$, with detailed procedures outlined in previous papers [67]. In summary, $D_{TT}$ was determined as the distance between the two minima in the $I(w)$ profile. Two methods were used to estimate the position of these minima on either side of $w$ = 0. The reported $D_{TT}$ values represent the average of the measurements obtained from both methods.

### 4.3.7 Machine learning (ML) classification of bilayer phase state

ML analyses were performed in Wolfram Mathematica 13.2 (Wolfram Research, Champaign, IL). We used two supervised machine learning methods, Gradient Boosted

Trees (GBT) and Logistic Regression (LR). These methods were chosen because of their superior performance in our previous in-silico study [137]. The models were trained on data from tieline endpoint samples A1 and A7 corresponding to pure Ld and Lo phases, respectively. The training features were the raw $I(w)$ profiles (i.e., 201-dimensional vectors of intensity values) from 5 nm length bilayer segments and their corresponding vesicle radii. Because extruded vesicle sizes are not uniformly distributed, and because different samples typically have different total numbers of vesicles, care must be taken to avoid biasing the model. Accordingly, segments were first binned by vesicle size, and an identical number of segments was then randomly selected from within each bin to produce a training set of 6000 segments each from samples A1 and A7. Validation data consisted of 2000 segments each from A1 and A7. When deployed on input segments, the two trained ML models each provide an estimate of the probability that a given segment is Lo, which we define as the segment's ordered character or OC (OC ∈ [0,1]).). We used the average OC value from the GBT and LR models for subsequent analysis including phase classification. Specifically, segments were classified as Ld or Lo phase using a binary threshold of OC* = 0.5. The first round of training and deployment revealed a minor presence of Lo phase within sample A1. We subsequently retrained the models after first eliminating segments from A1 whose OC values exceeded 0.75. A correction was implemented to eliminate isolated segments (i.e., those with phase classification different from their two nearest neighbors), which would otherwise lead to the erroneous division of a continuous domain into two or more discontinuous domains [137].

### 4.3.8 Phase area fractions

For samples on the same thermodynamic tieline, phase area fractions can be calculated from the Lever Rule provided that the average molecular areas of the two phases are known. For a tieline of Ld + Lo coexistence, the area fraction of Lo phase, $a_{Lo}$, as a function of the mole fraction of Lo phase, $\chi_{Lo}$, is calculated as:

$$a_{Lo}(\chi_{Lo}) = \frac{\chi_{Lo}A_{Lo}}{\chi_{Lo}A_{Lo} + (1-\chi_{Lo})A_{Ld}}, \qquad (4.1)$$

where $A_{Ld}$ and $A_{Lo}$ are the average molecular areas of the Ld and Lo phases, respectively. We used published values of 43.3 Å$^2$ for $A_{Lo}$ and 63.1 Å for $A_{Ld}$ [2 92].

## 4.4 Results and Discussion

### 4.4.1 Initial results for tieline compositions

Given our expectations from the published 23°C phase diagram,[128] we were surprised to observe 8% Lo phase fraction in the vesicles of sample A1 (Fig.4.4). To deal with this, we removed the Lo phase segments from the A1 dataset and re-trained the models using only the Ld segments as described in Methods. Pinpointing the source of the discrepant phase behavior is beyond the scope of this study, but we can speculate on some potential explanations. First is the compositional uncertainty inherent both to LUVs prepared by dry film hydration and GUVs prepared by electroformation,[138] the latter of which were used by Zhao et al. to determine the phase boundaries.[128] Second is the inclusion of 5 mol% POPG in cryo-EM vesicles that was absent from the GUV study. Third is the large difference in curvature of ~ 100 nm diameter LUVs compared to ~ 20 μm diameter GUVs, which could in principle shift the phase boundaries.

### 4.4.2 Segment intensity profiles contain the signatures of Ld and Lo phases

Figure 4.5 shows several representative segment intensity profiles of Ld (green) and Lo (pink) phases. For Lo profiles, the outer trough is more pronounced, and the distance between the outer and inner troughs ($D_{TT}$) is greater (i.e., a larger bilayer thickness), compared to Ld profiles. The overall contrast, defined as the intensity difference between the outer peak and inner trough, is generally larger for Lo segments compared to Ld. Similar observations can made in the average intensity profiles of all segments from A1 and A7 shown at the bottom of Fig. 4.5, where the shaded area denotes ±1 standard deviation. The spatially resolved intensity profiles thus contain signatures from the two classes of phase behavior (i.e., Ld and Lo) and were used as the primary features for ML analyses.

### 4.4.3 Phase classification using bilayer thickness

Our initial analysis focused on segment $D_{TT}$ values. We observe that average $D_{TT}$ increases systematically from sample A1 to A7, consistent with the increasing concentration of high-melting lipid DSPC (Fig. 4.6) and cholesterol. The probability distributions of segment thicknesses $D_{TT}$ for each system are shown in Fig.4.7a.

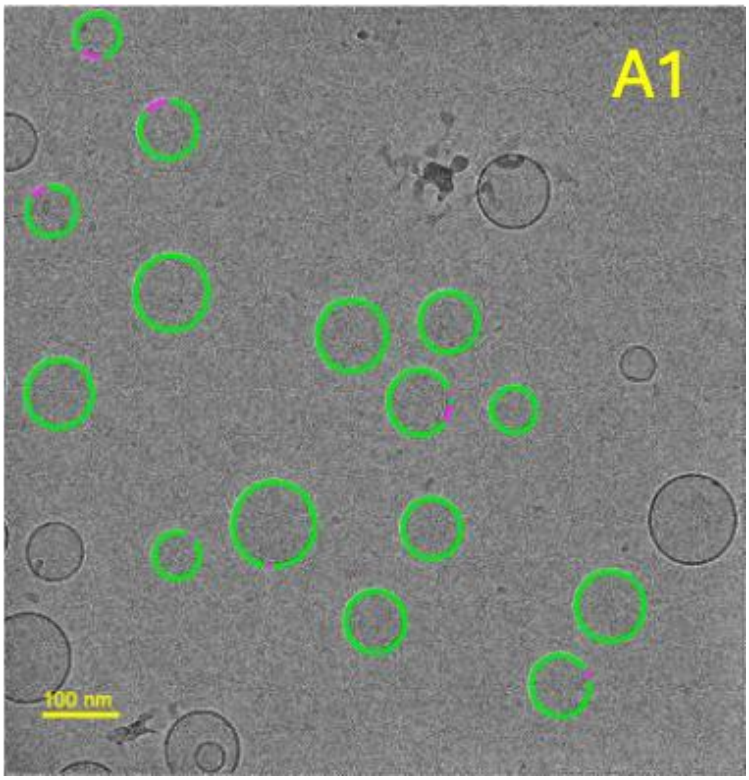


**Figure 4.4 Presence of Lo phase in sample A1.** A small amount of Lo phase (pink) was observed in some vesicles in sample A1, which according to existing phase diagrams should have been purely Ld phase (green).

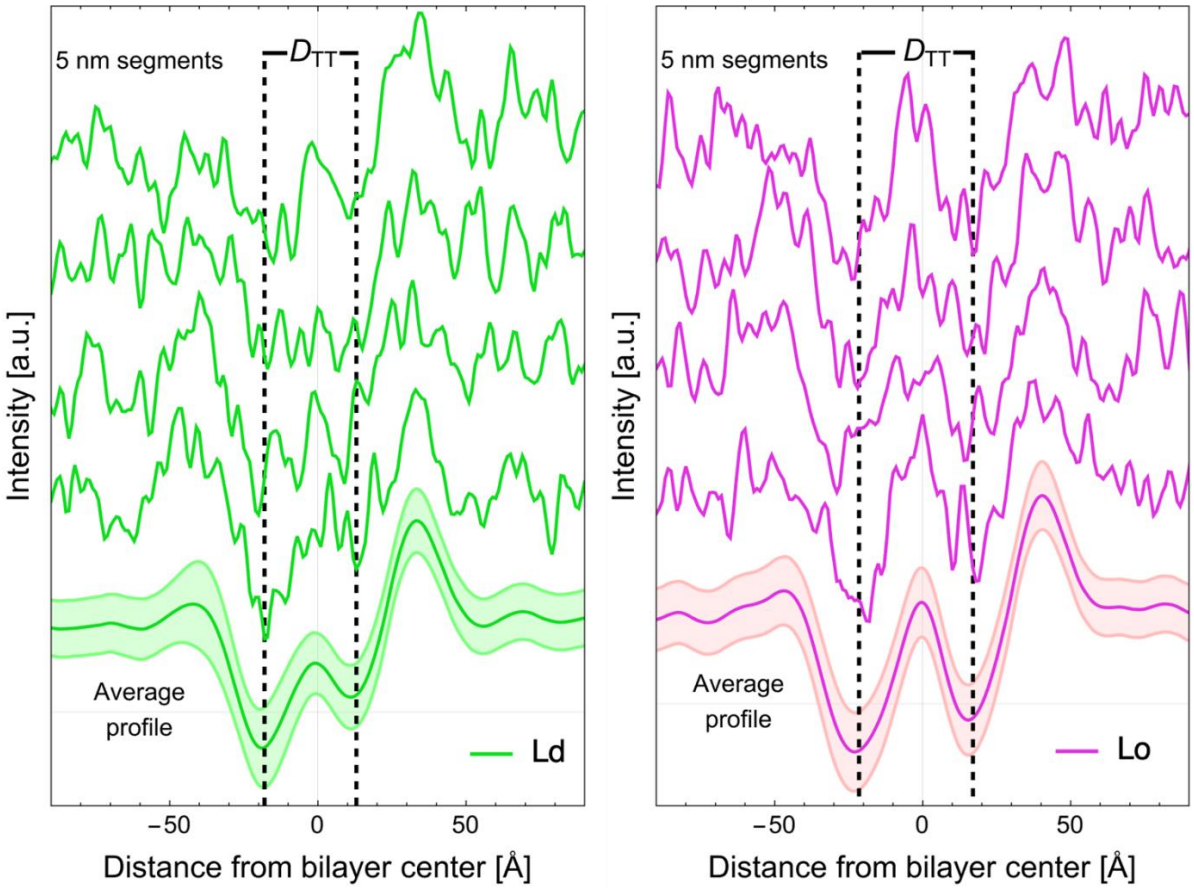


**Figure 4.5 Segment intensity profiles.** Comparison of Ld (green) and Lo (pink) intensity profiles. For Lo, the outer trough is more pronounced, $D_{TT}$ is larger, and contrast is greater as compared to Ld as shown in four randomly chosen 5 nm segments at the top. A similar observation is made in the average intensity profiles of all segments from A1 and A7 shown at the bottom, where the shaded area denotes $\pm 1$ standard deviation.

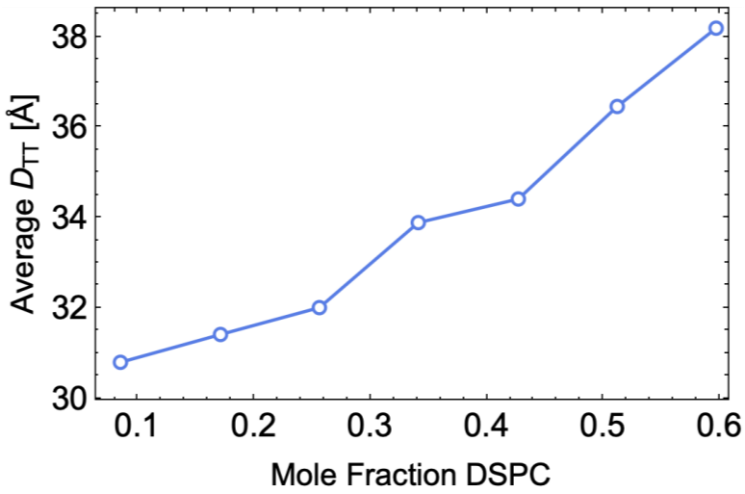


**Figure 4.6 Bilayer thickness of tieline samples.** The average bilayer thickness increases with the amount of DSPC in the sample.

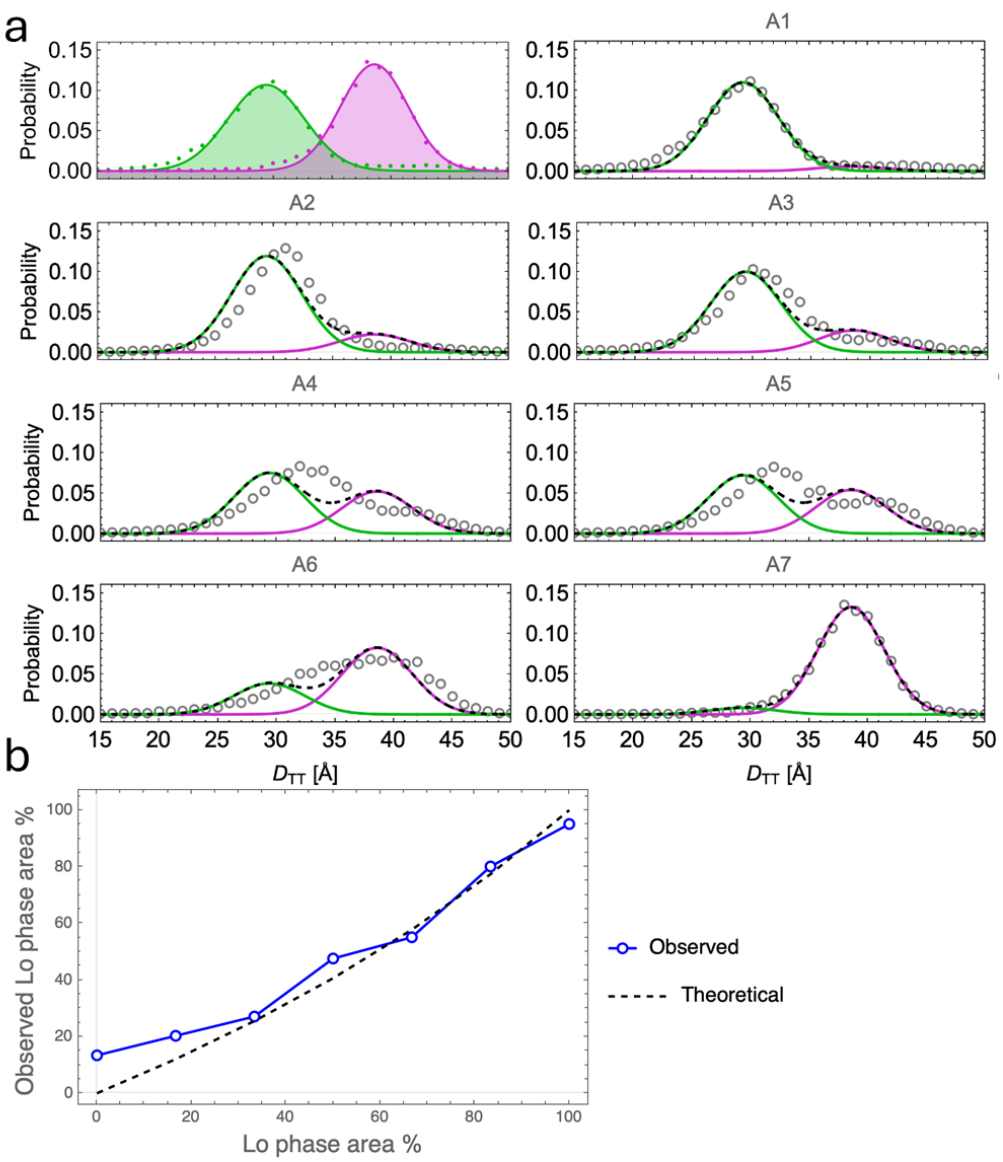


**Figure 4.7 Bilayer thickness distributions and Lo phase percentage.** a) The panel on the top left shows the overlap between Lo and Ld thickness distributions. The remaining panels show the experimental thickness distributions for each system (open symbols) and fits to a constrained 2-gaussian model (solid lines). b) The Lo area percentage estimated using $D_{TT}$ follows the correct trend but does not align well for samples with low Lo phase fraction.

Segment thicknesses are distributed approximately normally for the single-phase Ld and Lo datasets A1 and A7 (Fig. 4.1), with a mean $D_{TT}$ of 30.8 Å for A1 and 38.2 Å for A7. Datasets A2-A6 show non-Gaussian behavior due to the coexistence of Ld and Lo phases within the vesicles. We modeled these distributions as a weighted sum of Gaussian functions corresponding to the Ld and Lo endpoints, with the mean values fixed to 30.8 Å and 38.2 Å. The model did not fit well for thinner bilayers in this experimental data, though it performed well in the simulated systems discussed in Chapter 3. The area under the curve obtained from modeling was used to estimate the phase area fractions for each dataset. Fig. 4.7b compares the Lo phase fraction obtained from modeling the thickness distributions (symbols) to the Lo phase fraction calculated from the Lever Rule and published values of the Ld and Lo molecular areas (dashed lines). This method was in reasonably good agreement for systems with high amounts of Lo phase, making it less reliable for analysis.

### 4.4.4 Phase classification using supervised machine learning

Next, we used two supervised ML methods (GBT and LR) as described in Methods. These methods yield predictions for the probability that a given segment is Lo phase, which we term the segment's ordered character $(\mathrm{OC})$. Segments with OC > 0.5 were classified as Lo, and segments with OC < 0.5 were classified as Ld. Fig. 4.8a plots the fraction of all segments classified as Lo for each tieline sample (symbols), revealing good agreement with the Lo area fraction calculated from the Lever Rule (dashed line). Further, when moving from A2 to A6, the ratio of Lo domain size to vesicle size increases, while that of Ld domains decreases (Fig 4.8b). Interestingly, we observe multiple domains in individual vesicles (Fig. 4.9). We discuss this observation, as well as the influence of vesicle orientation, in the subsequent sections.

### 4.4.5 Ensemble-averaged intensity profiles of Ld and Lo phases

Intensity profiles contain the signature features of the phase to which a segment belongs. Further, the electron scattering profile of the bilayer can in principle be reconstructed from the intensity profiles, making cryo-EM a potential candidate to complement established methods like neutron and X-ray scattering for bilayer structure determination [78, 86].

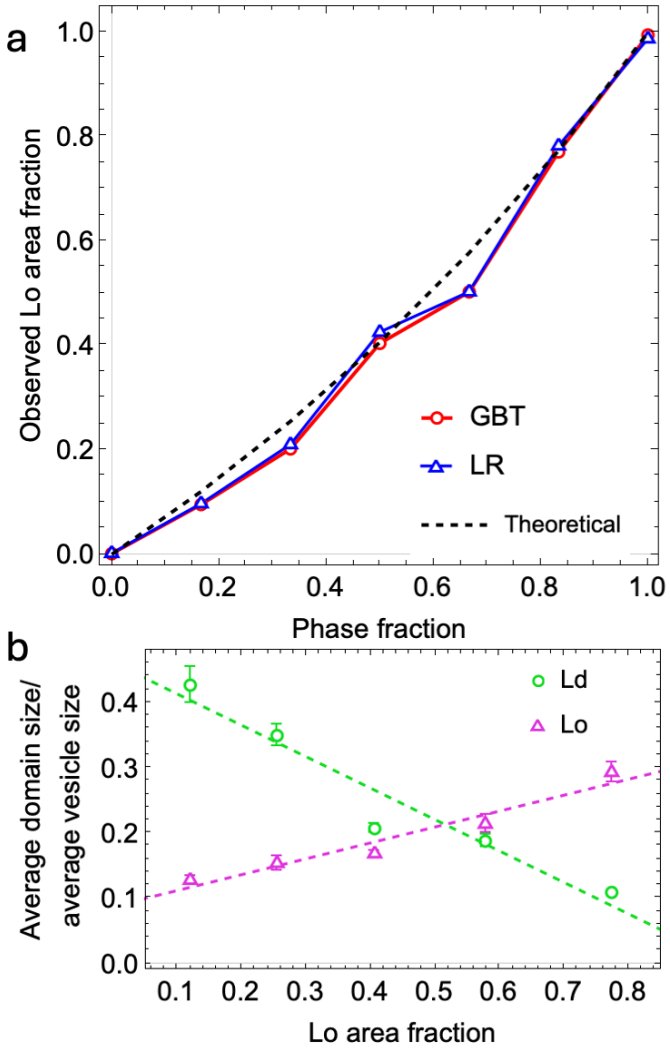


**Figure 4.8 Ensemble average area fraction and domain size.** a) Area fraction of Lo phase obtained for each system using GBT and LR models. b) The ratio of average domain size and average vesicle size given for each system.

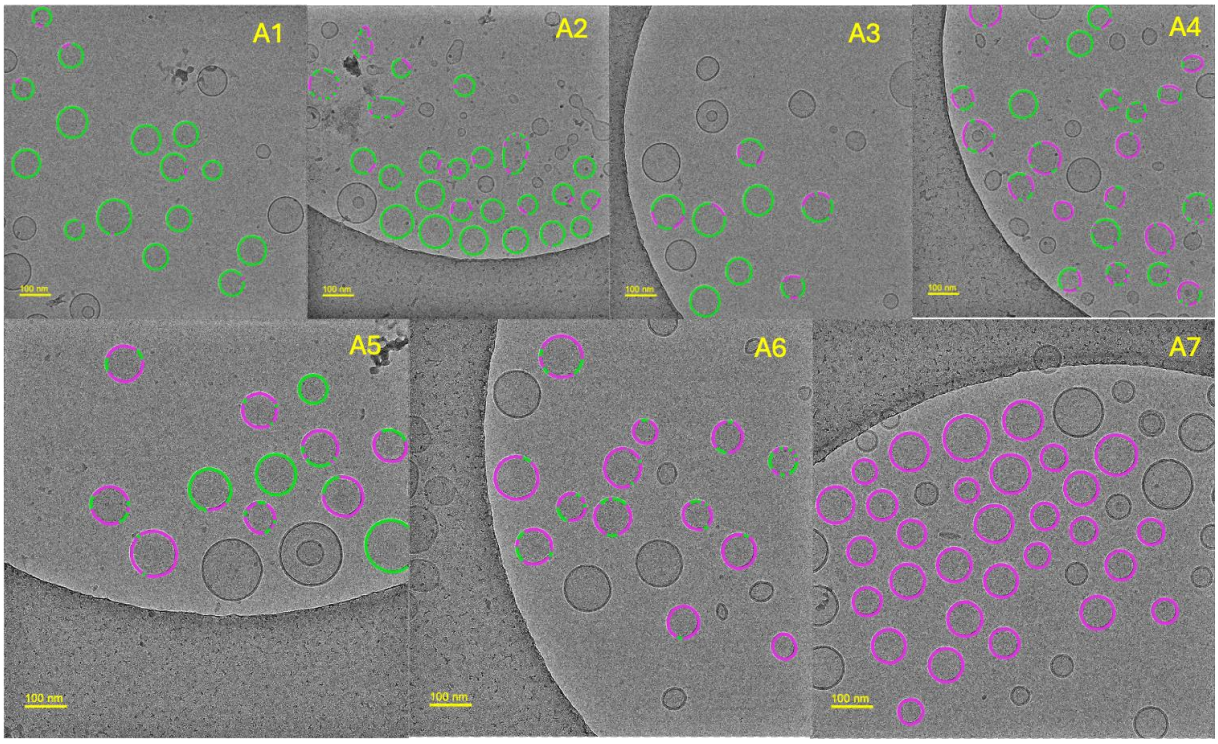


**Figure 4.9 Classification results on all seven systems.** Segments classified as Ld are shown in green whereas segments classified as Lo are shown in pink. System A1 shows the presence of some Lo phase. These segments were removed from the Ld training dataset in the second round.

When bilayers are phase-separated, cryo-EM also allows us to determine the phase state of individual segments, thus providing a distinct advantage over traditional scattering techniques that produce a single curve representing the average of any coexisting phases. Fig. 4.10 plots the mean intensity profiles of Ld (green lines) and Lo (pink lines) segments for phase-separated samples A2-A6, as well as those calculated from tieline endpoint samples A1 and A7 (black lines). The Ld and Lo profiles, despite coming from liposomes with different overall composition, are nevertheless similar. This is consistent with the thermodynamic requirement that samples on the same tieline have the same coexisting phases (here, composition A1 and A7), with only the relative amounts of the two phases changing. Additionally, Fig. 4.10b shows that the $D_{TT}$ values calculated from the mean Ld and Lo intensity profiles of samples A2-A6 (open symbols) were each within 2 Å of $D_{TT}$ values calculated from samples A1 and A7 (dashed lines). These results are similar to those obtained in the simulation study (Fig. 3.19)[137, 139], but with slightly greater variation. A key difference between the in silico and in vitro datasets is that experimental vesicles typically showed several domains, compared to a single domain per vesicle in simulations. The presence of multiple domains results in a greater number of boundary segments that possess features of both phases, thereby producing deviations from the average properties observed at the tieline endpoints.

### 4.4.6 Vesicle size effects and domain budding

It is widely recognized that nanoscale membrane curvature is integral to numerous biological processes [131, 132]. Curvature is influenced by factors such as vesicle size, lipid composition, integral membrane proteins or cytoskeletal attachments [133]. Simulation studies further suggest that strong curvature can alter the bilayer structure[134]. To investigate the influence of curvature, we binned the vesicles in each dataset by size and calculated various properties. For example, Fig. 4.11 plots the Lo phase area fractions $a_{Lo}$ vs. vesicle size for phase-separated samples A2-A6, revealing a trend in which $a_{Lo}$ decreases with increasing vesicle size. This trend is obscured in ensemble averages such as those found in Fig. 4.8a. Consistent with the trend, we find numerous small vesicles that appear to be entirely Lo phase together with larger vesicles that appear to be entirely Ld phase (Fig. 4.12), an observation that suggests a high propensity for domain budding.

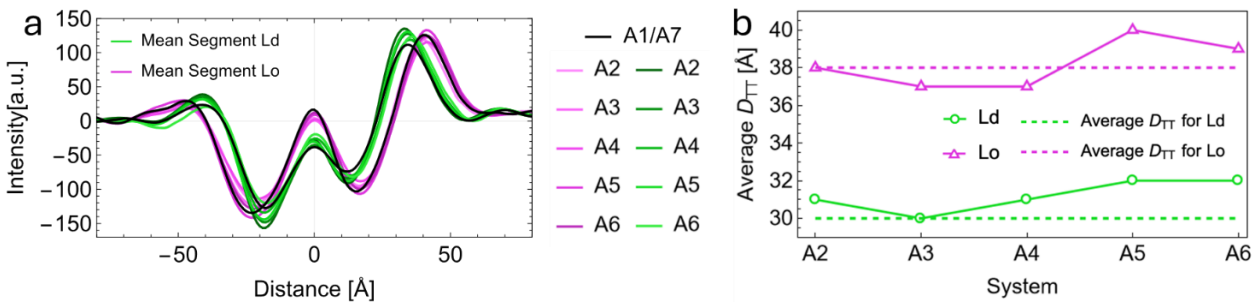


**Figure 4.10 Average intensity profiles and $D_{TT}$ values.** (a) After classification, the mean intensity profile for all Lo (Ld) segments is illustrated in pink (green) for each phase-separated dataset (A2-A6), whereas the mean intensity profiles of pure Ld and Lo (datasets A1 and A7, respectively) are presented in black. (b) Average $D_{TT}$ values estimated from the mean intensity profiles shown in (a) for each phase separated system. Dashed pink and green lines represent the average $D_{TT}$ value of the pure Ld and Lo datasets.

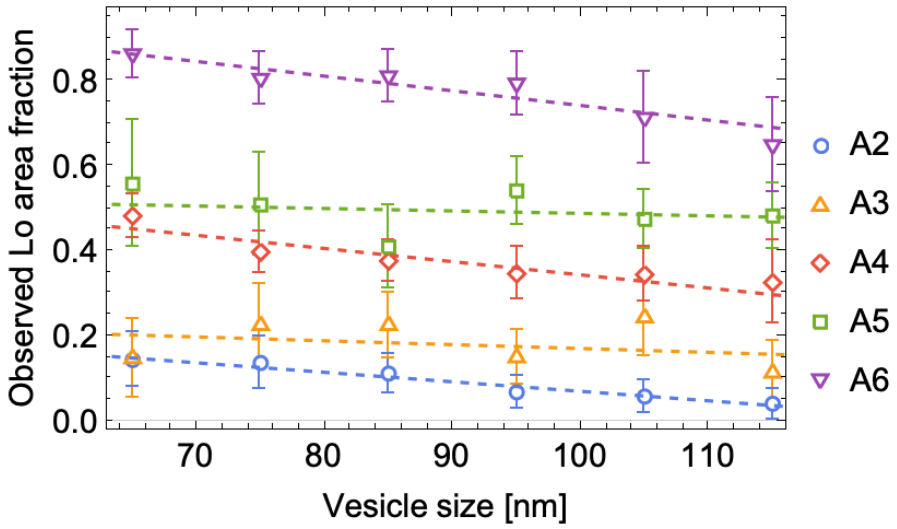


**Figure 4.11 Size binned Lo area fraction.** Area fraction shows a decreasing trend with an increase in vesicle size.

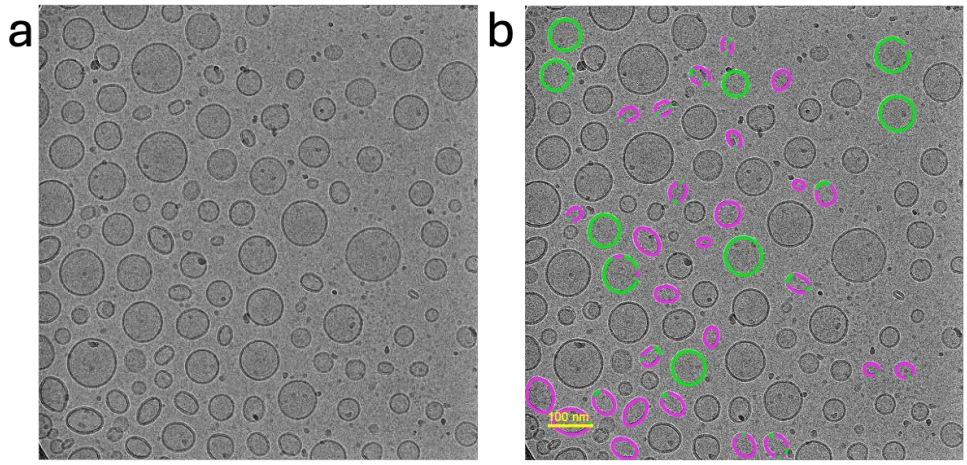


**Figure 4.12 Budding in vesicles.** Smaller Lo phase buds were identified in sample A4, exclusively containing Lo phase components, along with larger parent vesicles made up of pure Ld phase.

in these samples, presumably driven by a large line tension. Indeed, cryopreservation captured some vesicles that were in the process of budding (Fig. 4.13), lending further support to this hypothesis. In light of these observations, it is likely that the trend in Lo area fraction vs. vesicle size is largely the result of domain budding, rather than a shift in the Ld + Lo phase boundary induced by vesicle curvature.

We also evaluated the influence of curvature on domain size. We restricted this analysis to vesicles in which the total number of Lo and Ld domains was less than 10. Vesicles with 10 or more domains would distort the average, pulling it toward a smaller value. Fig. 4.14 shows the results of this analysis for Ld domains (top) and Lo domains (bottom). Domains of Ld phase (which is typically the continuous phase in GUVs) showed a clear increase in size with increasing vesicle size for samples A2 to A6. Comparing the different samples, Ld domain size also increases with increasing Ld phase fraction (i.e., from right to left along the tieline) as expected. Similar trends were observed for Lo domains with the exception of sample A2, where Lo domain size appears to decrease with increasing vesicle size. We speculate that this discrepancy is caused by relatively weaker statistics for this sample combined with a vesicle orientation effect, in which domains of the minority phase might not appear in a given vesicle projection simply because of its orientation with respect to the electron beam.

### 4.4.7 Vesicle-to-vesicle heterogeneity

Although ensemble average measurements of bilayer properties often provide valuable insights, such averages can obscure the heterogeneity between vesicles. Compared to other techniques, cryo-EM coupled with ML has the advantage of revealing variability in the characteristics of individual vesicles. One notable example is the frequent non-spherical vesicle shapes seen in Fig. 4.9 and 4.12. Additional examples are shown in Fig. 4.15 and Fig. 4.16, which plot histograms of Lo area fraction and number of Lo domains, respectively, from individual vesicles of phase separated samples. These plots reveal substantial vesicle-to-vesicle heterogeneity that cannot be solely attributed to vesicle orientation effects. Instead, we speculate that the underlying cause is compositional heterogeneity.

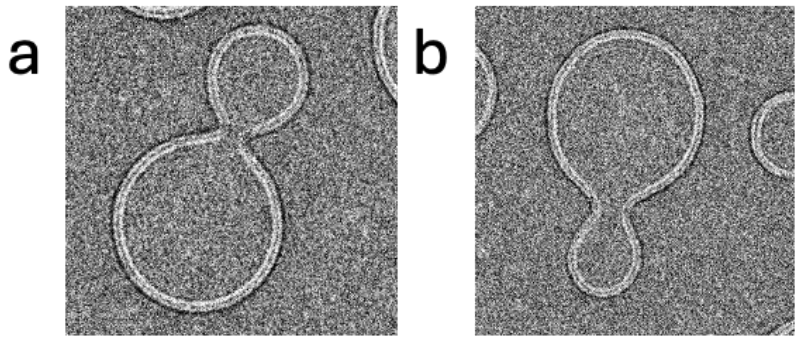


**Figure 4.13 Budding captured in cryo-EM images.** Vesicles undergoing budding frozen at an intermediate state in sample A3.

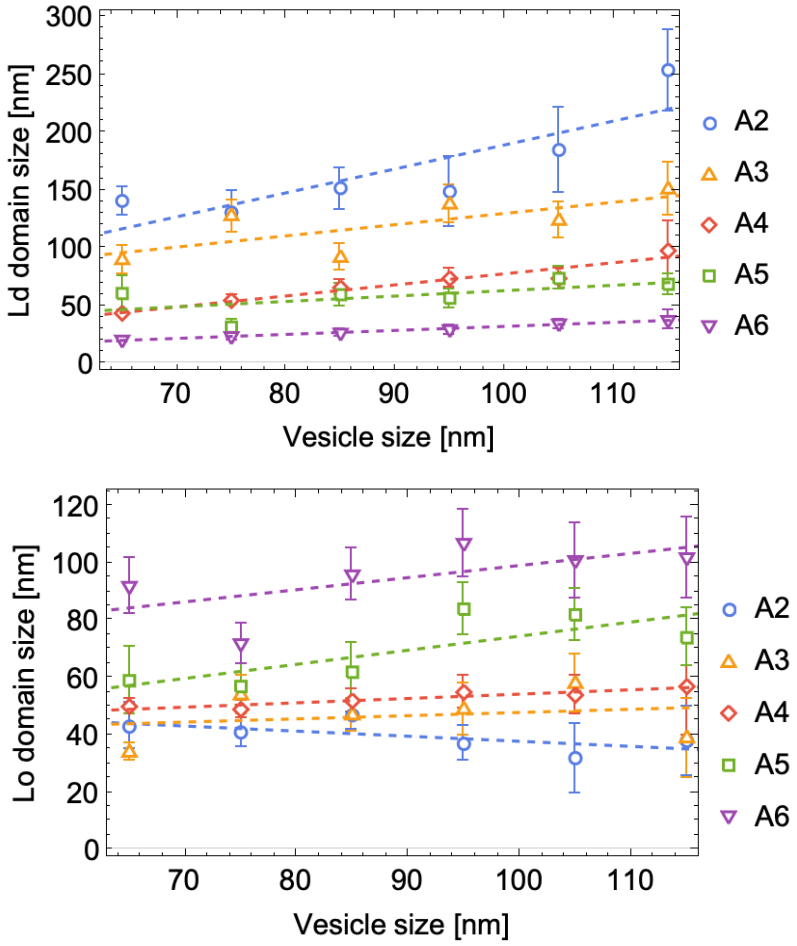


**Figure 4.14 Average Ld and Lo domain size vs. vesicle size.** The domain size shows an increasing trend with an increase in vesicle size.

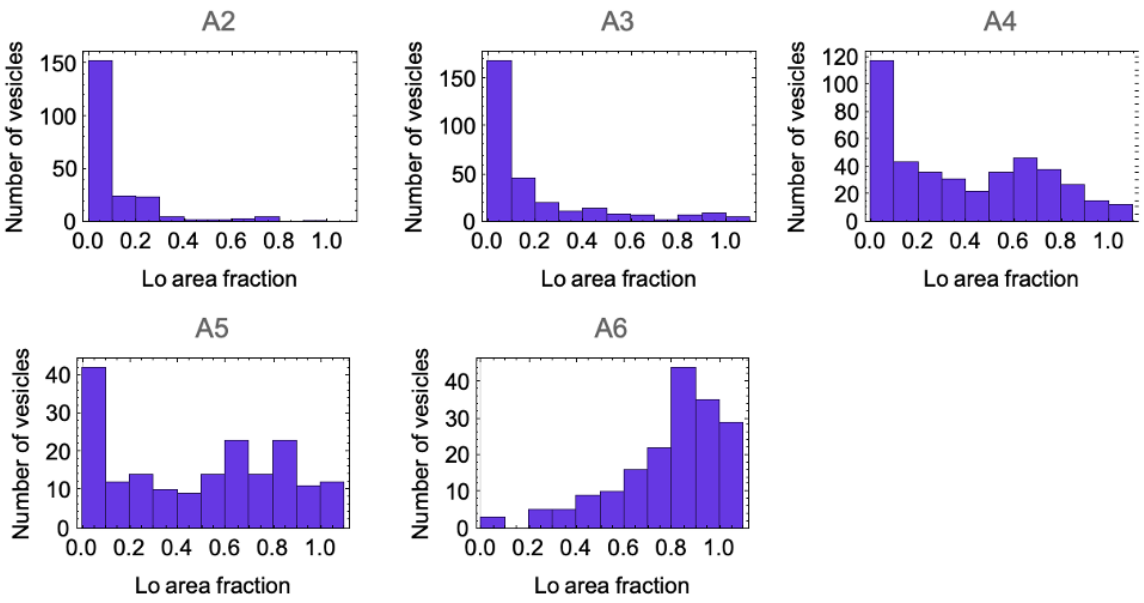


**Figure 4.15 Area fraction distribution.** The distribution of area fraction for systems A2-A6 shows a wide range of heterogeneity.

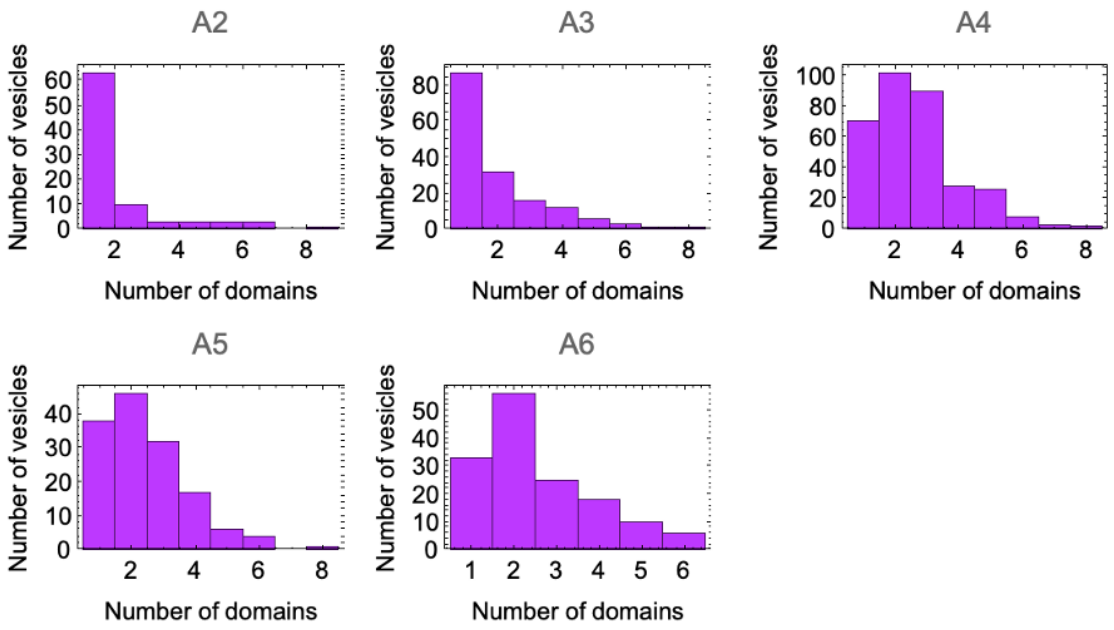


**Figure 4.16 Distribution of number of Lo domains.** The distribution of the number of Lo domains for systems A2-A6 shows a wide range of heterogeneity.

Larsen et al. devised a clever fluorescence assay for vesicle heterogeneity that involved tethering individual liposomes to a glass surface at low densities in order to isolate their signals.[138] Our observations here are consistent with their finding of significant variation in lipid composition among the liposomes of a given preparation[138].

### 4.4.8 Challenges of using cryo-EM

Our use of cryo-EM to investigate phase separation in liposomes presents its own set of challenges. These include variability in physical parameters such as vesicle composition and ice thickness, as well as instrumental parameters like defocus length. Additionally, cryo-EM images have a low contrast-to-noise ratio, which complicates analysis. In certain cases, the orientation of the vesicle may prevent the capture of smaller domains, or the domain boundary may align almost parallel to the projection plane, leading to intensity contributions from both phases within each segment. While the analysis pipeline developed using simulated images with known ground truth proved useful, experimental data presented additional complications. These include the presence of several domains in many vesicles, which resulted in a high number of boundary segments that are challenging to accurately classify. Moreover, trained models tend to predict values near 0 or 1, avoiding intermediate values even for boundary segments with ground truth values that are indeed intermediate. These complexities need to be carefully considered and addressed when utilizing cryo-EM for analysis. Despite the challenges posed by cryo-EM analysis, the ensemble-averaged results align well with findings from other techniques.

## 4.5 Summary and Conclusions

Here, we deployed a novel application of supervised machine learning for characterizing phase separation in experimental cryo-EM images of extruded liposomes. Phase area fraction, domain size for both phases and domain numbers were estimated. Although the ensemble-averaged results from our study align with values for phase area fractions calculated from the Lever Rule, we observed significant heterogeneity in a vesicle-by-vesicle analysis.

This highlights a potential limitation of ensemble averages in spectroscopic and scattering techniques, which might obscure the true properties of the system. Further, these techniques do not consider factors such as budding in vesicles (particularly in phase-separated systems with high line tension) and the non-spherical shape of vesicles, which deviate from assumptions made in many models. The advantage of cryo-EM lies in its ability to analyze systems particle-by-particle, thus offering insights that other techniques may overlook. The presence of numerous domains in the experimental system, in contrast to the single domain of each phase in the simulated study, presents a new challenge. At the 5 nm segment level, there is a higher likelihood of misclassification near domain boundaries, where both phases contribute to the observed signal. To enhance analysis, increasing the number of vesicles per bin size would be beneficial. The future steps could focus on improving the contrast-to-noise ratio, particularly through noise reduction, to refine the analysis further.

# Chapter 5

## Investigating the influence of membrane dipole potential on liquid-ordered/liquid-disordered phase separation in model membranes

A version of this chapter is in preparation to be submitted.

This chapter describes research designed by Karan D. Sharma and Frederick A. Heberle. Experiments and data collection were performed by Karan D. Sharma and M. Neal Waxham. Michael D. Best and Jinchao Lou designed, synthesized and characterized the deuterated ether lipid. Best Data analysis and writing of the manuscript was performed Karan D. Sharma, Jinchao Lou, Michael D. Best, M. Neal Waxham, and Frederick A. Heberle.

## 5.1 Abstract

Cells can dynamically alter the spatial organization of lipids and proteins in the plasma membrane (PM) to regulate processes including cell signaling. The size and morphology of membrane domains, along with their dependence on lipid composition, have garnered significant attention. Model membrane studies have proven valuable for elucidating the influence of phospholipid chains, headgroups, and cholesterol concentration on membrane phase behavior. Following this approach, we investigated simplified three- and four-component models that mimic the composition of the PM outer leaflet to understand the role of the membrane dipole potential originating in the lipid backbone. Replacing ester-linked DPPC and DOPC with their ether-linked counterparts allowed us to selectively change the dipole density of coexisting liquid-disordered (Ld) and liquid-ordered (Lo) phases, while replacing DOPC with POPC allowed us to change the line tension. We used confocal fluorescence imaging of GUVs to gain insight into the macroscopic phase behavior, and FRET, SANS and cryo-EM of LUVs to probe nanoscale heterogeneity. Our results can be understood in terms of a model where the tendency to minimize line tension is counteracted by dipole repulsion, which can in some cases result in stable arrays of small domains or stripe phases. These findings suggest that relatively small changes in the structure of the lipid backbone can influence domain formation and morphology in biomimetic membranes.

## 5.2 Introduction

The composition and structural properties of the lipid bilayer play a critical role in cell function. Membrane properties such as permeability, fluidity, elasticity, and thickness

regulate process including the selective transport of materials across the cell, protein sorting, signaling, and the membrane's response to external stimuli. The membrane's mechanical and structural properties result from a complex interplay between the hundreds of components of the bilayer. While the compositional complexity and dynamic behavior of biological membranes make it a very difficult task to understand the role of individual lipids, a physicochemical approach that groups lipids by common characteristics can often yield insight.[20] A notable example is the lipid raft model, which postulates that favorable interactions between saturated lipids and cholesterol give rise to microdomains that are surrounded by a matrix of mostly unsaturated lipids.[79] Lipid rafts are hypothesized to influence cell signaling, trafficking, and even the pathogenesis of certain viruses and bacteria.[19] The mechanisms and conditions of raft formation are unclear. Understanding the interactions between the different lipids that comprise the plasma membrane can provide insight into the underlying mechanisms of many biological processes that depend on rafts.

An interesting model for the PM. outer leaflet composition is DSPC/DOPC/POPC/cholesterol, mixtures of which exhibit a transition from nanoscopic to microscopic domains as DOPC replaces POPC.[140] This transition passes through a small window of composition in which modulated phase patterns appear. These modulated phase patterns have also been observed in asymmetric model membranes and GPMVs.[103] Adjusting the lipid composition or introducing asymmetry in lipid vesicles was found to control domain size and morphology within a small composition space. This finding offers insight into a potential mechanism by which cells can create lateral heterogeneity in the plasma membrane by fine-tuning the local membrane composition.

A simple model that has been proposed as an explanation for modulated phases considers a competition between line tension and an electrostatic repulsion arising from permanent dipoles in the lipids (Fig. 5.1).[141]

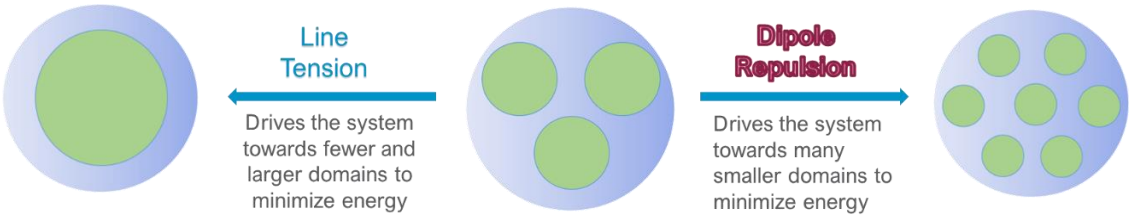


**Figure 5.1 Competing interactions model.** The hypothesis of the competing interactions model is that line tension drives the system towards fewer and larger domains by minimizing the perimeter of domain boundary whereas dipole repulsion drives the system towards many smaller domains.[141]

Although the in-plane components of the dipole moments are expected to cancel in a fluid bilayer, the component of the carbonyl dipole that is parallel to the bilayer normal does not, and thus can generate a repulsive force over a distance of several nanometers provided the local dielectric strength is low.[141] In a phase separated bilayer where the dipole densities of the two phases are different, dipole repulsion could therefore act to break up large domains of high dipole density. This dispersive force is opposed by the line tension, which acts to promote phase separation by driving the system towards fewer, larger domains to minimize unfavorable lipid contacts. In the context of regular solution theory, line tension can be related to the unfavorable pairwise interaction energy between unlike lipids, for example lipids with saturated and unsaturated chains. At a molecular level, the thickness mismatch between ordered and disordered domains is known to be a major contributor to the line tension.[57] Line tension is relatively straightforward to measure experimentally using flicker spectroscopy, with typical values ranging from 0.1-2 pN in membranes exhibiting Ld + Lo phase separation.[141, 142] On the other hand, experimental measurements of the absolute value of the membrane dipole potential are more challenging, with estimates obtained from different methods varying between 200-1,000 mV.[86] Notably, experimental observations and MD simulations show significantly lower dipole potentials for phospholipids containing an ether linkage compared to those with a conventional ester linkage.[143]

Both simulation and theory have provided insight into the competing interactions model. Using Monte Carlo simulations, Amazon and Feigenson showed that the critical line tension required for phase separation is highly sensitive to the dipole density mismatch between Ld and Lo phases.[144] Usery et al. developed a simple analytical model that treats the Lo phase as a disk of dipoles and reached a similar conclusion.[141] Here, we provide what is to our knowledge the first rigorous experimental test of these models. We first show that the dipole density of Ld and Lo phases can be systematically altered by substituting ether-linked glycerophospholipids for their ester-linked counterparts (Fig. 5.2).

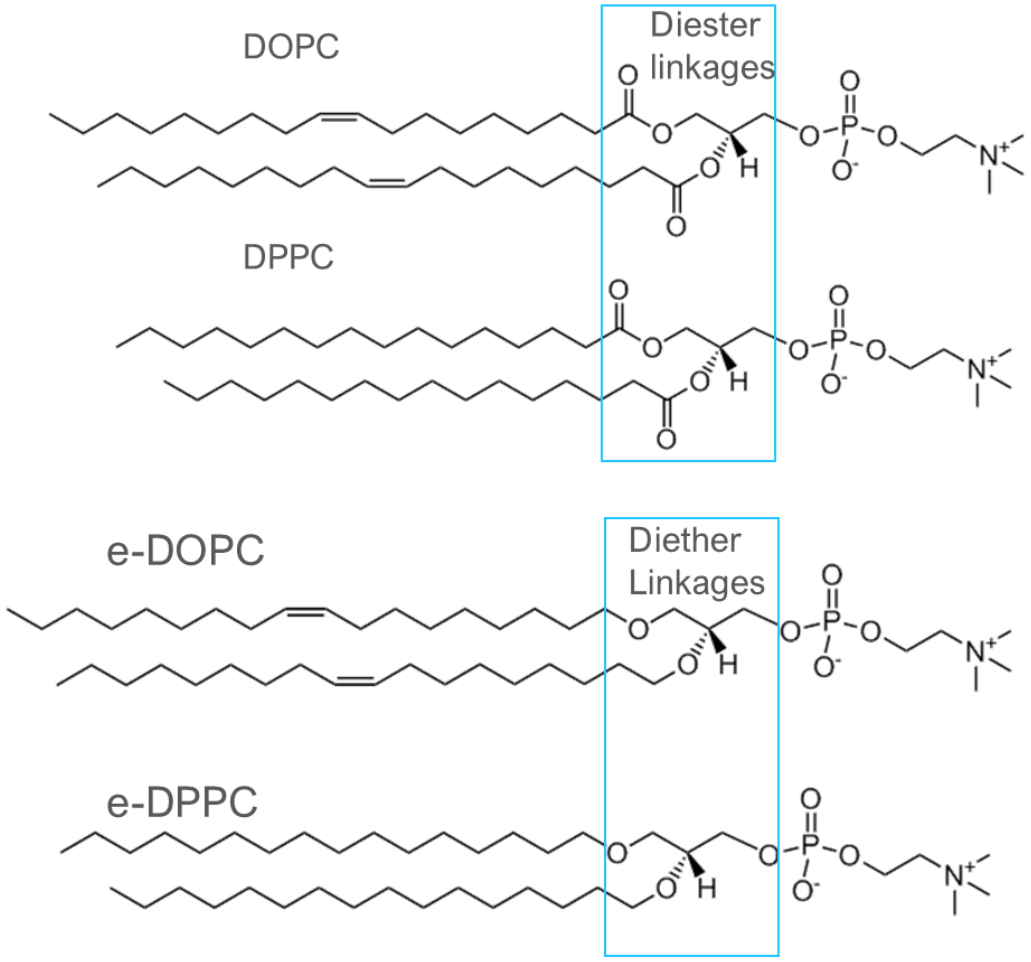


**Figure 5.2 Structure of lipids under study.** The structures of ester and ether linked DPPC and DOPC.

To prove this, we use an electrochromic fluorescent lipid probe to measure the relative dipole potential of Ld and Lo phases with different combinations of ester-linked and ether-linked lipids. For each of these combinations, we then assessed the phase behavior while systematically varying the line tension through changes in either temperature or composition. To access domain length scales ranging from nanometers to microns, we use a suite of spectroscopic (FRET and SANS) and imaging (confocal microscopy and cryo-EM) techniques with different spatial resolutions. These measurements reveal a strong correlation between dipole density mismatch of Ld and Lo phases and the critical line tension for macroscopic phase separation, thus validating a key prediction of the competing interactions model.

## 5.3. Materials and Methods

### 5.3.1 Materials

Phospholipids 1,2-dioleoyl-sn-glycero-3-phosphocholine (18:1-PC, DOPC), 1,2-dipalmitoyl-sn-glycero-3-phosphocholine (16:0 PC, DPPC), 1-palmitoyl-2-oleoyl-glycero-3-phosphocholine 16:0-18:1 PC (POPC) were purchased from Avanti Polar Lipids (Alabaster, AL). The diether analogues of these phospholipids, 1,2-di-O-(9Z-octadecenyl)-sn-glycero-3-phosphocholine (18:1 Diether PC, eDOPC), 1,2-di-O-hexadecyl-sn-glycero-3-phosphocholine (16:0 Diether PC, eDPPC) and 1-O-hexadecanyl-2-O-(9Z-octadecenyl)-sn-glycero-3-phosphocholine (16:0-18:1 Diether PC, ePOPC) were purchased from Avanti Polar Lipids (Alabaster, AL). 1-palmitoyl-2-oleoyl-sn-glycero-3-phospho-(1'-rac-glycerol) (sodium salt) (16:0-18:1 PG, POPG) was purchased from Avanti Polar Lipids (Alabaster, AL). Cholesterol was purchased from Nu-Chek Prep (Elysian, MN) as a dry powder. Fluorescent dyes 1-palmitoyl-2-(dipyrrometheneboron difluoride)undecanoyl-sn-glycero-3-phosphocholine (TopFluor-PC or TFPC) and 1,2-dioleoyl-sn-glycero-3-phosphoethanolamine-N-(lissamine rhodamine B sulfonyl) (ammonium salt) (Lissamine Rhodamine-PE or LRPE) were purchased from Avanti Polar Lipids (Alabaster, AL) as chloroform solutions. Fluorescent dye 1,2-distearoyl-sn-glycero-3-phosphoethanolamine-N-(7-nitro-2-1,3-benzoxadiazol-4-yl) (ammonium salt) (18:0 NBD PE, NBD-DSPE) was purchased from Avanti Polar Lipids (Alabaster, AL) as a powder. Fluorescent dye 1,1'-Dioctadecyl-3,3,3',3'-

Tetramethylindodicarbocyanine, 4-Chlorobenzenesulfonate Salt) (DiD) was purchased from ThermoFisher Scientific. Naphthopyrene was purchased from Tokyo chemical. HPLC-grade chloroform was used to prepare stock solutions of phospholipids, dyes, and cholesterol. The stocks were stored at -20°C until use. Lipids were weighed precisely assuming two tightly bound water molecules per phospholipid. The concentration of dyes in methanol solution was measured using UV-Vis. Water was purified using a Millipore (Bedford, MA) Milli-Q system. 4-(2-(6-(dioctylamino)-2-naphthalenyl)ethyl)-1-(3-sulphopropyl)-pyridinium inner salt (Di-8-ANEPPS) was purchased from Invitrogen. A 1 mM stock of Di-8-ANEPPS was prepared in ethanol and its concentration was measured using UV-Vis at 498 nm (molar absorption coefficient, ε = 37,000 $M^{-1}cm^{-1}$) in methanol. A 7.2 pH buffer was prepared using 150 mM NaCl solutions (Sigma-Aldrich), 1 mM ethylenediaminetetraacetic acid (EDTA) solution (Thermo Scientific) and 25 mM 4-(2-hydroxyethyl)-1-piperazineethanesulfonic acid (HEPES) (Thermo Scientific). Synthesis of deuterated ether DPPC is given in the end.

### 5.3.2 GUV preparation for fluorescence microscopy

For all experiments, ~250 nmol of total lipids dissolved in chloroform were dispensed into a glass culture tube using a syringe and repeating dispenser (Hamilton USA, Reno, NV) and mixed uniformly using a vortex mixer. The composition of GUVs in three component mixtures were a high-$T_M$ lipid/high-$T_M$ lipid/Chol at a 39/39/22 mol ratio. The fluorescent lipid probes LRPE and NBD-DSPE were added to each sample with probe:lipid ratios of 1:2000 and 1:200, respectively. GUVs were prepared by the electroformation method.[145] The lipid solution was deposited onto the ends of two ITO-coated slides by evaporating the bulk chloroform on a hotplate set to 55°C. For removal of residual chloroform, the slides were placed in a heated desiccator for two hours at 55°C leading to the formation of dry lipid films. A large O-ring was then firmly placed on lipid-coated portion of one slide to make a compartment and two small O-rings were placed on the other end of the slide to act as spacers. The compartment was overfilled with warm sucrose solution (100 mM) and covered with the second ITO slide to create a ‘sandwich’ which was held together by a clip and placed in a metal block at 55°C. Electrical leads were attached to the ITO-covered slides and a peak-to-peak voltage of 1V along with frequency of 7 Hz was applied for two hours at 55°C. The setup was slowly cooled to room temperature overnight. The

GUVs were harvested the next day and were allowed to settle overnight. Then GUVs were diluted in 100 mM glucose solution and imaged with confocal microscopy the next day. For quaternary mixtures, the ratio of the low-$T_M$ lipids DOPC and POPC in the mixture was varied keeping the total mole fraction of low-$T_M$ lipids constant at 0.39. The replacement ratio (ρ) is defined as the mole percentage of DOPC in the low-$T_M$ component of the mixture:

$$\rho = \frac{[\mathrm{DOPC}] * 100}{([\mathrm{DOPC}] + [\mathrm{POPC}])}, \qquad (5.1)$$

where [DOPC] and [POPC] are the mole fractions of DOPC and POPC in the mixture, respectively.

### 5.3.3 LUV preparation for cryo-EM

LUVs were prepared from chloroform solutions of the desired lipid mixtures. Bulk solvent was removed using a nitrogen evaporator and samples were placed in vacuum overnight to remove any remaining solvent. To prepare a multilamellar vesicle suspension, the dry lipid film was hydrated with ultrapure water to a concentration of 3 mg/mL at 50°C, which is above the melting point of the high-$T_M$ lipid. The suspension was vigorously vortexed every 15 min for one hour and then subjected to five freeze/thaw cycles between liquid nitrogen and a 50°C water bath with vigorous vortexing after each thaw step. Finally, the sample was extruded through a 100 nm polycarbonate filter 31 times using a mini extruder (Avanti Polar Lipids).

### 5.3.4 LUV preparation for SANS

LUV preparation for SANS measurements was identical to the preparation described above for cryo-EM with the following differences. To produce appropriate conditions for contrast matching, 65.4% of the high-$T_M$ lipids DPPC and eDPPC were replaced with their chain perdeuterated variants, and lipid films were hydrated with 34.5% $D_2O$ (v/v) to a concentration of 20 mg/mL.

### 5.3.5 LLV preparation for fluorescence spectroscopy

Vesicles of low average lamellarity for fluorescence spectroscopic measurements were prepared using the rapid solvent exchange (RSE) method developed by Buboltz et al.[146]

Briefly, a chloroform solution of the desired lipid mixture (250 nmol total lipid) and fluorescence probes were dispensed in a glass culture tube. For FRET measurements, Nap, TFPC, and DiD were added at probe-to-lipid ratios of 1:200, 1:1500, and 1:1300, respectively. For dipole potential measurements, Di-8-ANEPPS was added at a probe-to-lipid ratio of 1:500. Subsequently, 500 µL of ultra-pure water (for FRET measurements) or HEPES-EDTA-NaCl buffer (pH 7.2) was added to the chloroform mixture of lipids and probes. The sample was subjected to continuous vortexing under vacuum for 90 s to remove chloroform.

### 5.3.6 Confocal fluorescence imaging

Prior to imaging, 50-250 µL of freshly harvested GUVs in 100 mM sucrose were suspended in 2 mL of 100 mM glucose in a culture tube. After ~ 30 min, a 4 µL aliquot was taken from the bottom of the tube and sandwiched between a glass slide and cover slip for microscopy observations. Imaging was performed with a Nikon C2+ point scanning system attached to a Nikon Eclipse Ti2-E microscope (Nikon Instruments, Melville, NY) equipped with a Plan Apo Lambda 60×/1.4 NA oil immersion objective. Sample temperature was maintained with an objective cooling collar (Bioptechs, Butler, PA) and micro-stage PID controller (VA Heat). NBD-DSPE and LRPE were excited with 488 nm and 561 nm laser lines, respectively, with quarter wave plates (ThorLabs, Newton, NJ) inserted in the excitation path to correct for polarization artifacts. 3D z-stacks were collected using both the red (561 nm laser, 546 nm quarter waveplate, laser power 3, HV setting 75) and green (488 nm laser, 488 nm quarter waveplate, laser power 5, HV setting 90) channels simultaneously with a step size of 1 µm.

### 5.3.7 Cryo-EM imaging and analysis

LUV samples were cryopreserved by applying a 4 µL aliquot to a Quantifoil 2/2 carbon-coated 200 mesh copper grid (Electron Microscopy Sciences, Hatfield, PA) that was glow-discharged for 30 s at 20 mA in a Pelco Easi-Glow discharge device (Ted Pella, Inc., Redding, CA). After manual blotting at room temperature (~ 22°C), the grids were plunged into liquid ethane cooled with liquid $N_2$. Cryo-preserved grids were stored in liquid $N_2$ until use. Cryo-EM image collection was performed at ~ 2 µm under focus on a FEI Polara G2 operated at 300 keV equipped with a Gatan K2 Summit direct electron detector operated

in counting mode. Data collection was conducted in a semi-automated fashion using Serial EM software operated in low-dose mode. Briefly, areas of interest were identified visually and 8×8 montages were collected at low magnification (2400×) at various positions across the grid and then individual areas were marked for automated data collection. Data was collected at 2.7 Å/pixel. Movies of 30 dose-fractionated frames were collected at each target site with the total electron dose being kept to < 20 $e^{-}/Å^2$. Dose-fractionated movies were drift-corrected with MotionCor2.

Cryo-EM thickness and intensity profiles were generated as described previously.[67] Briefly, vesicles were identified and subdivided into 5 nm segments to obtain spatially resolved intensity profiles in the direction normal to the bilayer using the neural network-based algorithm MEMNET which is part of the TARDIS software package.[127] The ML analyses used in the following sections were implemented in Wolfram Mathematica 13.2 (Wolfram Research, Champaign, IL) unless stated otherwise. We used unsupervised *k*-means clustering as implemented in Mathematica v13.2, with the number of clusters (*k*) set to 2. The clustering analysis was performed on segment intensity profiles (201-dimensional vector of intensities). Domain sizes were determined from the length of runs of Ld and Lo segments in each vesicle.

### 5.3.8 Di-8 measurements

The electrochromic fluorescent probe Di-8-ANEPPS was used to measure membrane dipole potential of Lo and Ld phases as previously described.[147, 148] The Ld composition was DPPC/DOPC/Chol = 23/67/10 and the Lo composition was DPPC/DOPC/Chol = 56/9/35. These compositions form the endpoints of a tieline that passes through the composition DPPC/DOPC/Chol = 40/40/20 as determined by small-angle X-ray scattering (F. Heberle personal communication). Since there are no phase diagrams available for ternary mixtures that contain ether lipids, the same compositions were used for mixtures containing one or more ether lipids. Moreover, for studying the relative impact of ether lipids on phase separation the compositions were kept same. Vesicle preparation was described in Section 5.3.4. 100 µL of the vesicle suspension was further diluted in 1900 µL of buffer in a fluorescence cuvette. The slit width for both excitation and emission windows were set to 3.5 nm and integration time was 0.1 s. Single point excitation

wavelengths were set at 420 and 520 nm with an emission wavelength of 670 nm which were collected simultaneously. A data point was collected every 30 s for a total of 15 min. The fluorescence intensity ratio *R*, defined as the ratio of fluorescence intensity at an excitation wavelength of 420 nm to 520 nm, was previously shown to be proportional to the membrane dipole potential.[148]

### 5.3.9 FRET measurements

LLVs were prepared as described above. A volume of 100 µl of this suspension was diluted with 1900 µl of ultra-pure water in a fluorescence cuvette. Slit widths for experiments were 3 nm bandpass for both excitation and emission with integration time of 0.1 s. Single point fluorescence measurements were recorded over a temperature range of 50/60°C to 20°C. At 0.5°C intervals, all three direct signals for each of the dyes, as well as two FRET signals (Nap → DiD and TFPC → DiD), were collected.

### 5.3.10 FRET analysis

The ability to detect phase separation with FRET relies on changes in FRET efficiency as the fluorescent donor and acceptor molecules either segregate or co-localize in response to lipid demixing.[50] We used two FRET pairs to take advantage of the fact that different dyes have different partitioning behavior in the distinct membrane environments of Lo and Ld phases. For example, TFPC and DiD favorably partition into the Ld phase, resulting in an increase in FRET intensity upon phase separation since both the FRET donor and acceptor are in the same phase. On the other hand, Nap favorably partitions into the Lo phase, leading to a decrease in its FRET to DiD after phase separation since the donor and acceptor are in different phases. To utilize FRET results in a quantitative manner, experimental measurements need to be normalized for various factors that can affect the fluorescence intensities. One such factor is the potential variability in vesicle concentration of lipids and dyes between samples, which can result in variation in measured fluorescence intensities. This effect can be corrected by normalizing each sample's sensitized acceptor emission ($F_A^{Dex}$) using the geometric mean of the direct fluorescence signals of the acceptor ($F_A^{Aex}$) and donor ($F_D^{Dex}$) dyes:

$$FRET = \frac{F_A^{D_{ex}}}{\sqrt{F_D^{D_{ex}} \cdot F_A^{A_{ex}}}}. \qquad (5.2)$$

In a uniformly mixed bilayer (e.g., DOPC in Fig. 5.3a) the normalized FRET typically shows a gradual, monotonic variation with temperature. However, if a phase transition occurs somewhere in the temperature range, a change in slope will be seen due to probe partitioning. If the donor and acceptor prefer different phases, FRET will decrease; if donor and acceptor prefer the same phase, FRET will increase (Fig. 5.3b). The onset of these changes are often subtle, but can be enhanced by taking the ratio of the FRET signals given by Eq. 5.3:

$$FRET\ ratio = \frac{FRET_{TFPC \rightarrow DiD}}{FRET_{Nap \rightarrow DiD}}. \qquad (5.3)$$

To determine the miscibility transition temperature, $T_{misc}$, we modeled the $FRET$ vs. $T$ data with an empirical function of five adjustable parameters that describes two regimes of different behavior:

$$FRET(T; T_{misc}) = \begin{cases} a\left(T^2 - {T_{misc}}^2\right) + b(T - T_{misc}) + FRET_{misc} & T < T_{misc} \\ c(T - T_{misc}) + FRET_{misc} & T \geq T_{misc} \end{cases}. \qquad (5.4)$$

In Eq. 5.4, the parameters $a$ and $b$ control the shape of the curve in the regime of phase separation (i.e., $T < T_{misc}$), the parameter $c$ describes the slope in the uniform regime (i.e., $T \geq T_{misc}$), and the parameter $FRET_{misc}$ is the FRET value at the point where these regimes intersect (i.e., $T = T_{misc}$).

### 5.3.11 SANS analysis

The neutron contrast between is defined as the difference in their neutron scattering length density (NSLD). By matching the NSLD of the aqueous solvent to that of the average bilayer composition, we significantly diminish the transverse bilayer scattering that would otherwise overshadow the contrast arising from lateral segregation of lipids (i.e., phase separation). Contrast matching is done by adjusting the $D_2O/H_2O$ ratio in the aqueous medium and the ratio of deuterated to protiated chains in the bilayer. In this study a 34.6% $D_2O$ medium and 65.4% chain-perdeuterated ether/ester DPPC was used.

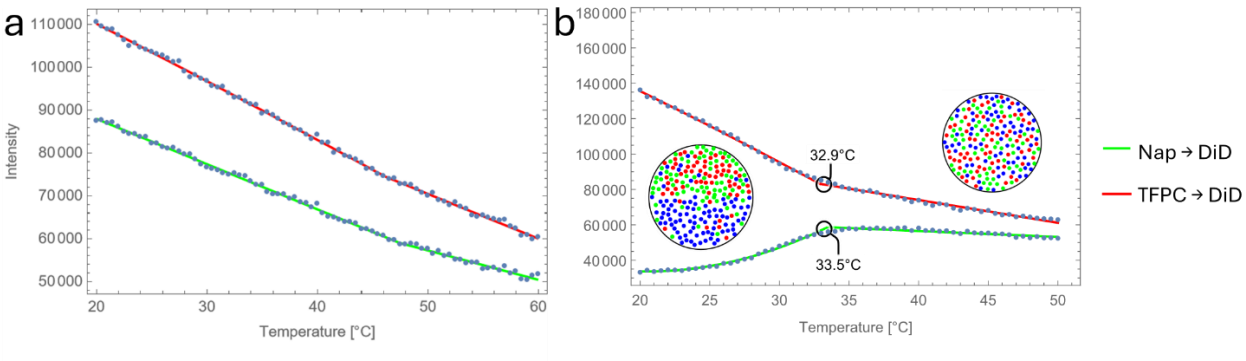


**Figure 5.3 FRET analysis.** a) Uniform one component DOPC b) Phase separated DPPC/DOPC/Chol (39/39/22 mol ratio). At higher temperature, all probes are uniformly mixed, but below the miscibility transition temperature a phase separation takes place. Nap (donor, blue) partitions into Lo phase while DiD (acceptor, red) mostly partitions into Ld which leads to a decrease in their FRET signal for pair when temperature is lowered. In the other probe-pair TFPC (donor, green) and DiD (acceptor, red) both partitions preferably in Ld phase which leads to a increase in their FRET signal for pair when temperature is lowered.

Under these conditions, minimal scattering occurs in the nearly contrast-free system when all lipids are well-mixed. However, when domains form, the lateral segregation of saturated and unsaturated lipids creates contrast in the acyl chain region, leading to an increase in the scattering signal. To analyze SANS data we calculated the Porod scattering invariant, $Q$, as follows:

$$Q = \int_0^\infty q^2 I(q) dq. \qquad (5.5)$$

$Q$ is proportional to the mean-square average fluctuations in NSLD within the sample. In a lipid vesicle, $Q$ has contributions from contrast variation normal to the bilayer (i.e., headgroups vs. chains) as well as in-plane contrast variation, for example the phase separation of protiated and deuterated lipids. The contrast conditions we used were chosen to maximize lateral contrast, thereby allowing $Q$ to be approximated as:

$$Q \approx a_{L_o}\left(1 - a_{L_o}\right)\Delta\rho^2. \qquad (5.6)$$

In Eq. 5.6, $a_{L_o}$ represents the fraction of Lo phase in the vesicle and $\Delta\rho$ is the neutron contrast between Lo and Ld phases[149]. Eq. 5.6 shows that SANS is sensitive to domain formation. If a phase transition occurs within a temperature range of interest, a plot of $Q$ vs. $T$ will show a change in slope at $T_{misc}$.[150] We modeled the data with a function of two linear regimes that intersect at $T_{misc}$,

$$Q(T; T_{misc}) = \begin{cases} m_2(T - T_{misc}) + Q_{misc} & T < T_{misc} \\ m_1(T - T_{misc}) + Q_{misc} & T \geq T_{misc} \end{cases}. \qquad (5.7)$$

The four adjustable parameters were the slopes of the linear regimes, $m_1$ and $m_2$, and their intersection point $(T_{misc}, Q_{misc})$.

### 5.3.12 Indirect dipole potential measurements

The membrane dipole potential ($\psi_d$) is an electrical potential difference between the hydrocarbon core of a lipid membrane and its polar exterior. It originates from the nonrandom arrangement of polar lipid residues and water molecules near the membrane surface. The carbonyl groups of the ester backbone linkages are attributed as a major contributor to $\psi_d$ since much lower $\psi_d$ magnitudes have been reported in lipids with ether

backbone linkages.[151] Loew et al. showed that voltage sensitive dyes such as Di-8-ANEPPS can be used to indirectly measure $\psi_d$ in a bilayer structure.[152] A spectral shift in voltage sensitive dyes occurs as a response associated with a change in the local electric field intensity. Changes in lipid packing or area per lipid would change the dipole density, arrangement of water molecules at the interface, and penetration of water molecules into the membrane. All these changes in turn would change the effective dielectric constant at the membrane interface. Various studies have shown *R* values to be directly proportional to $\psi_d$.[153] *R* values were calculated for both Lo and Ld phases separately for each of the four systems under study.

### 5.4. Results and Discussion

Lo phases are enriched in cholesterol and saturated (high-$T_M$) lipids whereas Ld phases are rich in unsaturated (low-$T_M$) lipids. Here, we study four systems with composition high-$T_M$/low-$T_M$/Chol = 39/39/22: eDPPC/DOPC/Chol (I); eDPPC/eDOPC/Chol (II); DPPC/DOPC/Chol (III); and DPPC/eDOPC/Chol (IV). We can control the amount of ether and ester lipid going into each phase using combinations of ether-linked and ester-linked high-$T_M$ and low-$T_M$ lipids. This allows us to alter the difference in the membrane dipole potential between the two phases. Line tension can be controlled by using the hybrid lipids POPC.[57] Together, the ability to control both the dipole density difference of Ld and Lo phases, and their line tension, allows us to interrogate the competing interactions model proposed by Feigenson and coworkers.[141, 144]

#### 5.4.1 Indirect estimation and comparison of membrane dipole potential

The results were in agreement with the literature showing ester lipids with higher *R* values as compared to ether lipids. Also, Lo mixtures had higher *R* values as compared to Ld mixtures mainly due to presence of higher cholesterol and saturated lipid content.[148] According to the hypothesis from the simple interactions model, the dipole potentials of Lo and Ld create a state of frustration that could potentially lead to the breakup of macroscopic domains.[141] Now, the value $\Delta R = R_{Lo} - R_{Ld}$ can be used as an indirect measure for $\psi_{Lo}$ - $\psi_{Ld}$. Higher values of $\Delta R$ result in more frustration in the system (referred to as dipole repulsions in the literature) since one of the phases has a much higher $\psi_d$.. If the value of $\Delta R$ is large enough it leads to the breakup of domains to spread

out the higher $\psi_d$ in Lo phase throughout the vesicle rather than concentrating it in one big domain. In doing so, dipole repulsion acts against line tension by increasing the perimeter of domains (single large domains has minimum perimeter).

The Lo phase in system III exhibited the maximum *R* value since all lipids are ester-linked. Conversely, the Lo phase in system II displayed the minimum *R* value because all lipids are ether-linked. A similar pattern was observed in the Ld phase as well. The parameter we are interested in for this study is the difference in the *R* values of Lo and Ld phases, i.e., $\Delta R$. The $\Delta R$ values across all systems followed the rank order: IV ($\Delta R$ = 3.1) < III ($\Delta R$ = 2.64) < II ($\Delta R$ = 0.65) < I ($\Delta R$ = 0.38) (Fig 5.4). The $\Delta R$ values can be explained based on the composition of the Lo and Ld phases. For example, in system IV (which has the largest $\Delta R$), the Lo phase is mostly composed of saturated lipid DPPC with ester linkages and cholesterol. On the other hand, the Ld phase is predominantly composed of ether-unsaturated lipid eDOPC. The second system in the hierarchy is III, where both Lo phase and Ld phases are composed of ester lipids. Next in line is system II, in which both the Lo and Ld phases consist of pure ether lipids. The last system in the order is I, where the Lo phase predominantly contains ether-saturated lipid eDPPC, while the Ld phase contains ester lipid DOPC. Despite the presence of ether lipids as the major constituent in the Lo phase, it still exhibits a higher *R* value due to the presence of saturated lipids and cholesterol. Now, the *R* value in the Ld phase is much closer to that of the Lo phase because of the presence of majority lipid ester DOPC.

### 5.4.2 GUVs and POPC titration experiments

GUVs were prepared for all four compositions. All four systems were found to be phase separated and showed micron-sized domains (Fig 5.5). An interesting observation was made with system IV, where a fraction of the vesicles was found to have multiple small domains whereas the remaining three systems showed a single large domain at room temperature. According to our hypothesis, the high $\Delta R$ value in system IV is responsible for breakup of domains. The repulsion was high enough to counter line tension in this case. The relative line tension in all four systems was compared by replacing DOPC by POPC as shown in the previous experiments.[57, 140]

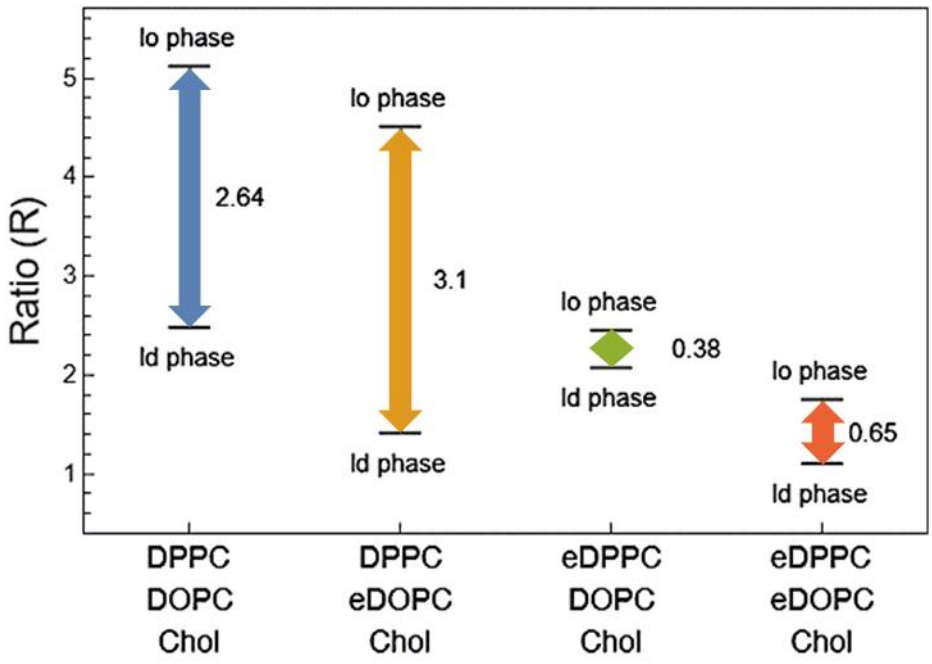


**Figure 5.4 $\Delta R$ measured with Di-8-ANEPPS.** Modulation of $\Delta R$ when different combinations of ether and ester lipid are used.

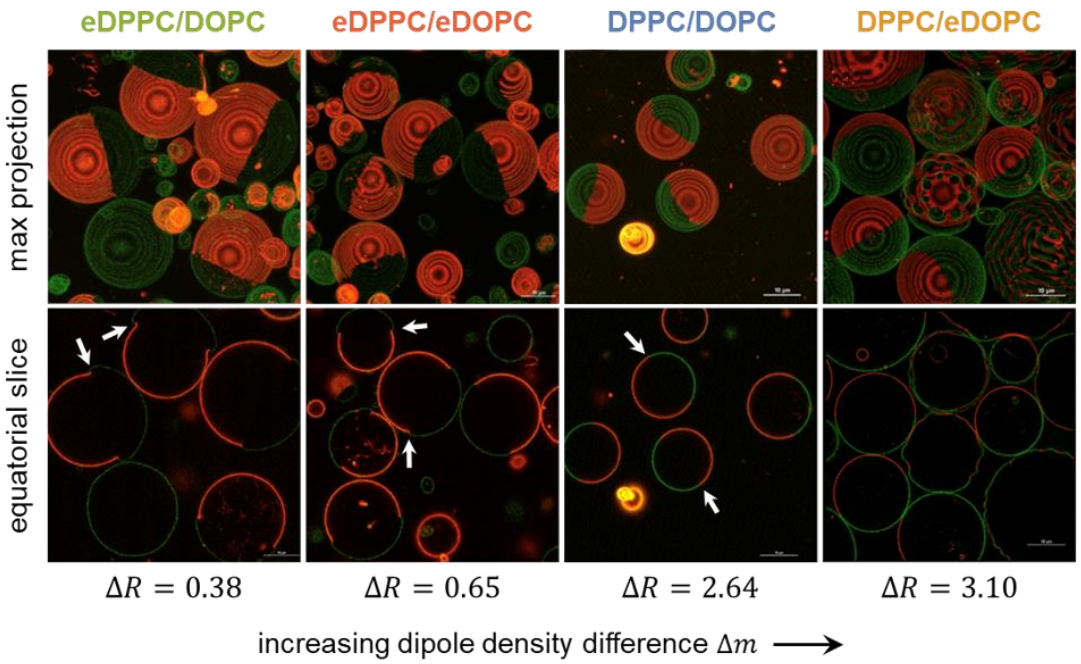


**Figure 5.5 Representative GUVs for all four systems (39/39/22).** Phase separation was observed in all four systems at room temperature. System IV with the highest $\Delta R$ showed smaller domains as compared to the other systems. Also in systems I and II where line tension dominates, some budding vesicles of pure Lo and Ld were seen at room temperature. The red dye (LR-PE) predominantly partitions into the Ld phase, while the green dye, NBD-DSPE, shows a slight preference for the Lo phase over the Ld phase.

POPC is known to lower the line tension of the system, therefore a system where opposing forces to line tension are weak would require a higher amount of DOPC replaced with POPC. In the systems with eDOPC, we used ePOPC for replacement. Addition of POPC breaks the domains into smaller domains and the process is continued until a modulated domain pattern is formed. Further addition of POPC beyond that point breaks the domains into nanodomains that no longer can be resolved by CFM. ρ (percentage of low melting lipid that is DOPC) values were estimated for each of the systems to the point $\rho_{end}$ where micron sized domains were broken into nanosized domains (Fig 5.6). $\rho_{end}$ values showed the same trend as $\Delta R$ values. The system IV has the highest $\rho_{end}$ which means the minimum amount of POPC was required for breaking up the domains, whereas system I has the lowest $\rho_{end}$ which shows the forces competing against line tension were weak and therefore a high amount of POPC was required to break up the domains.

### 5.4.3 Miscibility transition temperature

The miscibility transition temperature, $T_{misc}$, was estimated for all four systems using three different methods: (1) FRET was used on vesicles prepared from RSE; (2) CFM was used on GUVs prepared by Electroformation; (3) SANS was used on extruded LUVs prepared from the dry film method. The three sample preparation methods produce vesicles with inherently different sizes and number of lamellae. Each measurement technique also has a unique resolution limit for detecting domains, with FRET and SANS having a resolution of 5-10 nm while CFM has a resolution limit of ~ 200 nm. SANS samples were prepared using deuterated high melting lipids which have a few degrees lower melting point as compared to the corresponding protiated lipids. FRET is dependent on the partition of different dyes in the Lo and Ld phases. GUVs prepared from electroformation have inherent compositional variation of a few percent. Given the limitations and upside of each of the probing methods and sample preparation, all three methods report the same rank order of $T_{misc}$. For FRET the order was IV (31.1°C) < III (33°C) < II (40.2°C) > I (44.8°C). In GUVs IV (29.1°C) < III (31.4°C) < II (38.2°C) < I (41.4°C). From SANS, IV (27.7°C) < III (31.2°C) < II (34.1°C) < I (38.9°C) (Fig 5.7, 5.8, 5.9).

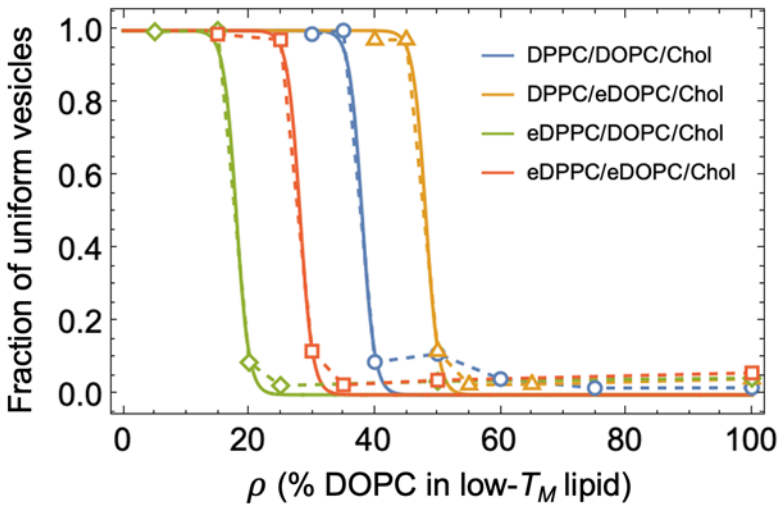


**Figure 5.6 Estimation of $\rho_{end}$.** System I has the lowest $\rho_{end}$ followed by II, III and IV which is the same trend as $\Delta R$ values.

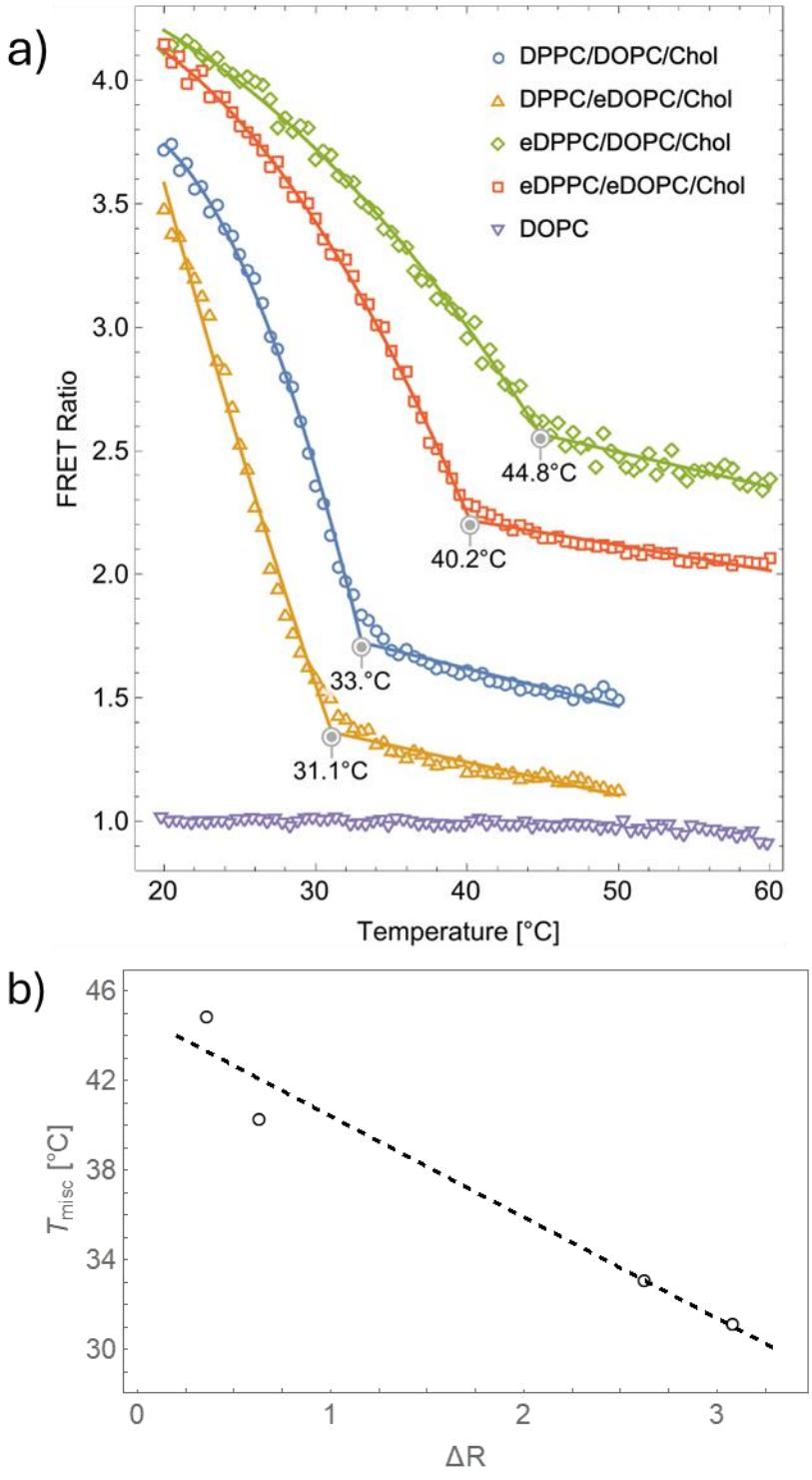


**Figure 5.7 $T_{misc}$ from FRET experiments.** a) $T_{misc}$ was evaluated from the inflection point in each phase separated system. $T_{misc}$ followed the trend IV < III < II < I. A uniform DOPC sample (purple triangles) shows no transition. b) $T_{misc}$ was found to be negatively correlated with $\Delta R$ values.

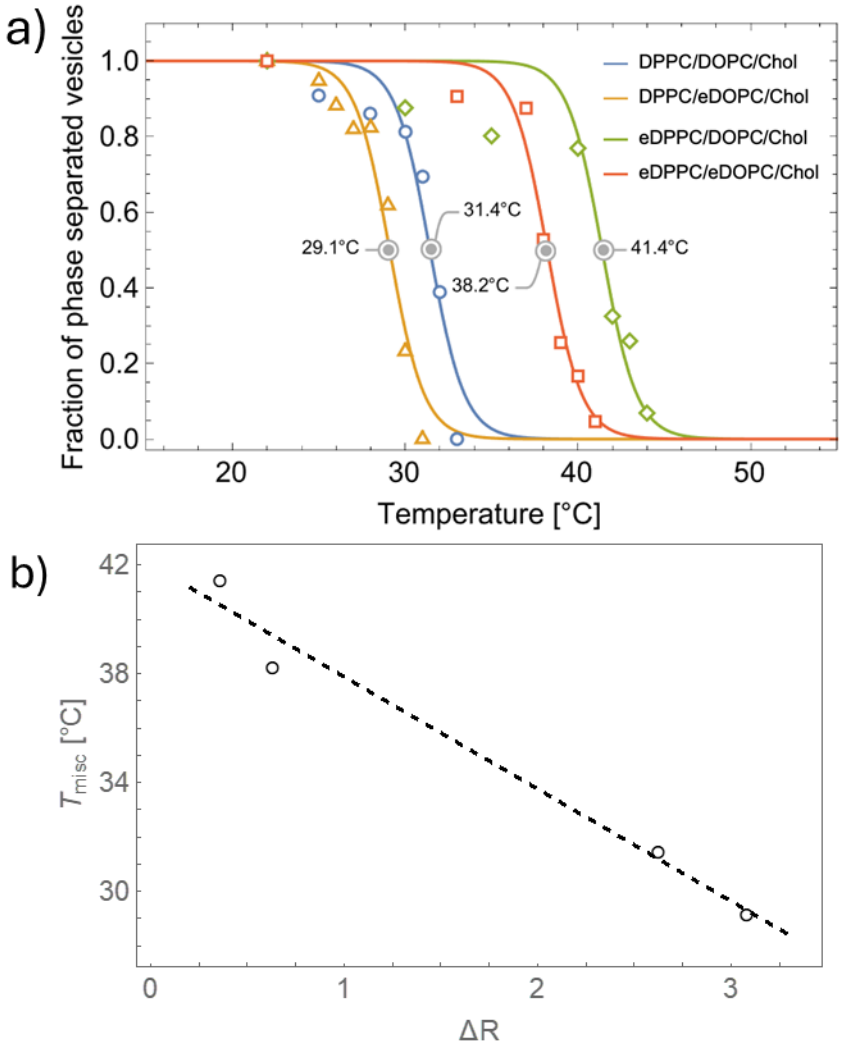


**Figure 5.8 $T_{misc}$ from GUV experiments.** a) $T_{misc}$ was evaluated from direct imaging using CFM for each phase separated system. $T_{misc}$ followed the same trend IV < III < II < I as FRET studies. b) Again, $T_{misc}$ was found to be negatively correlated with $\Delta R$ values.

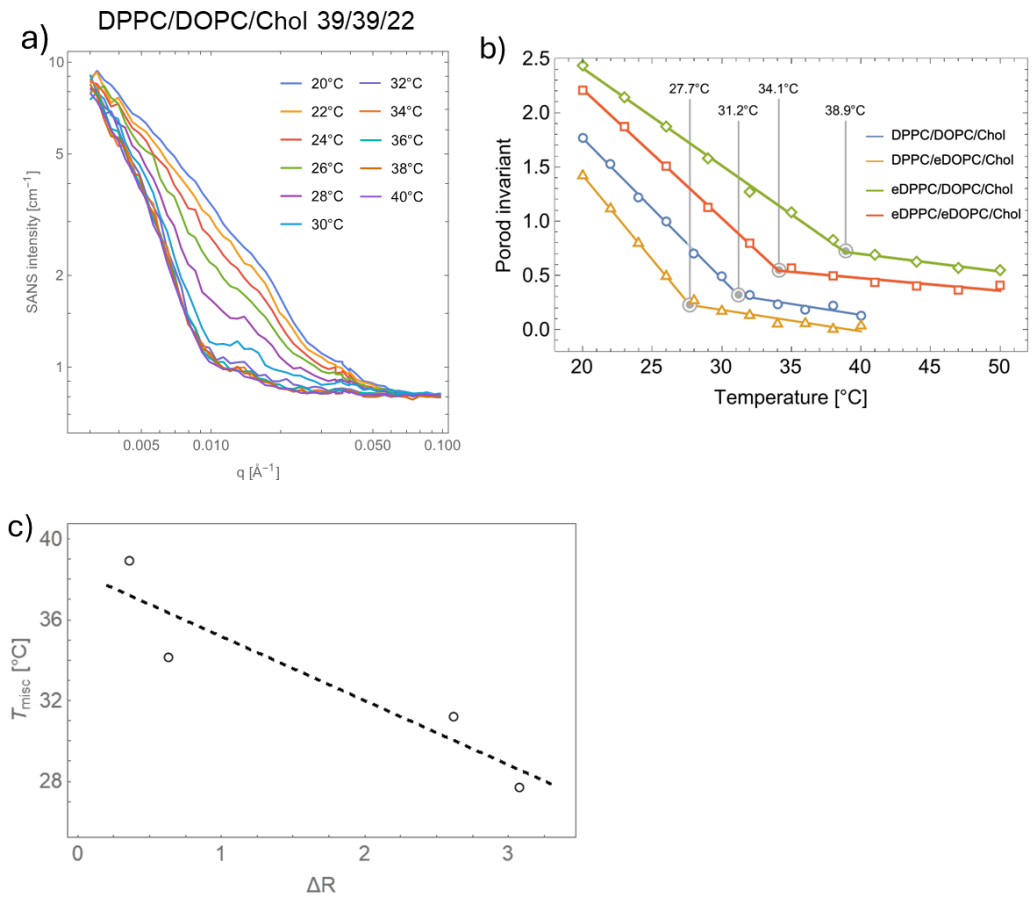


**Figure 5.9 $T_{misc}$ from SANS experiments.** a) SANS intensity vs. q plotted for various temperatures for DPPC/DOPC/chol (39/39/22). The Porod invariant was evaluated at each temperature. b) $T_{misc}$ was evaluated from the Porod invariant for each phase separated system. $T_{misc}$ followed the same trend IV < III < II < I as FRET and GUV studies. c) $T_{misc}$ was found to be negatively correlated with $\Delta R$ values.

The order of $T_{misc}$ concurred with the observations from Di-8 experiments, i.e., $T_{misc}$ was found to be negatively correlated with $\Delta R$ values. System IV, where the $\Delta R$ value was maximum, had the lowest transition temperature as hypothesized. In system IV the highest membrane dipole potential difference between the two phases is expected to contribute towards the lowest $T_{misc}$ and vice versa in system in system I where the $T_{misc}$ is the highest. This observation supports our hypothesis that variations in the membrane dipole potential of two coexisting liquid phases can have a significant impact on the physical properties of phase separated systems.

### 5.4.4 Bilayer thickness distribution and measuring domain size using cryo-EM

The difference in bilayer thickness and contrast in intensity profiles of Lo and Ld phases can help detect phase separation in LUVs.[67] Approximately 900 vesicles with diameters greater than 40 nm were analyzed per sample. Phase separation was observed in each system to some extent (Fig 5.10). Systems III and IV exhibited clear phase separation, while systems I and II showed less distinct separation due to budding, indicative of high line tension (also observed in Chapter 4). The thickness probability distribution for all four systems was non-Gaussian, suggesting the presence of two different Gaussian distributions and suggesting phase separation (Fig 5.11). A trend was observed in these distributions: systems with higher $\Delta R$ exhibited two well-separated Gaussian distributions, with the gap between them progressively closing from system IV to system I. This is suspected to result from smaller liquid-ordered (Lo) phase domains budding off from the parent vesicle, leaving behind larger liquid-disordered (Ld) vesicles. Systems I and II, which have high line tension, are particularly prone to this budding phenomenon. Similar results were also observed in giant unilamellar vesicles (GUVs) of systems I and II (Fig. 5.5). Domain size was also measured for each system using 2-means clustering analysis.[137, 139] The domains in system IV were found to much smaller than system III and the result aligned with the GUV study (Fig 5.11). The domain size in these two systems showed a linear increase in domain size with vesicle size. The size of Lo domains in system I and II do not follow the same trend. The Lo domain size starts to decrease with an increase in vesicle size. We again suspect that this outcome is related to budding in these systems.

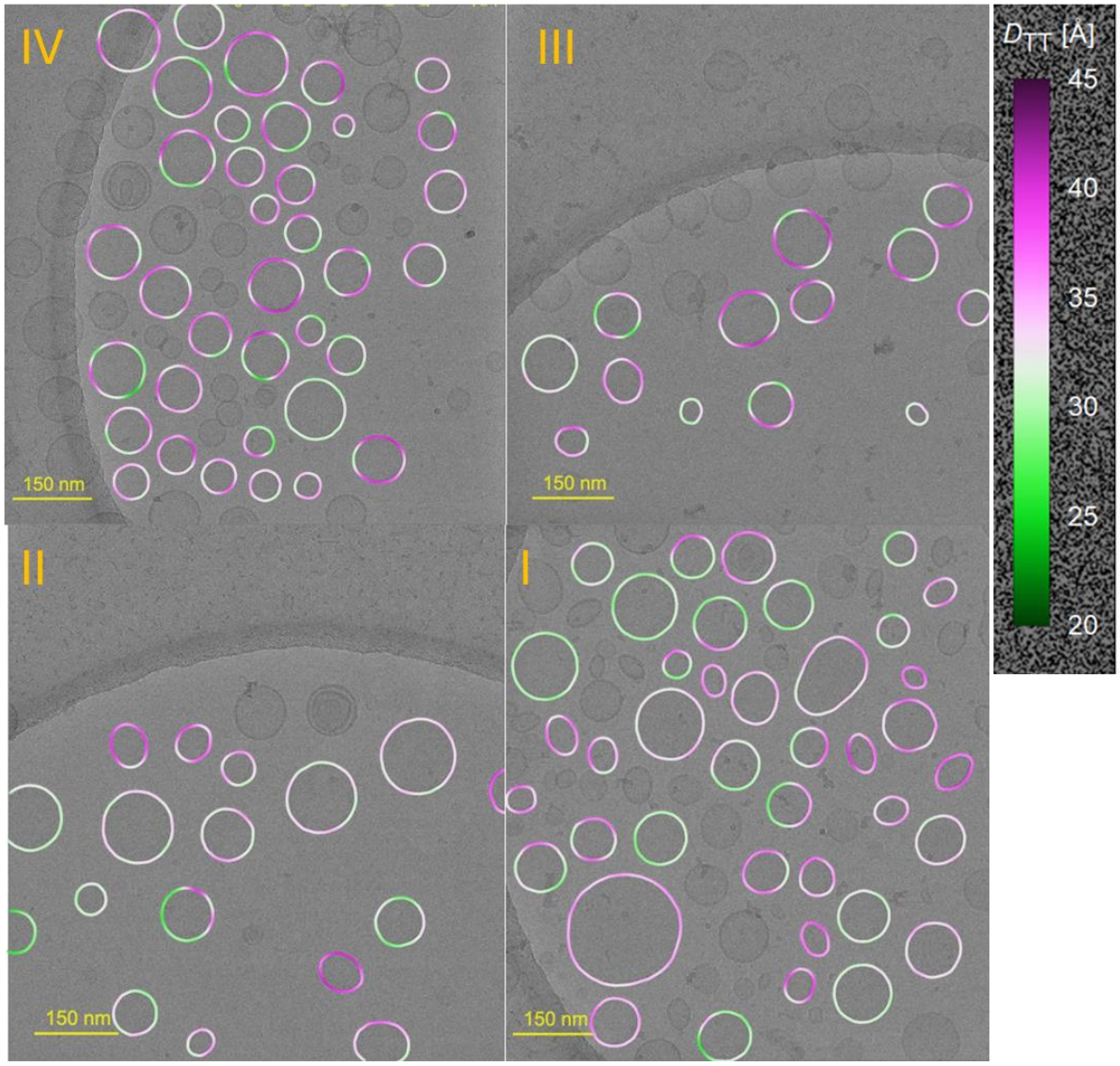


**Figure 5.10 Cryo-EM reveals phase separation through thickness analysis.** The domains were smallest in system IV, followed by system III. Phase separation was not clearly observed in all vesicles in systems II and I, where significant budding was noted. This budding resulted in smaller vesicles, either pure pink or green, which are suggested to bud from each other due to high line tension.

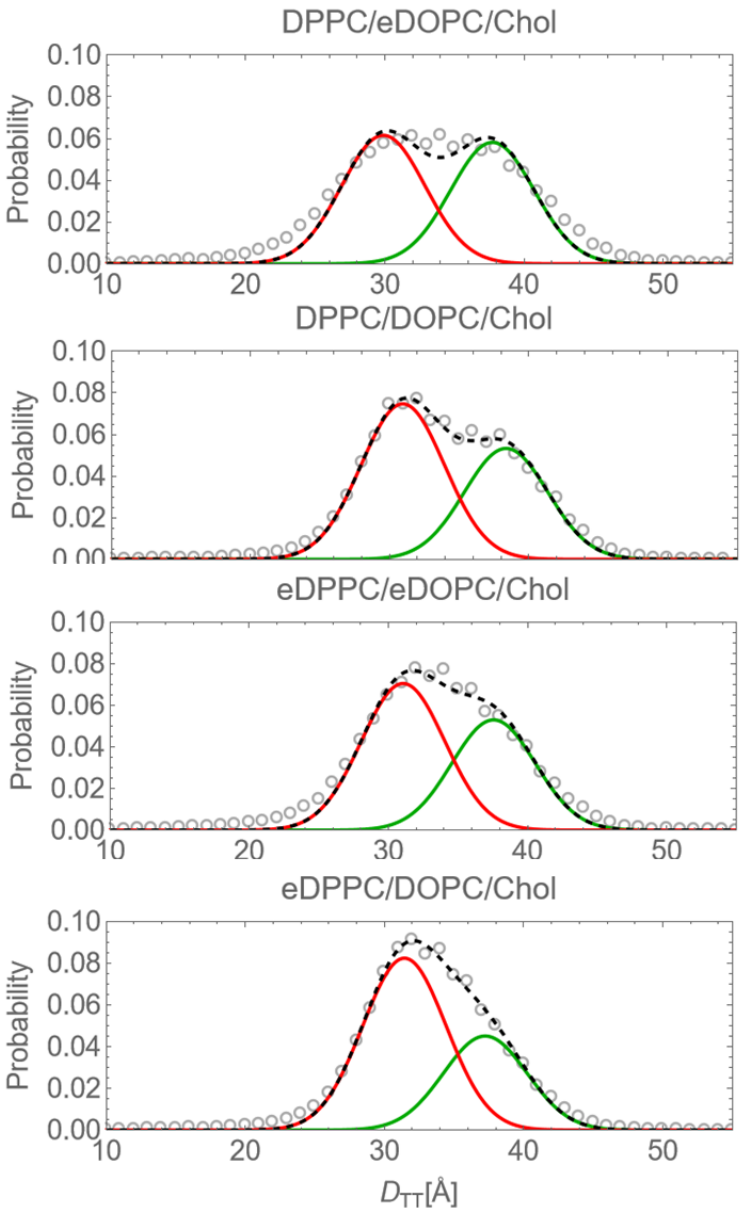


**Figure 5.11 Bilayer thickness distribution.** The broad non-Gaussian distribution indicates the presence of phase separation in each of the systems.

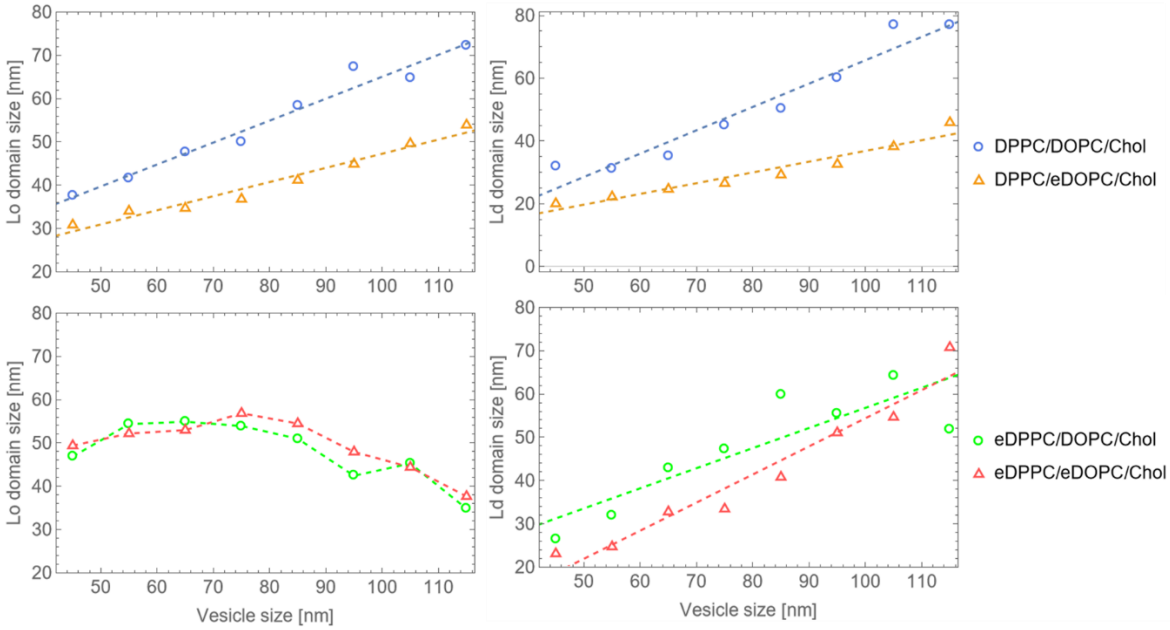


**Figure 5.12 Domain size vs. vesicle size.** System IV (orange) and system III (blue) show a linear increase in domain size with vesicle size (both Lo and Ld). The domains in system IV are smaller than the system as seen in GUV studies. The results for system I (green) and II (red) do not align with the trends due to the presence of budding in the system.

## 5.5 Summary and Conclusions

In this study, we investigate how varying lipid compositions affect membrane properties and phase separation in model membrane systems. We focused on testing the competing interactions model of Feigenson and coworkers, which proposes that line tension drives the system towards fewer large domains where a difference in membrane dipole potential drives the system towards smaller multiple domains. Systems I to IV, with different ratios of ether and ester lipids, show distinct membrane dipole potentials influencing domain properties. $T_{misc}$ was estimated using three different techniques (FRET, CFM, and SANS). Despite differences in basic principles of all the methods, they still consistently ranked the systems in the same order of $T_{misc}$ values: IV < III < II < I. Higher ΔR correlates with lower $T_{misc}$, indicative of the difference in dipole potential working against the line tension to help in breaking the domains. Line tension, influenced by the lipid composition, was analyzed using POPC titration, showing that system IV (which has the highest ΔR value) required the least POPC to break domains. Cryo-EM domain size measurements also supported that higher ΔR values led to smaller domains and budding being a suspected problem in systems with high line tension.

This study gives us insight into how changing lipid composition can change properties of lipid domains, which could be one of the ways biological membranes control lipid raft formation. This study provides valuable insights into how variations in lipid composition can profoundly influence the properties of lipid domains within membranes. These findings are particularly relevant in understanding how biological membranes may regulate the formation of lipid rafts. By manipulating lipid compositions, such as altering the balance between ether and ester lipids or adjusting cholesterol content, membranes can modulate parameters like membrane dipole potential and miscibility transition temperatures. These factors, in turn, impact the size, stability, and characteristics of lipid domains, including lipid rafts. Thus, the study underscores the importance of lipid composition in biological membranes as a mechanism for controlling lipid raft formation and function.

### 5.6 Synthesis of deuterated ether lipid

The synthetic route for deuterated ether-linked DPPC lipid **dPC-4** is outlined in Scheme 1 (Figure 5.13) PMB protected diol **CL-2** was first prepared from (*S*)-isopropylideneglycerol, followed by acetal deprotection. Next, Williamson ether synthesis was performed to introduce deuterated lipid alkyl chains using 1-boromohexadecane-$d_{33}$. Dietherglycerol lipid **dPC-2** was obtained via PMB deprotection in the presence of DDQ. This lipid was then treated with ethylene glycol chlorophosphite followed by ring opening with trimethylamine to introduce the phosphocholine headgroups of the desired product. A non-deuterated version was prepared in the same manner using the non-deuterated 1-boromohexadecane.

**(*R*)-3-((4-Methoxybenzyl)oxy)propane-1,2-diol (CL-2)** was synthesized according to a previously published protocol.[154]

**(*S*)-1-((2,3-Bis((hexadecyl-$d_{33}$)oxy)propoxy)methyl)-4-methoxybenzene (dPC-1)** Compound **CL-2** (0.1 g, 0.473 mmol) was dissolved with 3 mL dry DMF in a 50 mL RBF under Argon at 0 °C. Sodium hydride (NaH, 0.114 g, 2.84 mmol, 60% dispersion in mineral oil) was added carefully. The reaction mixture was stirred for 30 min before addition of tetrabutylammonium iodide (TBAI, 10 mg, 10% w/w of diol) and 1-bromohexadecane-$d_{33}$ (0.4 g, 1.18 mmol). Next, the reaction was allowed to warm up to room temperature and further stirred overnight before being quenched by addition of water. EtOAc (3×25 mL) was used to extract the aqueous residual. The combined organic layer was washed with 5×50 mL water and 50 mL brine. After being dried over $Na_2SO_4$, filtered, and concentrated under reduced pressure, the crude was purified with silica gel column chromatography using gradient elution from hexane to 10% EtOAc in hexanes as a white solid (0.282 g, 0.388 mmol, 82% yield). $R_f$ = 0.46 (10% EtOAc-hexanes).

$^1$H NMR (500 MHz, Chloroform-*d*) δ 7.26 (d, *J* = 8.6 Hz, 2H), 6.87 (d, *J* = 8.6 Hz, 2H), 4.49 (s, 2H), 3.80 (s, 3H), 3.61 – 3.44 (m, 5H). $^2$H NMR (77 MHz, Chloroform-regular) δ 3.47 (d, *J* = 10.2 Hz, 4H), 1.20 (m, 56H), 0.83 (s, 6H).

$^{13}$C NMR (126 MHz, Chloroform-*d*) δ 159.26, 130.69, 129.33, 113.84, 78.01, 73.14, 70.91, 70.14, 55.36.

**A.**

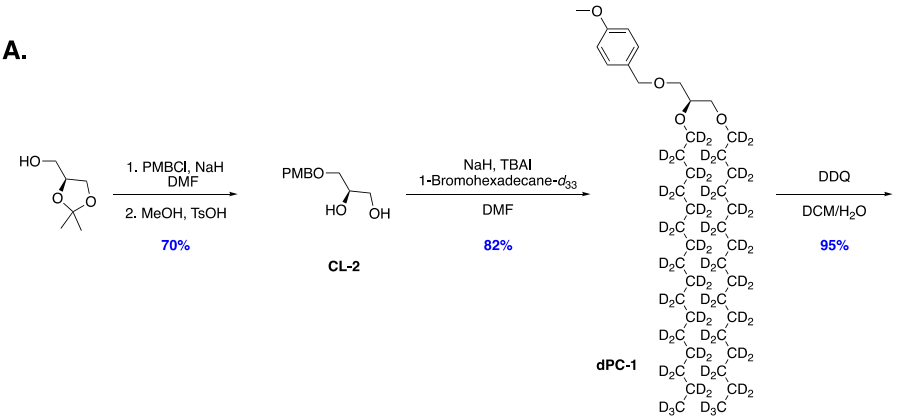
1. PMBCl, NaH
DMF
2. MeOH, TsOH
70%
CL-2
NaH, TBAI
1-Bromohexadecane-$d_{33}$
DMF
82%
DDQ
DCM/$H_2O$
95%
dPC-1

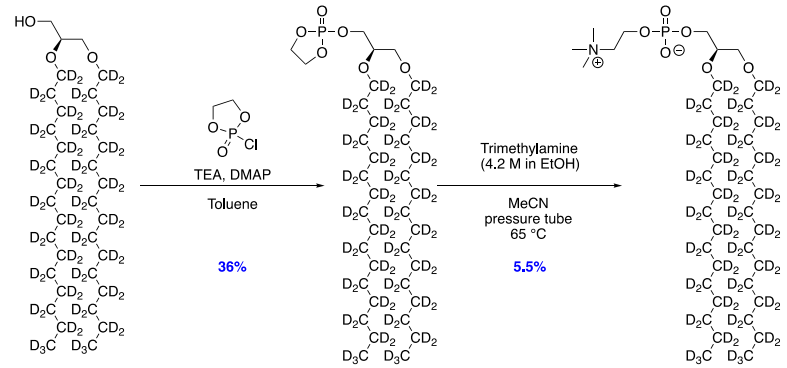
TEA, DMAP
Toluene
36%
Trimethylamine
(4.2 M in EtOH)
MeCN
pressure tube
65 °C
5.5%
dPC-2
dPC-3
dPC-4

**B.**

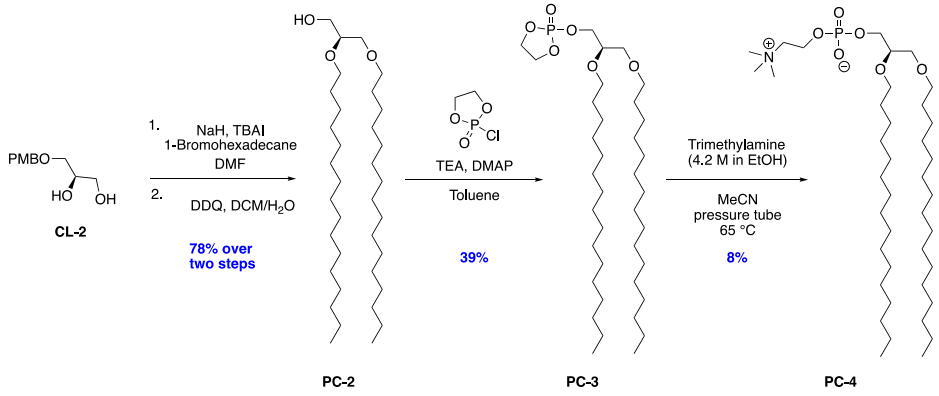
CL-2
1. NaH, TBAI
1-Bromohexadecane
DMF
2. DDQ, DCM/$H_2O$
78% over
two steps
TEA, DMAP
Toluene
39%
Trimethylamine
(4.2 M in EtOH)
MeCN
pressure tube
65 °C
8%
PC-2
PC-3
PC-4

**Figure 5.13 Scheme 1.** Synthetic route for deuterated ether-linked DPPC lipid (**A**) and non-deuterated version (**B**). PMB-protected glycerol diol **CL-2**, derived from (*S*)-isopropylideneglycerol, underwent Williamson ether synthesis to form **dPC-1**. Subsequent PMB deprotection, ethylene glycol chlorophosphite treatment, and TMA treatment led to the final deuterated ether-linked DPPC lipid **dPC-4** (A). The non-deuterated version (**B**) followed the same steps using a non-deuterated starting material.

**(*S*)-2,3-Bis((hexadecyl-$d_{33}$)oxy)propan-1-ol (dPC-2)**

Compound **dPC-2** (0.258 g, 0.355 mmol) and 2,3-dichloro-5,6-dicyano-1,4-benzoquinone (DDQ, 0.161 g, 0.71 mmol) were weighed into a 100 mL flask. DCM/water (20 mL/2 mL, 10/1, v/v) was then added, and the reaction was stirred vigorously at room temperature overnight. The color of the reaction turned from dark green to bright orange. The reaction was finally quenched by addition of saturated $NaHCO_3$ solution. The mixture was extracted with 3 x 50 mL DCM. The combined organic layer was further washed with 100 mL water and 100 mL brine once, dried with $Na_2SO_4$, filtered, and concentrated under reduced pressure. The crude was separated through silica gel column chromatography using gradient elution from 50% DCM-hexanes to 100% DCM, followed by a 2$^{nd}$ gradient elution from 5% EtOAc-hexanes to 20% EtOAc-hexanes. The product was obtained as a white solid (0.205 g, 0.337 mmol, 95% yield). $R_f$ = 0.58 (25% EtOAc-hexanes). NOTE: The desired product and PMB-CHO byproduct showed similar polarities on the TLC plate. However, they could be separated effectively using two different gradient elution systems as mentioned above.

$^1$H NMR (500 MHz, Chloroform-*d*) δ 3.72 (d, *J* = 11.1 Hz, 1H), 3.61 (dd, *J* = 11.3, 3.4 Hz, 1H), 3.55 – 3.38 (m, 3H), 2.13 (s, 1H).

$^2$H NMR (77 MHz, Chloroform-regular) δ 3.65 – 3.29 (m, 4H), 1.50 (s, 4H), 1.18 (s, 52H), 0.82 (s, 6H).

$^{13}$C NMR (126 MHz, Chloroform-*d*) δ 78.33, 71.03, 63.26.

**(*R*)-2-(2,3-Bis((hexadecyl-$d_{33}$)oxy)propoxy)-1,3,2-dioxaphospholane 2-oxide (dPC-3)**

Compound **dPC-2** (82.7 mg, 0.136 mmol) and 4-dimethylaminopyridine (DMAP, 1.66 mg, 0.0136 mmol) were dissolved in 10 mL dry toluene in a 50 mL RBF under Argon at 0 °C. Next, 2-chloro-2-oxo-1,3,2-dioxaphospholane (COP, 37.3 µL, 0.408 mmol) was added into the RBF. After adding triethylamine (TEA, 56.8 µL, 0.408 mmol) in toluene dropwise, the reaction was warmed up to rt and stirred overnight. Upon completion, the precipitate formed during reaction was filtered off through a celite pad. The filtrate was concentrated under reduced pressure and purified via a silica gel column using gradient elution from

25% EtOAc-hexanes to 50% EtOAc-hexanes. The product was obtained as a clear oil (25.2 mg, 0.049 mmol, 36% yield). $R_f$ = 0.15 (50% EtOAc-Hexanes).
$^1$H NMR (500 MHz, Chloroform-*d*) δ 4.52 – 4.31 (m, 4H), 4.27 (td, *J* = 9.9, 8.8, 4.0 Hz, 1H), 4.16 (td, *J* = 10.3, 5.5 Hz, 1H), 3.62 (q, *J* = 4.9 Hz, 1H), 3.48 (q, *J* = 5.2 Hz, 2H).

$^{31}$P NMR (202 MHz, Chloroform-*d*) δ 17.57.

**(*R*)-2,3-Bis((hexadecyl-*d*$_{33}$)oxy)propyl (2-(trimethylammonio)ethyl) phosphate (dPC-4)**

Compound **dPC-3** (184 mg, 0.258 mmol) was dissolved in a pressure tube with 10 mL dry MeCN. After adding trimethylamine (TMA, 1.23 mL, 5.16 mmol, 4.2 M in EtOH), the reaction was stirred at 65 °C for 24 hours. Upon completion, the reaction mixture was transferred to a 50 mL RBF and the solvent was removed under reduced pressure. The crude was purified with a column packed with Iatrobead using gradient elution from 100% $CHCl_3$ to 65/25/4 $CHCl_3$/MeOH/$H_2O$ (v/v), followed by a final elution with 5/2 $CHCl_3$/10% $NH_4OH$ in MeOH (v/v). The final product was obtained as a clear wax (11 mg, 0.014 mmol, 5.5% yield). $R_f$ = 0.25 (65/25/4 $CHCl_3$/MeOH/$H_2O$ (v/v)).

$^1$H NMR (500 MHz, Chloroform-*d*) δ 4.29 (s, 2H), 3.99 – 3.66 (m, 4H), 3.64 – 3.42 (m, 5H), 3.42 – 3.05 (m, 9H).

$^2$H NMR (77 MHz, Chloroform-regular) δ 3.46 (s, 4H), 1.24 (s, 56H), 0.88 (s, 6H).

$^{13}$C NMR (126 MHz, Chloroform-*d*) δ 78.15, 70.85, 66.56, 65.18, 59.45, 54.62, 29.85, 28.58. $^{31}$P NMR (202 MHz, Chloroform-*d*) δ -0.78.

HRMS-DART: $[M+H]^+$ calcd for $C_{40}H_{19}D_{66}NO_6P$: 773.0252; Found: 773.9837.

**(*S*)-2,3-Bis(hexadecyloxy)propan-1-ol (PC-2)**

The same protocol used to synthesize **dPC-1** and **dPC-2** was followed. **CL-2** (0.2 g, 0.942 mmol), NaH (0.152 g, 3.77 mmol, 60% dispersion in mineral oil), TBAI (20 mg, 10% w/w of diol) and 1-bromohexadecane (0.72 mL, 2.36 mmol) afforded crude **PC-1**, which was passed along to PMB deprotection without further purification. The reaction crude and DDQ (0.43 g, 1.88 mmol) yielded the product as a while solid (0.397 g, 0.73 mmol, 78% yield over two steps). $R_f$ = 0.58 (25% EtOAc-hexanes).

$^{1}$H NMR (500 MHz, Chloroform-*d*) δ 3.72 (dd, *J* = 11.4, 3.8 Hz, 1H), 3.65 – 3.57 (m, 2H), 3.55 – 3.40 (m, 6H), 2.19 (s, 1H), 1.64 – 1.49 (m, 4H), 1.25 (s, 52H), 0.88 (t, *J* = 6.9 Hz, 6H).

$^{13}$C NMR (126 MHz, Chloroform-*d*)) δ 78.40, 72.01, 71.06, 70.55, 63.26, 32.08, 30.23, 29.85, 29.84, 29.82, 29.81, 29.77, 29.76, 29.62, 29.51, 26.25, 22.84, 14.26.

**(*R*)-2-(2,3-Bis(hexadecyloxy)propoxy)-1,3,2-dioxaphospholane 2-oxide (PC-3)**

The same protocol used to synthesize **dPC-3** was followed. **PC-2** (0.1 g, 0.185 mmol), DMAP (2.26 mg, 0.0185 mmol), COP (50 µL, 0.55 mmol) and TEA (76.5 µL, 0.55 mmol) yielded the product as a clear oil (47.1 mg, 0.073 mmol, 39% yield). $R_f$ = 0.15 (50% EtOAc-Hexanes).

$^{1}$H NMR (500 MHz, Chloroform-*d*) δ 4.49 – 4.32 (m, 4H), 4.27 (td, *J* = 10.0, 8.8, 4.0 Hz, 1H), 4.16 (td, *J* = 10.3, 5.5 Hz, 1H), 3.65 – 3.39 (m, 7H), 1.55 (dt, *J* = 16.6, 7.0 Hz, 4H), 1.25 (s, 52H), 0.88 (t, *J* = 6.8 Hz, 6H).

$^{13}$C NMR (126 MHz, Chloroform-*d*) δ 71.97, 70.88, 69.62, 68.23, 68.19, 66.06, 32.07, 30.09, 29.85, 29.81, 29.79, 29.77, 29.64, 29.51, 26.23, 26.16, 22.84, 14.26.

$^{31}$P NMR (202 MHz, Chloroform-*d*) δ 17.57.

**(*R*)-2,3-Bis(hexadecyloxy)propyl (2-(trimethylammonio)ethyl) phosphate (PC-4)**

The same protocol used to synthesize **dPC-4** was followed. **PC-3** (126 mg, 0.195 mmol) and TMA (0.93 mL, 3.9 mmol, 4.2 M in EtOH) yielded the product as a clear wax (11 mg, 0.0156 mmol, 8% yield). $R_f$ = 0.25 (65/25/4 $CHCl_3$/MeOH/$H_2O$ (v/v)).

$^{1}$H NMR (500 MHz, Chloroform-*d*) δ 4.47 – 4.11 (m, 2H), 3.80 (d, *J* = 38.7 Hz, 4H), 3.61 – 3.48 (m, 4H), 3.47 – 3.24 (m, 12H), 3.11 (s, 4H), 1.59 – 1.47 (m, 4H), 1.25 (s, 52H), 0.87 (t, *J* = 6.8 Hz, 6H).

$^{13}$C NMR (126 MHz, Chloroform-*d*) δ 78.25, 71.87, 70.95, 70.62, 66.58, 65.13, 59.40, 54.63, 32.09, 30.38, 29.91, 29.53, 26.32, 22.84, 14.27.

$^{31}$P NMR (202 MHz, Chloroform-*d*) δ -0.72

## References

(1) Korn, E. D. Structure and function of the plasma membrane: a biochemical perspective. *The Journal of general physiology* **1968**, *52* (1), 257-278.

(2) Harayama, T.; Riezman, H. Understanding the diversity of membrane lipid composition. *Nature reviews Molecular cell biology* **2018**, *19* (5), 281-296.

(3) Levental, K. R.; Lorent, J. H.; Lin, X.; Skinkle, A. D.; Surma, M. A.; Stockenbojer, E. A.; Gorfe, A. A.; Levental, I. Polyunsaturated lipids regulate membrane domain stability by tuning membrane order. *Biophysical journal* **2016**, *110* (8), 1800-1810.

(4) Lorent, J.; Levental, K. R.; Ganesan, L.; Rivera-Longsworth, G.; Sezgin, E.; Doktorova, M.; Lyman, E.; Levental, I. Plasma membranes are asymmetric in lipid unsaturation, packing and protein shape. *Nature chemical biology* **2020**, *16* (6), 644-652.

(5) Levental, K. R.; Surma, M. A.; Skinkle, A. D.; Lorent, J. H.; Zhou, Y.; Klose, C.; Chang, J. T.; Hancock, J. F.; Levental, I. ω-3 polyunsaturated fatty acids direct differentiation of the membrane phenotype in mesenchymal stem cells to potentiate osteogenesis. *Science advances* **2017**, *3* (11), eaao1193.

(6) Schade, D. S.; Shey, L.; Eaton, R. P. Cholesterol review: a metabolically important molecule. *Endocrine Practice* **2020**, *26* (12), 1514-1523.

(7) Chakraborty, S.; Doktorova, M.; Molugu, T. R.; Heberle, F. A.; Scott, H. L.; Dzikovski, B.; Nagao, M.; Stingaciu, L.-R.; Standaert, R. F.; Barrera, F. N. How cholesterol stiffens unsaturated lipid membranes. *Proceedings of the National Academy of Sciences* **2020**, *117* (36), 21896-21905.

(8) Mitchell, J. M.; Flight, R. M.; Moseley, H. N. Deriving lipid classification based on molecular formulas. *Metabolites* **2020**, *10* (3), 122.

(9) Jacobson, K.; Mouritsen, O. G.; Anderson, R. G. Lipid rafts: at a crossroad between cell biology and physics. *Nature cell biology* **2007**, *9* (1), 7-14.

(10) Doktorova, M.; Symons, J. L.; Levental, I. Structural and functional consequences of reversible lipid asymmetry in living membranes. *Nature chemical biology* **2020**, *16* (12), 1321-1330.

(11) Clarke, R. J.; Hossain, K. R.; Cao, K. Physiological roles of transverse lipid asymmetry of animal membranes. *Biochimica et Biophysica Acta (BBA)-Biomembranes* **2020**, *1862* (10), 183382.

(12) Singer, S. J.; Nicolson, G. L. The Fluid Mosaic Model of the Structure of Cell Membranes: Cell membranes are viewed as two-dimensional solutions of oriented globular proteins and lipids. *Science* **1972**, *175* (4023), 720-731.
(13) Shimshick, E. J.; Mcconnell, H. M. Lateral phase separation in phospholipid membranes. *Biochemistry* **1973**, *12* (12), 2351-2360.
(14) Wunderlich, F.; Kreutz, W.; Mahler, P.; Ronai, A.; Heppeler, G. Thermotropic fluid→ ordered" discontinuous" phase separation in microsomal lipids of Tetrahymena. An x-ray diffraction study. *Biochemistry* **1978**, *17* (10), 2005-2010.
(15) Florine, K. I.; Feigenson, G. W. Protein redistribution in model membranes: clearing of M13 coat protein from calcium-induced gel-phase regions in phosphatidylserine/phosphatidylcholine multilamellar vesicles. *Biochemistry* **1987**, *26* (11), 2978-2983.
(16) Sankaram, M. B.; Thompson, T. E. Cholesterol-induced fluid-phase immiscibility in membranes. *Proceedings of the National Academy of Sciences* **1991**, *88* (19), 8686-8690.
(17) Simons, K.; Ikonen, E. Functional rafts in cell membranes. *nature* **1997**, *387* (6633), 569-572.
(18) Almeida, P. F. Thermodynamics of lipid interactions in complex bilayers. *Biochimica et Biophysica Acta (BBA)-Biomembranes* **2009**, *1788* (1), 72-85.
(19) Sezgin, E.; Levental, I.; Mayor, S.; Eggeling, C. The mystery of membrane organization: composition, regulation and roles of lipid rafts. *Nature reviews Molecular cell biology* **2017**, *18* (6), 361-374.
(20) Heberle, F. A.; Feigenson, G. W. Phase separation in lipid membranes. *Cold Spring Harbor perspectives in biology* **2011**, *3* (4), a004630.
(21) Luchini, A.; Vitiello, G. Mimicking the mammalian plasma membrane: An overview of lipid membrane models for biophysical studies. *Biomimetics* **2020**, *6* (1), 3.
(22) Veatch, S. L.; Polozov, I.; Gawrisch, K.; Keller, S. L. Liquid domains in vesicles investigated by NMR and fluorescence microscopy. *Biophysical journal* **2004**, *86* (5), 2910-2922.
(23) Simons, K.; Vaz, W. L. Model systems, lipid rafts, and cell membranes. *Annu. Rev. Biophys. Biomol. Struct.* **2004**, *33*, 269-295.

(24) Feigenson, G. W. Phase diagrams and lipid domains in multicomponent lipid bilayer mixtures. *Biochimica et Biophysica Acta (BBA)-Biomembranes* **2009**, *1788* (1), 47-52.
(25) De Almeida, R. F.; Fedorov, A.; Prieto, M. Sphingomyelin/phosphatidylcholine/cholesterol phase diagram: boundaries and composition of lipid rafts. *Biophysical journal* **2003**, *85* (4), 2406-2416.
(26) Sharma, K. D.; Heberle, F. A.; Waxham, M. N. Visualizing lipid membrane structure with cryo-EM: past, present, and future. *Emerging Topics in Life Sciences* **2023**, *7* (1), 55-65.
(27) Mills, T. T.; Huang, J.; Feigenson, G. W.; Nagle, J. F. Effects of cholesterol and unsaturated DOPC lipid on chain packing of saturated gel-phase DPPC bilayers. *Biophysical Journal* **2009**, *96* (3), 605a.
(28) Vist, M. R.; Davis, J. H. Phase equilibria of cholesterol/dipalmitoylphosphatidylcholine mixtures: deuterium nuclear magnetic resonance and differential scanning calorimetry. *Biochemistry* **1990**, *29* (2), 451-464.
(29) Ipsen, J. H.; Karlström, G.; Mourtisen, O.; Wennerström, H.; Zuckermann, M. Phase equilibria in the phosphatidylcholine-cholesterol system. *Biochimica et Biophysica Acta (BBA)-Biomembranes* **1987**, *905* (1), 162-172.
(30) Lingwood, D.; Simons, K. Lipid rafts as a membrane-organizing principle. *science* **2010**, *327* (5961), 46-50.
(31) Mañes, S.; del Real, G.; Martínez-a, C. Pathogens: raft hijackers. *Nature Reviews Immunology* **2003**, *3* (7), 557-568.
(32) Kulkarni, R.; Wiemer, E. A.; Chang, W. Role of lipid rafts in pathogen-host interaction-a mini review. *Frontiers in Immunology* **2022**, *12*, 815020.
(33) Mesa-Herrera, F.; Taoro-González, L.; Valdés-Baizabal, C.; Diaz, M.; Marín, R. Lipid and lipid raft alteration in aging and neurodegenerative diseases: a window for the development of new biomarkers. *International journal of molecular sciences* **2019**, *20* (15), 3810.
(34) Schengrund, C.-L. Lipid rafts: keys to neurodegeneration. *Brain research bulletin* **2010**, *82* (1-2), 7-17.

(35) Sviridov, D.; Mukhamedova, N.; Miller, Y. I. Lipid rafts as a therapeutic target: thematic review series: biology of lipid rafts. *Journal of lipid research* **2020**, *61* (5), 687-695.
(36) Partlow, K. C.; Lanza, G. M.; Wickline, S. A. Exploiting lipid raft transport with membrane targeted nanoparticles: a strategy for cytosolic drug delivery. *Biomaterials* **2008**, *29* (23), 3367-3375.
(37) Feigenson, G. W. Phase boundaries and biological membranes. *Annu. Rev. Biophys. Biomol. Struct.* **2007**, *36*, 63-77.
(38) He, H.-T.; Marguet, D. Detecting nanodomains in living cell membrane by fluorescence correlation spectroscopy. *Annual review of physical chemistry* **2011**, *62*, 417-436.
(39) Veatch, S. L.; Keller, S. L. Separation of liquid phases in giant vesicles of ternary mixtures of phospholipids and cholesterol. *Biophysical journal* **2003**, *85* (5), 3074-3083.
(40) Veatch, S. L.; Keller, S. L. Seeing spots: complex phase behavior in simple membranes. *Biochimica et Biophysica Acta (BBA)-Molecular Cell Research* **2005**, *1746* (3), 172-185.
(41) Su, W.-C.; Ho, J. C.; Gettel, D. L.; Rowland, A. T.; Keating, C. D.; Parikh, A. N. Kinetic control of shape deformations and membrane phase separation inside giant vesicles. *Nature Chemistry* **2024**, *16* (1), 54-62.
(42) Wesołowska, O.; Michalak, K.; Maniewska, J.; Hendrich, A. B. Giant unilamellar vesicles-a perfect tool to visualize phase separation and lipid rafts in model systems. *Acta Biochimica Polonica* **2009**, *56* (1).
(43) Zong, W.; Shao, X.; Chai, Y.; Wang, X.; Han, S.; Chu, H.; Zhu, C.; Zhang, X. Liposomes encapsulating artificial cytosol as drug delivery system. *Biophysical Chemistry* **2022**, *281*, 106728.
(44) Lussier, F.; Staufer, O.; Platzman, I.; Spatz, J. P. Can bottom-up synthetic biology generate advanced drug-delivery systems? *Trends in Biotechnology* **2021**, *39* (5), 445-459.
(45) Li, Y.; Liu, S.; Xu, W.; Wang, K.; He, F.; Liu, J. Formation of giant plasma membrane vesicles for biological and medical applications: a review. *Sensors & Diagnostics* **2023**.

(46) Levental, K. R.; Levental, I. Giant plasma membrane vesicles: models for understanding membrane organization. *Current topics in membranes* **2015**, *75*, 25-57.
(47) Baumgart, T.; Hammond, A. T.; Sengupta, P.; Hess, S. T.; Holowka, D. A.; Baird, B. A.; Webb, W. W. Large-scale fluid/fluid phase separation of proteins and lipids in giant plasma membrane vesicles. *Proceedings of the National Academy of Sciences* **2007**, *104* (9), 3165-3170.
(48) Zemljič Jokhadar, Š.; Klančnik, U.; Grundner, M.; Švelc Kebe, T.; Vrhovec Hartman, S.; Liović, M.; Derganc, J. GPMVs in variable physiological conditions: could they be used for therapy delivery? *BMC biophysics* **2018**, *11*, 1-12.
(49) Leveille, C. L.; Cornell, C. E.; Merz, A. J.; Keller, S. L. Yeast cells actively tune their membranes to phase separate at temperatures that scale with growth temperatures. *Proceedings of the National Academy of Sciences* **2022**, *119* (4), e2116007119.
(50) Heberle, F. A.; Buboltz, J. T.; Stringer, D.; Feigenson, G. W. Fluorescence methods to detect phase boundaries in lipid bilayer mixtures. *Biochimica et Biophysica Acta (BBA)-Molecular Cell Research* **2005**, *1746* (3), 186-192.
(51) Levental, I.; Levental, K. R.; Heberle, F. A. Lipid rafts: controversies resolved, mysteries remain. *Trends in cell biology* **2020**, *30* (5), 341-353.
(52) Loura, L. M.; Prieto, M. FRET in membrane biophysics: An overview. *Frontiers in physiology* **2011**, *2*, 82.
(53) Enoki, T. A.; Heberle, F. A.; Feigenson, G. W. FRET detects the size of nanodomains for coexisting liquid-disordered and liquid-ordered phases. *Biophysical Journal* **2018**, *114* (8), 1921-1935.
(54) Pathak, P.; London, E. The effect of membrane lipid composition on the formation of lipid ultrananodomains. *Biophysical journal* **2015**, *109* (8), 1630-1638.
(55) Trusova, V. M.; Gorbenko, G. P.; Deligeorgiev, T.; Gadjev, N. Probing protein–lipid interactions by FRET between membrane fluorophores. *Methods and Applications in Fluorescence* **2016**, *4* (3), 034014.
(56) Heller, W. T. Small-angle neutron scattering for studying lipid bilayer membranes. *Biomolecules* **2022**, *12* (11), 1591.

(57) Heberle, F. A.; Petruzielo, R. S.; Pan, J.; Drazba, P.; Kucerka, N.; Standaert, R. F.; Feigenson, G. W.; Katsaras, J. Bilayer thickness mismatch controls domain size in model membranes. *Journal of the American Chemical Society* **2013**, *135* (18), 6853-6859.
(58) Lawrence, J. C.; Saslowsky, D. E.; Edwardson, J. M.; Henderson, R. M. Real-time analysis of the effects of cholesterol on lipid raft behavior using atomic force microscopy. *Biophysical journal* **2003**, *84* (3), 1827-1832.
(59) Quinn, P. J.; Wolf, C. An X-ray diffraction study of model membrane raft structures. *The FEBS Journal* **2010**, *277* (22), 4685-4698.
(60) Fritzsching, K. J.; Kim, J.; Holland, G. P. Probing lipid–cholesterol interactions in DOPC/eSM/Chol and DOPC/DPPC/Chol model lipid rafts with DSC and 13C solid-state NMR. *Biochimica et Biophysica Acta (BBA)-Biomembranes* **2013**, *1828* (8), 1889-1898.
(61) Cai, M.; Zhao, W.; Shang, X.; Jiang, J.; Ji, H.; Tang, Z.; Wang, H. Direct evidence of lipid rafts by in situ atomic force microscopy. *Small* **2012**, *8* (8), 1243-1250.
(62) Binder, W. H.; Barragan, V.; Menger, F. M. Domains and rafts in lipid membranes. *Angewandte Chemie International Edition* **2003**, *42* (47), 5802-5827.
(63) Yasuda, T.; Tsuchikawa, H.; Murata, M.; Matsumori, N. Deuterium NMR of raft model membranes reveals domain-specific order profiles and compositional distribution. *Biophysical Journal* **2015**, *108* (10), 2502-2506.
(64) McIntosh, T. J. X-ray diffraction analysis of membrane lipids. In *AMolecular Description of Biological Membrane Components by Computer Aided Conformational Analysis*, CRC Press, 2019; pp 247-266.
(65) Bennett, W. D.; Tieleman, D. P. Computer simulations of lipid membrane domains. *Biochimica et Biophysica Acta (BBA)-Biomembranes* **2013**, *1828* (8), 1765-1776.
(66) Venable, R. M.; Brown, F. L.; Pastor, R. W. Mechanical properties of lipid bilayers from molecular dynamics simulation. *Chemistry and physics of lipids* **2015**, *192*, 60-74.
(67) Heberle, F. A.; Doktorova, M.; Scott, H. L.; Skinkle, A. D.; Waxham, M. N.; Levental, I. Direct label-free imaging of nanodomains in biomimetic and biological membranes by cryogenic electron microscopy. *Proceedings of the National Academy of Sciences* **2020**, *117* (33), 19943-19952.
(68) Wang, H. W.; Wang, J. W. How cryo-electron microscopy and X-ray crystallography complement each other. *Protein Science* **2017**, *26* (1), 32-39.

(69) Kühlbrandt, W. Cryo-EM enters a new era. *elife* **2014**, *3*, e03678.
(70) Egelman, E. H. The current revolution in cryo-EM. *Biophysical journal* **2016**, *110* (5), 1008-1012.
(71) Fischer, T. D.; Dash, P. K.; Liu, J.; Waxham, M. N. Morphology of mitochondria in spatially restricted axons revealed by cryo-electron tomography. *PLoS biology* **2018**, *16* (9), e2006169.
(72) Van Meer, G.; Voelker, D. R.; Feigenson, G. W. Membrane lipids: where they are and how they behave. *Nature reviews Molecular cell biology* **2008**, *9* (2), 112-124.
(73) Koynova, R.; Tenchov, B. Phase transitions and phase behavior of lipids. *Encyclopedia of Biophysics* **2013**, 1841-1854.
(74) Marsh, D. Liquid-ordered phases induced by cholesterol: a compendium of binary phase diagrams. *Biochimica et Biophysica Acta (BBA)-Biomembranes* **2010**, *1798* (3), 688-699.
(75) Marsh, D. Cholesterol-induced fluid membrane domains: a compendium of lipid-raft ternary phase diagrams. *Biochimica et Biophysica Acta (BBA)-Biomembranes* **2009**, *1788* (10), 2114-2123.
(76) Petrache, H. I.; Dodd, S. W.; Brown, M. F. Area per lipid and acyl length distributions in fluid phosphatidylcholines determined by 2H NMR spectroscopy. *Biophysical journal* **2000**, *79* (6), 3172-3192.
(77) Kučerka, N.; Heberle, F. A.; Pan, J.; Katsaras, J. Structural significance of lipid diversity as studied by small angle neutron and X-ray scattering. *Membranes* **2015**, *5* (3), 454-472.
(78) Heberle, F. A.; Pan, J.; Standaert, R. F.; Drazba, P.; Kučerka, N.; Katsaras, J. Model-based approaches for the determination of lipid bilayer structure from small-angle neutron and X-ray scattering data. *European Biophysics Journal* **2012**, *41*, 875-890.
(79) Simons, K.; Gerl, M. J. Revitalizing membrane rafts: new tools and insights. *Nature reviews Molecular cell biology* **2010**, *11* (10), 688-699.
(80) Eggeling, C.; Ringemann, C.; Medda, R.; Schwarzmann, G.; Sandhoff, K.; Polyakova, S.; Belov, V. N.; Hein, B.; Von Middendorff, C.; Schönle, A. Direct observation of the nanoscale dynamics of membrane lipids in a living cell. *Nature* **2009**, *457* (7233), 1159-1162.

(81) Lepault, J.; Pattus, F.; Martin, N. Cryo-electron microscopy of artificial biological membranes. *Biochimica et Biophysica Acta (BBA)-Biomembranes* **1985**, *820* (2), 315-318.
(82) Tahara, Y.; Fujiyoshi, Y. A new method to measure bilayer thickness: cryo-electron microscopy of frozen hydrated liposomes and image simulation. *Micron* **1994**, *25* (2), 141-149.
(83) Tristram-Nagle, S.; Liu, Y.; Legleiter, J.; Nagle, J. F. Structure of gel phase DMPC determined by X-ray diffraction. *Biophysical journal* **2002**, *83* (6), 3324-3335.
(84) Sun, W.; Tristram-Nagle, S.; Suter, R.; Nagle, J. Structure of gel phase saturated lecithin bilayers: temperature and chain length dependence. *Biophysical journal* **1996**, *71* (2), 885-891.
(85) Kučerka, N.; Gallová, J.; Uhríková, D.; Balgavý, P.; Bulacu, M.; Marrink, S.-J.; Katsaras, J. Areas of monounsaturated diacylphosphatidylcholines. *Biophysical Journal* **2009**, *97* (7), 1926-1932.
(86) Wang, L.; Bose, P. S.; Sigworth, F. J. Using cryo-EM to measure the dipole potential of a lipid membrane. *Proceedings of the National Academy of Sciences* **2006**, *103* (49), 18528-18533.
(87) Engstrom, T.; Clinger, J. A.; Spoth, K. A.; Clarke, O. B.; Closs, D. S.; Jayne, R.; Apker, B. A.; Thorne, R. E. High-resolution single-particle cryo-EM of samples vitrified in boiling nitrogen. *IUCrJ* **2021**, *8* (6), 867-877.
(88) Bag, N.; Yap, D. H. X.; Wohland, T. Temperature dependence of diffusion in model and live cell membranes characterized by imaging fluorescence correlation spectroscopy. *Biochimica et Biophysica Acta (BBA)-Biomembranes* **2014**, *1838* (3), 802-813.
(89) Venable, R. M.; Zhang, Y.; Hardy, B. J.; Pastor, R. W. Molecular dynamics simulations of a lipid bilayer and of hexadecane: an investigation of membrane fluidity. *Science* **1993**, *262* (5131), 223-226.
(90) Klauda, J. B.; Roberts, M. F.; Redfield, A. G.; Brooks, B. R.; Pastor, R. W. Rotation of lipids in membranes: molecular dynamics simulation, 31P spin-lattice relaxation, and rigid-body dynamics. *Biophysical journal* **2008**, *94* (8), 3074-3083.

(91) Marquardt, D.; Heberle, F. A.; Miti, T.; Eicher, B.; London, E.; Katsaras, J.; Pabst, G. 1H NMR shows slow phospholipid flip-flop in gel and fluid bilayers. *Langmuir* **2017**, *33* (15), 3731-3741.
(92) Heftberger, P.; Kollmitzer, B.; Rieder, A. A.; Amenitsch, H.; Pabst, G. In situ determination of structure and fluctuations of coexisting fluid membrane domains. *Biophysical journal* **2015**, *108* (4), 854-862.
(93) Cornell, C. E.; Mileant, A.; Thakkar, N.; Lee, K. K.; Keller, S. L. Direct imaging of liquid domains in membranes by cryo-electron tomography. *Proceedings of the National Academy of Sciences* **2020**, *117* (33), 19713-19719.
(94) Heberle, F. A.; Welsch, D.; Scott, H. L.; Waxham, M. N. Optimization of cryo-electron microscopy for quantitative analysis of lipid bilayers. *Biophysical Reports* **2023**, *3* (1).
(95) Allender, D. W.; Schick, M. Recent experiments support a microemulsion origin of plasma membrane domains: Dependence of domain size on physical parameters. *Membranes* **2020**, *10* (8), 167.
(96) Feigenson, G. W. On the small size of liquid-disordered+ liquid-ordered nanodomains. *Biochimica et Biophysica Acta (BBA)-Biomembranes* **2021**, *1863* (10), 183685.
(97) Palmieri, B.; Safran, S. A. Hybrid lipids increase the probability of fluctuating nanodomains in mixed membranes. *Langmuir* **2013**, *29* (17), 5246-5261.
(98) Shaw, T. R.; Ghosh, S.; Veatch, S. L. Critical phenomena in plasma membrane organization and function. *Annual review of physical chemistry* **2021**, *72*, 51-72.
(99) Penczek, P. A. Image restoration in cryo-electron microscopy. In *Methods in enzymology*, Vol. 482; Elsevier, 2010; pp 35-72.
(100) Kollmitzer, B.; Heftberger, P.; Podgornik, R.; Nagle, J. F.; Pabst, G. Bending rigidities and interdomain forces in membranes with coexisting lipid domains. *Biophysical journal* **2015**, *108* (12), 2833-2842.
(101) Das, C.; Sheikh, K. H.; Olmsted, P. D.; Connell, S. D. Nanoscale mechanical probing of supported lipid bilayers with atomic force microscopy. *Physical Review E* **2010**, *82* (4), 041920.

(102) Levental, I.; Lyman, E. Regulation of membrane protein structure and function by their lipid nano-environment. *Nature Reviews Molecular Cell Biology* **2023**, *24* (2), 107-122.
(103) Cornell, C. E.; Skinkle, A. D.; He, S.; Levental, I.; Levental, K. R.; Keller, S. L. Tuning length scales of small domains in cell-derived membranes and synthetic model membranes. *Biophysical Journal* **2018**, *115* (4), 690-701.
(104) Pfab, J.; Phan, N. M.; Si, D. DeepTracer for fast de novo cryo-EM protein structure modeling and special studies on CoV-related complexes. *Proceedings of the National Academy of Sciences* **2021**, *118* (2), e2017525118.
(105) Bepler, T.; Kelley, K.; Noble, A. J.; Berger, B. Topaz-Denoise: general deep denoising models for cryoEM and cryoET. *Nature communications* **2020**, *11* (1), 5208.
(106) Tegunov, D.; Xue, L.; Dienemann, C.; Cramer, P.; Mahamid, J. Multi-particle cryo-EM refinement with M visualizes ribosome-antibiotic complex at 3.5 Å in cells. *Nature methods* **2021**, *18* (2), 186-193.
(107) Ronneberger, O.; Fischer, P.; Brox, T. U-net: Convolutional networks for biomedical image segmentation. In *Medical image computing and computer-assisted intervention–MICCAI 2015: 18th international conference, Munich, Germany, October 5-9, 2015, proceedings, part III 18*, 2015; Springer: pp 234-241.
(108) Sanchez-Garcia, R.; Gomez-Blanco, J.; Cuervo, A.; Carazo, J. M.; Sorzano, C. O. S.; Vargas, J. DeepEMhancer: a deep learning solution for cryo-EM volume post-processing. *Communications biology* **2021**, *4* (1), 874.
(109) Zhong, E. D.; Bepler, T.; Berger, B.; Davis, J. H. CryoDRGN: reconstruction of heterogeneous cryo-EM structures using neural networks. *Nature methods* **2021**, *18* (2), 176-185.
(110) Yao, X.; Fan, X.; Yan, N. Cryo-EM analysis of a membrane protein embedded in the liposome. *Proceedings of the National Academy of Sciences* **2020**, *117* (31), 18497-18503.
(111) Baker, M. R.; Fan, G.; Seryshev, A. B.; Agosto, M. A.; Baker, M. L.; Serysheva, I. I. Cryo-EM structure of type 1 IP3R channel in a lipid bilayer. *Communications biology* **2021**, *4* (1), 625.

(112) Doyle, M. T.; Jimah, J. R.; Dowdy, T.; Ohlemacher, S. I.; Larion, M.; Hinshaw, J. E.; Bernstein, H. D. Cryo-EM structures reveal multiple stages of bacterial outer membrane protein folding. *Cell* **2022**, *185* (7), 1143-1156. e1113.
(113) Tao, X.; Zhao, C.; MacKinnon, R. Membrane protein isolation and structure determination in cell-derived membrane vesicles. *Proceedings of the National Academy of Sciences* **2023**, *120* (18), e2302325120.
(114) Biou, V. Lipid-membrane protein interaction visualised by cryo-EM: a review. *Biochimica et Biophysica Acta (BBA)-Biomembranes* **2023**, *1865* (1), 184068.
(115) Ward, A. E.; Sokovikova, D.; Waxham, M. N.; Heberle, F. A.; Levental, I.; Levental, K. R.; Kiessling, V.; White, J. M.; Tamm, L. K. Serinc5 restricts HIV membrane fusion by altering lipid order and heterogeneity in the viral membrane. *ACS Infectious Diseases* **2023**, *9* (4), 773-784.
(116) Bleecker, J. V.; Cox, P. A.; Foster, R. N.; Litz, J. P.; Blosser, M. C.; Castner, D. G.; Keller, S. L. Thickness mismatch of coexisting liquid phases in noncanonical lipid bilayers. *The journal of physical chemistry B* **2016**, *120* (10), 2761-2770.
(117) Phillips, J. C.; Braun, R.; Wang, W.; Gumbart, J.; Tajkhorshid, E.; Villa, E.; Chipot, C.; Skeel, R. D.; Kale, L.; Schulten, K. Scalable molecular dynamics with NAMD. *Journal of computational chemistry* **2005**, *26* (16), 1781-1802.
(118) Klauda, J. B.; Venable, R. M.; Freites, J. A.; O'Connor, J. W.; Tobias, D. J.; Mondragon-Ramirez, C.; Vorobyov, I.; MacKerell Jr, A. D.; Pastor, R. W. Update of the CHARMM all-atom additive force field for lipids: validation on six lipid types. *The journal of physical chemistry B* **2010**, *114* (23), 7830-7843.
(119) Klauda, J. B.; Monje, V.; Kim, T.; Im, W. Improving the CHARMM force field for polyunsaturated fatty acid chains. *The journal of physical chemistry B* **2012**, *116* (31), 9424-9431.
(120) Jo, S.; Kim, T.; Iyer, V. G.; Im, W. CHARMM-GUI: a web-based graphical user interface for CHARMM. *Journal of computational chemistry* **2008**, *29* (11), 1859-1865.
(121) Jo, S.; Lim, J. B.; Klauda, J. B.; Im, W. CHARMM-GUI Membrane Builder for mixed bilayers and its application to yeast membranes. *Biophysical journal* **2009**, *97* (1), 50-58.
(122) Lee, J.; Cheng, X.; Jo, S.; MacKerell, A. D.; Klauda, J. B.; Im, W. CHARMM-GUI input generator for NAMD, GROMACS, AMBER, OpenMM, and CHARMM/OpenMM

simulations using the CHARMM36 additive force field. *Biophysical journal* **2016**, *110* (3), 641a.
(123) Doktorova, M.; LeVine, M. V.; Khelashvili, G.; Weinstein, H. A new computational method for membrane compressibility: Bilayer mechanical thickness revisited. *Biophysical journal* **2019**, *116* (3), 487-502.
(124) Humphrey, W.; Dalke, A.; Schulten, K. VMD: visual molecular dynamics. *Journal of molecular graphics* **1996**, *14* (1), 33-38.
(125) Sachs, J. N.; Crozier, P. S.; Woolf, T. B. Atomistic simulations of biologically realistic transmembrane potential gradients. *The Journal of chemical physics* **2004**, *121* (22), 10847-10851.
(126) Gurtovenko, A. A.; Vattulainen, I. Calculation of the electrostatic potential of lipid bilayers from molecular dynamics simulations: Methodological issues. *The Journal of chemical physics* **2009**, *130* (21).
(127) Kiewisz, R.; Fabig, G.; Müller-Reichert, T.; Bepler, T. Automated Segmentation of 3D Cytoskeletal Filaments from Electron Micrographs with TARDIS. Oxford University Press US: 2023.
(128) Zhao, J.; Wu, J.; Heberle, F. A.; Mills, T. T.; Klawitter, P.; Huang, G.; Costanza, G.; Feigenson, G. W. Phase studies of model biomembranes: complex behavior of DSPC/DOPC/cholesterol. *Biochimica et Biophysica Acta (BBA)-Biomembranes* **2007**, *1768* (11), 2764-2776.
(129) Heberle, F. A.; Wu, J.; Goh, S. L.; Petruzielo, R. S.; Feigenson, G. W. Comparison of three ternary lipid bilayer mixtures: FRET and ESR reveal nanodomains. *Biophysical journal* **2010**, *99* (10), 3309-3318.
(130) Konyakhina, T. M.; Goh, S. L.; Amazon, J.; Heberle, F. A.; Wu, J.; Feigenson, G. W. Control of a nanoscopic-to-macroscopic transition: modulated phases in four-component DSPC/DOPC/POPC/Chol giant unilamellar vesicles. *Biophysical journal* **2011**, *101* (2), L8-L10.
(131) McMahon, H. T.; Boucrot, E. Membrane curvature at a glance. *Journal of cell science* **2015**, *128* (6), 1065-1070.
(132) Jarsch, I. K.; Daste, F.; Gallop, J. L. Membrane curvature in cell biology: An integration of molecular mechanisms. *Journal of Cell Biology* **2016**, *214* (4), 375-387.

(133) Kozlov, M. M.; Taraska, J. W. Generation of nanoscopic membrane curvature for membrane trafficking. *Nature reviews Molecular cell biology* **2023**, *24* (1), 63-78.
(134) Risselada, H. J.; Marrink, S. J. Curvature effects on lipid packing and dynamics in liposomes revealed by coarse grained molecular dynamics simulations. *Physical Chemistry Chemical Physics* **2009**, *11* (12), 2056-2067.
(135) Baxter, W. T.; Grassucci, R. A.; Gao, H.; Frank, J. Determination of signal-to-noise ratios and spectral SNRs in cryo-EM low-dose imaging of molecules. *Journal of structural biology* **2009**, *166* (2), 126-132.
(136) Scheres, S. H.; Núñez-Ramírez, R.; Gómez-Llorente, Y.; San Martín, C.; Eggermont, P. P.; Carazo, J. M. Modeling experimental image formation for likelihood-based classification of electron microscopy data. *Structure* **2007**, *15* (10), 1167-1177.
(137) Sharma, K. D.; Doktorova, M.; Waxham, M. N.; Heberle, F. A. Cryo-EM images of phase separated lipid bilayer vesicles analyzed with a machine learning approach. *Biophysical Journal* **2024**.
(138) Larsen, J.; Hatzakis, N. S.; Stamou, D. Observation of inhomogeneity in the lipid composition of individual nanoscale liposomes. *Journal of the American Chemical Society* **2011**, *133* (28), 10685-10687.
(139) Sharma, K. D.; Doktorova, M.; Mehta, D.; Waxham, N.; Heberle, F. A. Using machine learning to characterize the structure of coexisting liquid-ordered and liquid-disordered phases from cryo-EM images of lipid vesicles. *Biophysical Journal* **2024**, *123* (3), 88a.
(140) Goh, S. L.; Amazon, J. J.; Feigenson, G. W. Toward a better raft model: modulated phases in the four-component bilayer, DSPC/DOPC/POPC/CHOL. *Biophysical journal* **2013**, *104* (4), 853-862.
(141) Usery, R. D.; Enoki, T. A.; Wickramasinghe, S. P.; Weiner, M. D.; Tsai, W.-C.; Kim, M. B.; Wang, S.; Torng, T. L.; Ackerman, D. G.; Heberle, F. A. Line tension controls liquid-disordered+ liquid-ordered domain size transition in lipid bilayers. *Biophysical journal* **2017**, *112* (7), 1431-1443.
(142) Esposito, C.; Tian, A.; Melamed, S.; Johnson, C.; Tee, S.-Y.; Baumgart, T. Flicker spectroscopy of thermal lipid bilayer domain boundary fluctuations. *Biophysical journal* **2007**, *93* (9), 3169-3181.

(143) Sarkar, P.; Chattopadhyay, A. Membrane dipole potential: An emerging approach to explore membrane organization and function. *The Journal of Physical Chemistry B* **2022**, *126* (24), 4415-4430.
(144) Amazon, J. J.; Feigenson, G. W. Lattice simulations of phase morphology on lipid bilayers: Renormalization, membrane shape, and electrostatic dipole interactions. *Physical Review E* **2014**, *89* (2), 022702.
(145) Angelova, M. I.; Dimitrov, D. S. Liposome electroformation. *Faraday discussions of the Chemical Society* **1986**, *81*, 303-311.
(146) Buboltz, J. T.; Feigenson, G. W. A novel strategy for the preparation of liposomes: rapid solvent exchange. *Biochimica et Biophysica Acta (BBA)-Biomembranes* **1999**, *1417* (2), 232-245.
(147) Clarke, R. J. The dipole potential of phospholipid membranes and methods for its detection. *Advances in colloid and interface science* **2001**, *89*, 263-281.
(148) Starke-Peterkovic, T.; Turner, N.; Vitha, M. F.; Waller, M. P.; Hibbs, D. E.; Clarke, R. J. Cholesterol effect on the dipole potential of lipid membranes. *Biophysical journal* **2006**, *90* (11), 4060-4070.
(149) Pencer, J.; Anghel, V. N. P.; Kucerka, N.; Katsaras, J. Scattering from laterally heterogeneous vesicles. I. Model-independent analysis. *Journal of Applied Crystalography* **2006**, *39*, 791-796.
(150) Heberle, F. A.; Petruzielo, R. S.; Pan, J.; Drazba, P.; Kucerka, N.; Standaert, R. F.; Feigenson, G. W.; Katsaras, J. Bilayer thickness mismatch controls domain size in model membranes. *J Am Chem Soc* **2013**, *135* (18), 6853-6859. DOI: 10.1021/ja3113615.
(151) Clarke, R. J. Effect of lipid structure on the dipole potential of phosphatidylcholine bilayers. *Biochimica et Biophysica Acta (BBA)-Biomembranes* **1997**, *1327* (2), 269-278.
(152) Gross, E.; Bedlack, R.; Loew, L. M. Dual-wavelength ratiometric fluorescence measurement of the membrane dipole potential. *Biophysical journal* **1994**, *67* (1), 208-216.
(153) Wang, L. Measurements and implications of the membrane dipole potential. *Annual review of biochemistry* **2012**, *81*, 615-635.
(154) Bandyopadhyay, S.; Bong, D. Synthesis of Trifunctional Phosphatidylserine Probes for Identification of Lipid-Binding Proteins. *Eur. J. Org. Chem.* **2011**, *2011* (4), 751-758.

# Appendix

**$^1$H NMR**

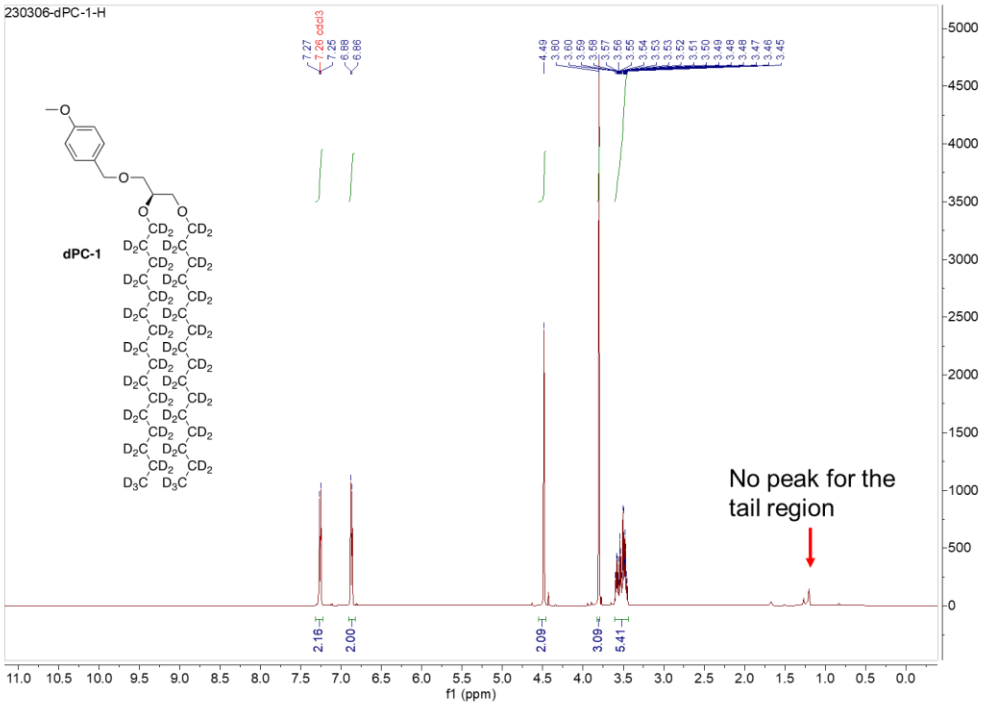


**$^2$H NMR**

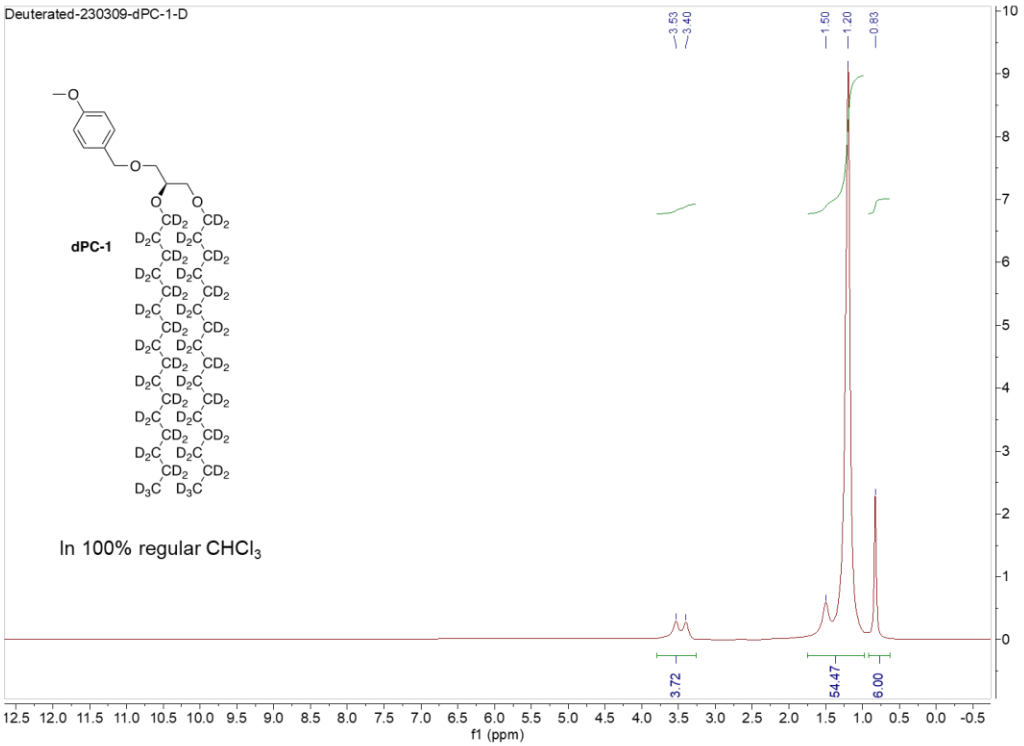

**$^{13}$C NMR**

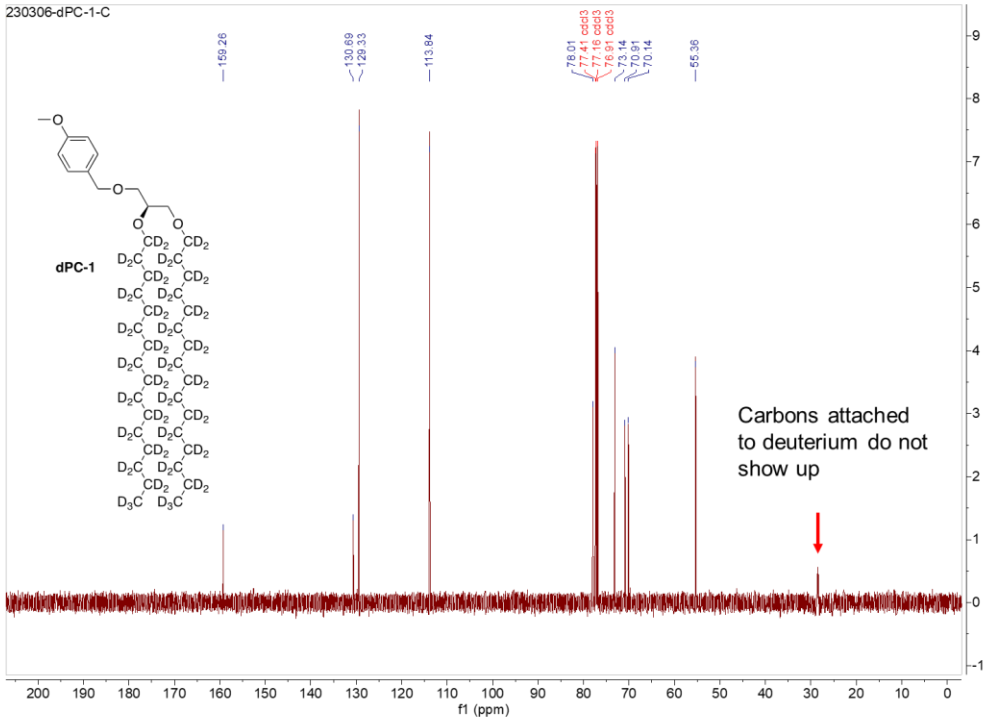
230306-dPC-1-C
159.26
130.69
129.33
113.84
78.01
77.41 cdd3
77.16 cdd3
76.91 cdd3
73.14
70.91
70.14
55.36
dPC-1
Carbons attached to deuterium do not show up
f1 (ppm)

**$^1$H NMR**

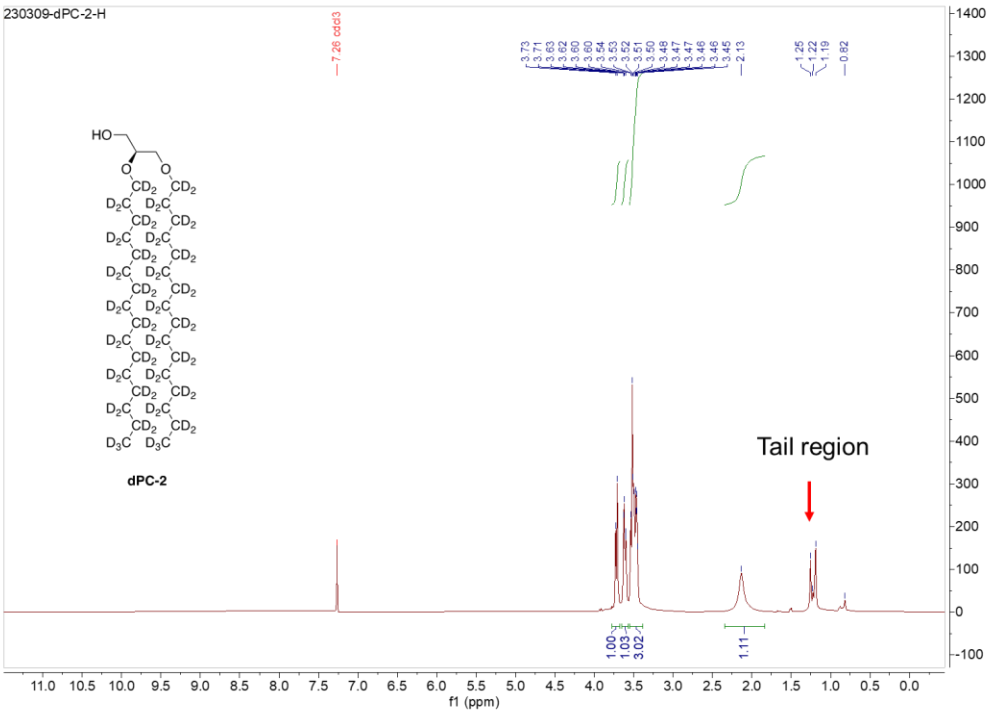
230309-dPC-2-H
dPC-2
Tail region
f1 (ppm)

**$^2$H NMR**

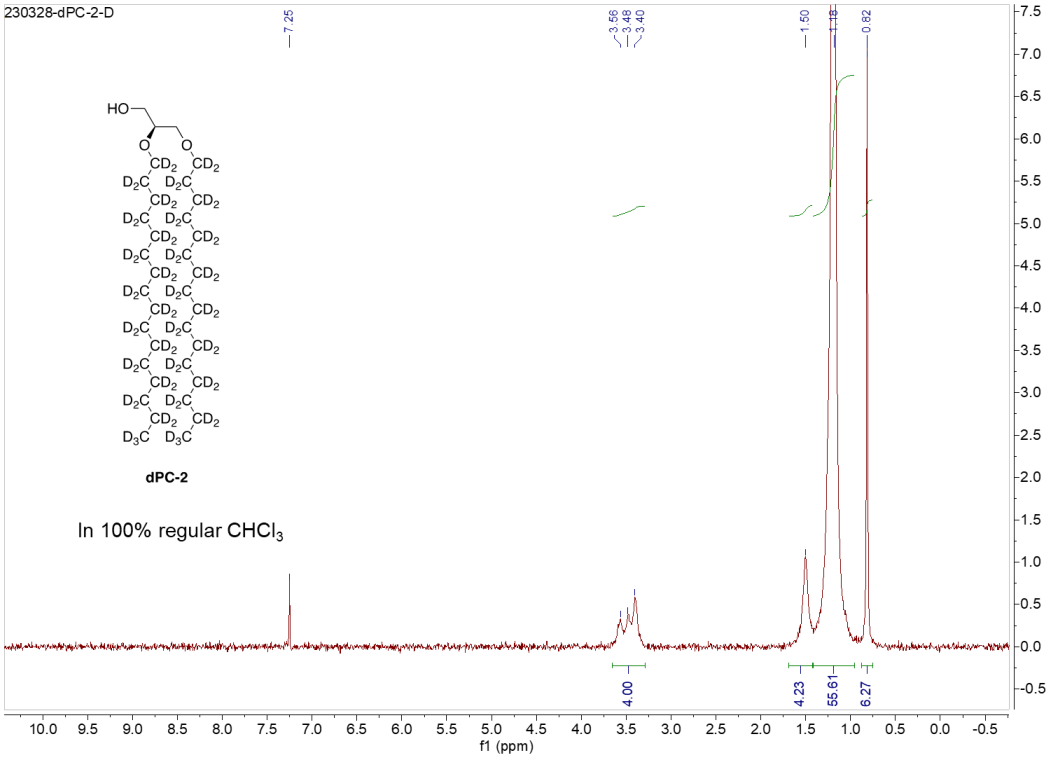
230328-dPC-2-D
dPC-2
In 100% regular CHCl3
f1 (ppm)

**$^{13}$C NMR**

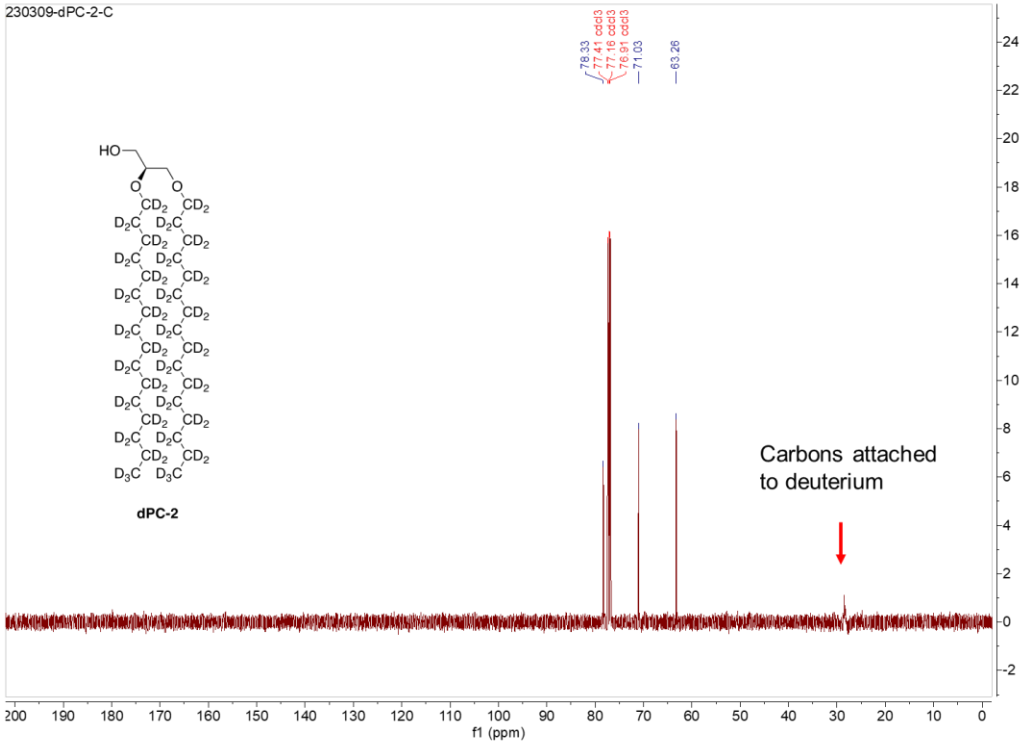


**$^{1}$H NMR**

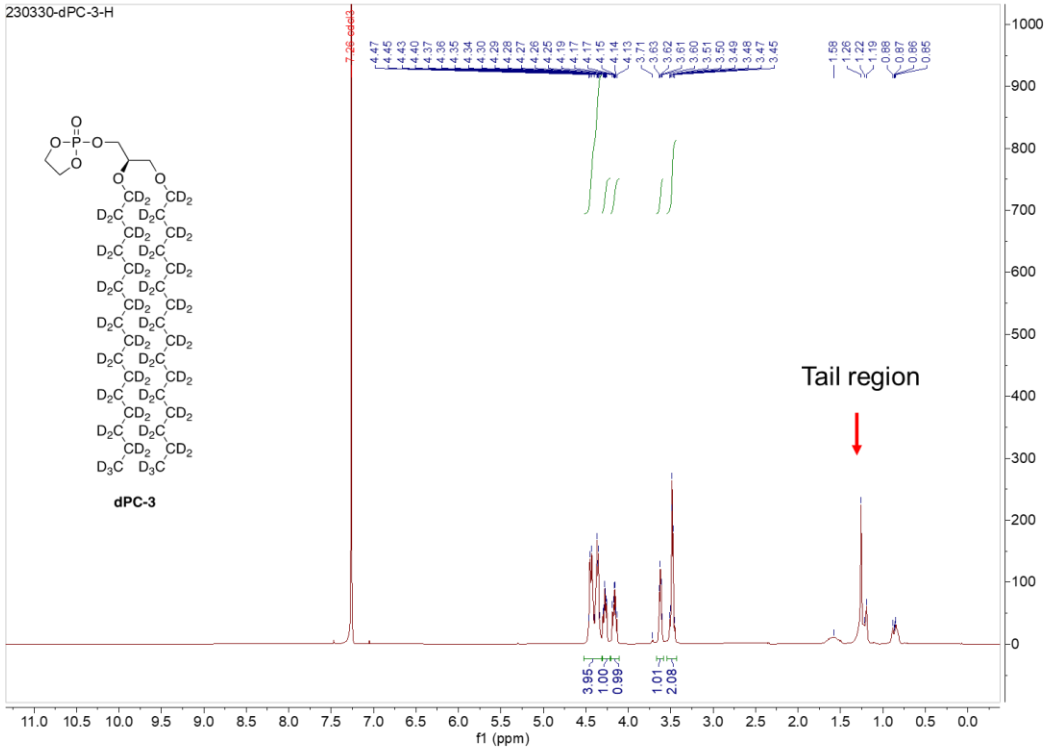

**$^{31}$P NMR**

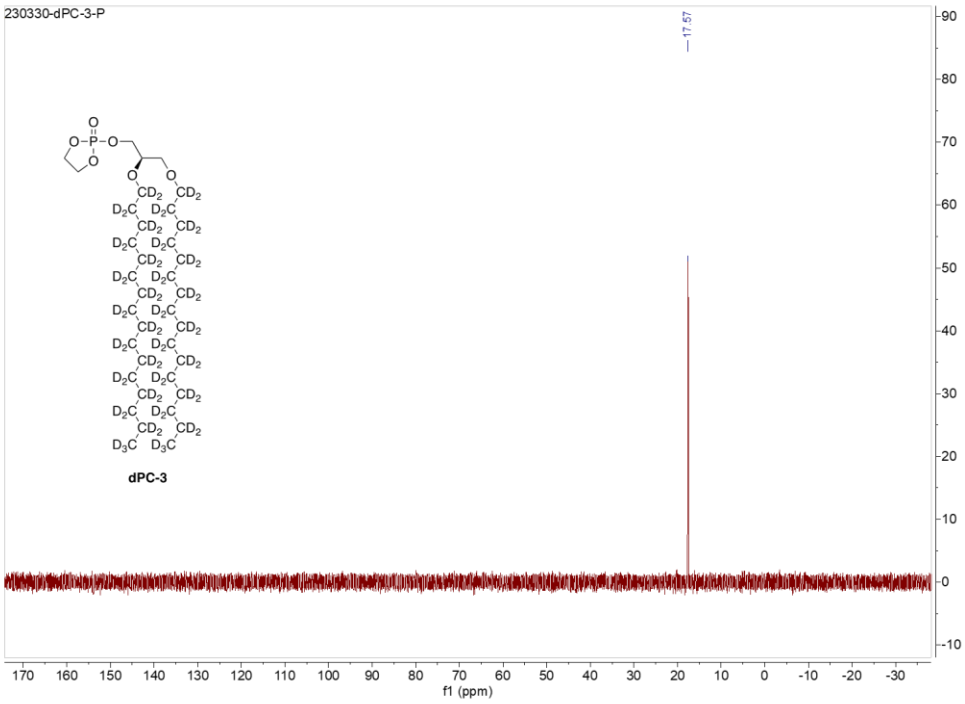
230330-dPC-3-P
17.57
dPC-3
90
80
70
60
50
40
30
20
10
0
-10
170 160 150 140 130 120 110 100 90 80 70 60 50 40 30 20 10 0 -10 -20 -30
f1 (ppm)

**$^1$H NMR**

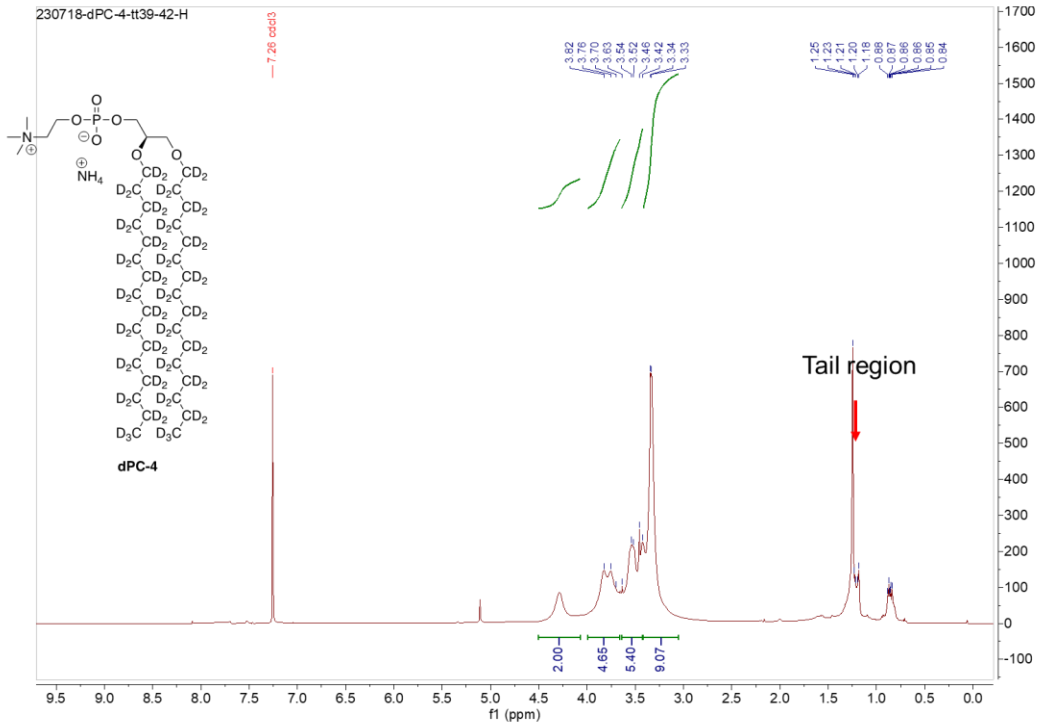
230718-dPC-4-tt39-42-H
dPC-4
Tail region
f1 (ppm)

**$^2$H NMR**

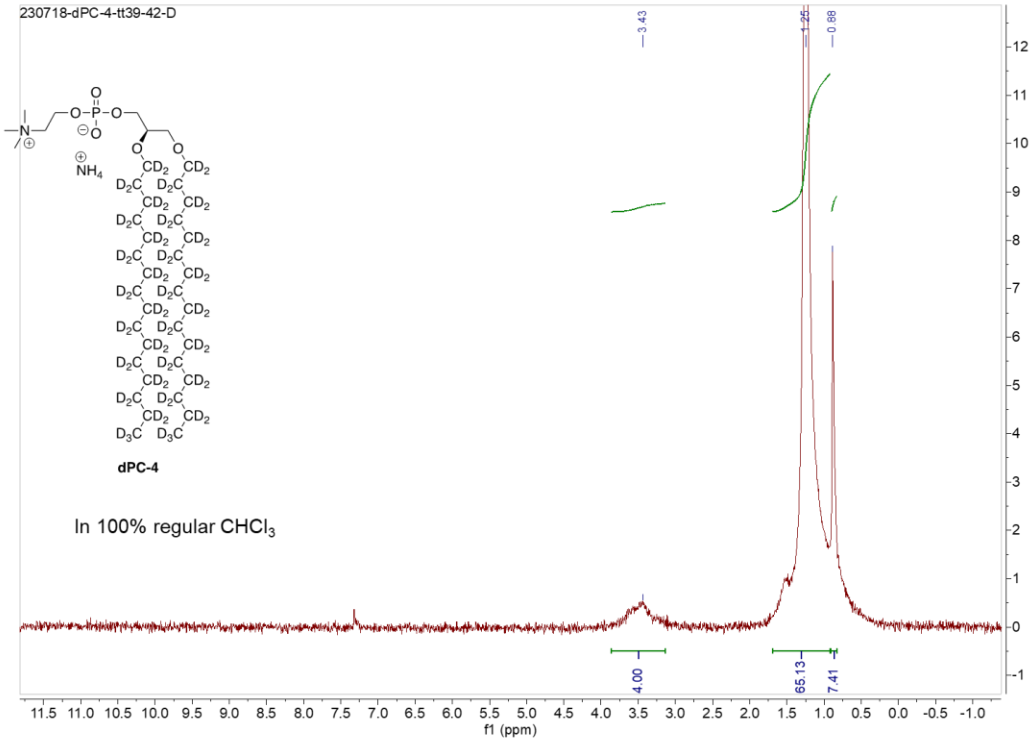
230718-dPC-4-tt39-42-D
dPC-4
In 100% regular CHCl3
f1 (ppm)

**$^{13}$C NMR**

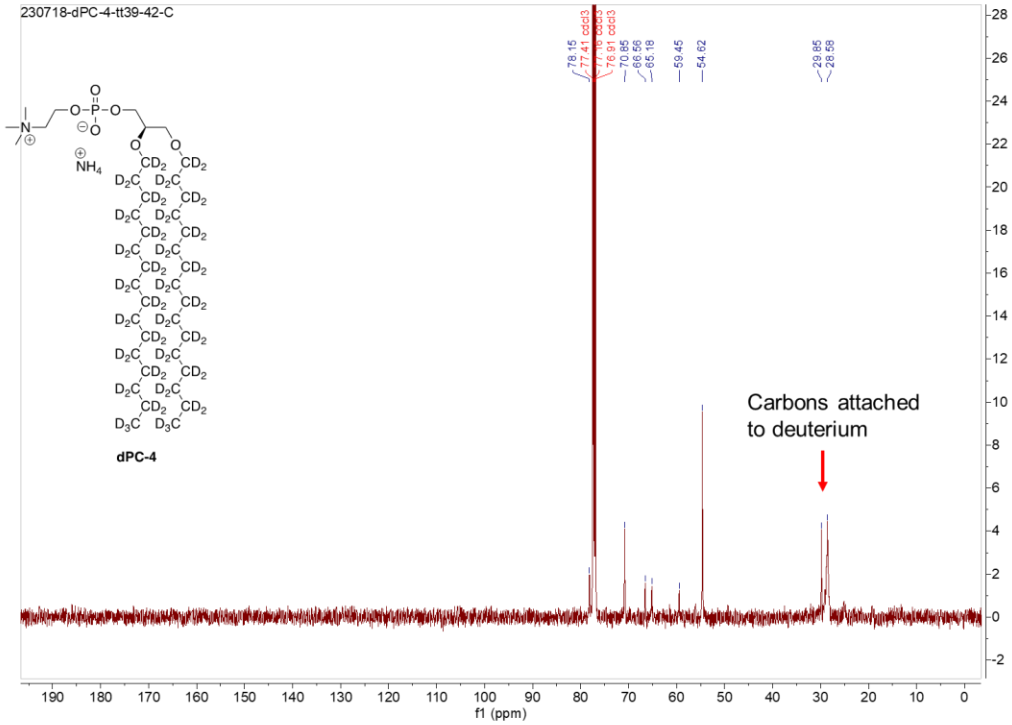
230718-dPC-4-tt39-42-C
dPC-4
78.15
77.41 cdcl3
77.16 cdcl3
76.91 cdcl3
70.85
66.56
65.18
59.45
54.62
29.85
29.58
Carbons attached
to deuterium
f1 (ppm)

**$^{31}$P NMR**

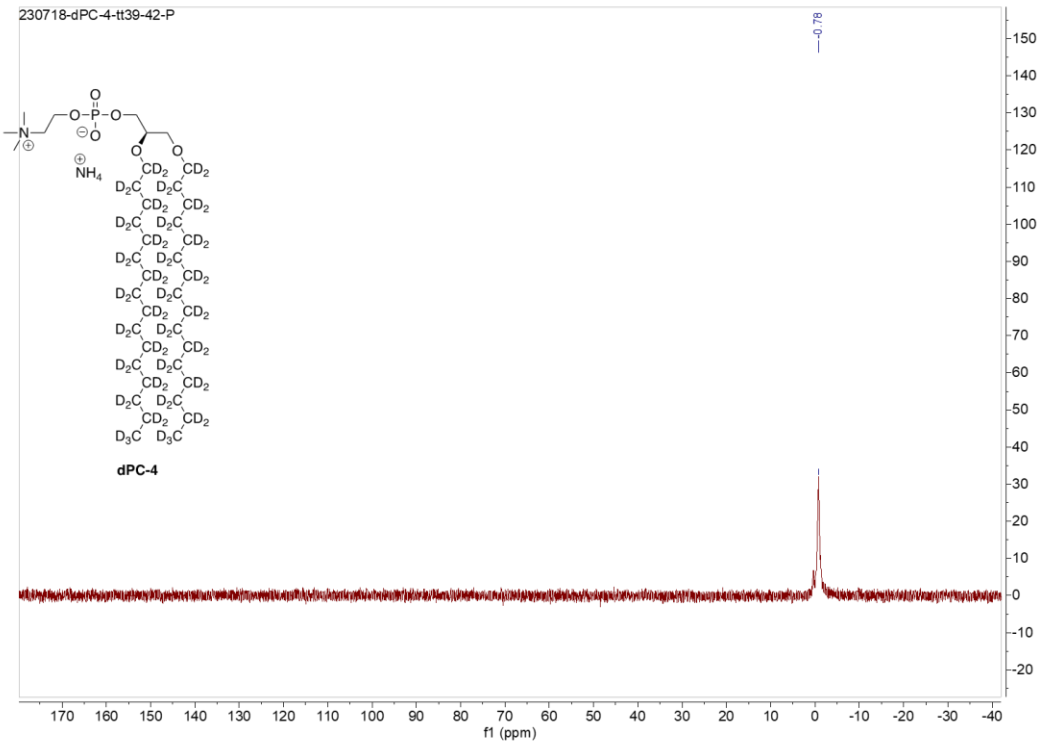


**DART-MS**

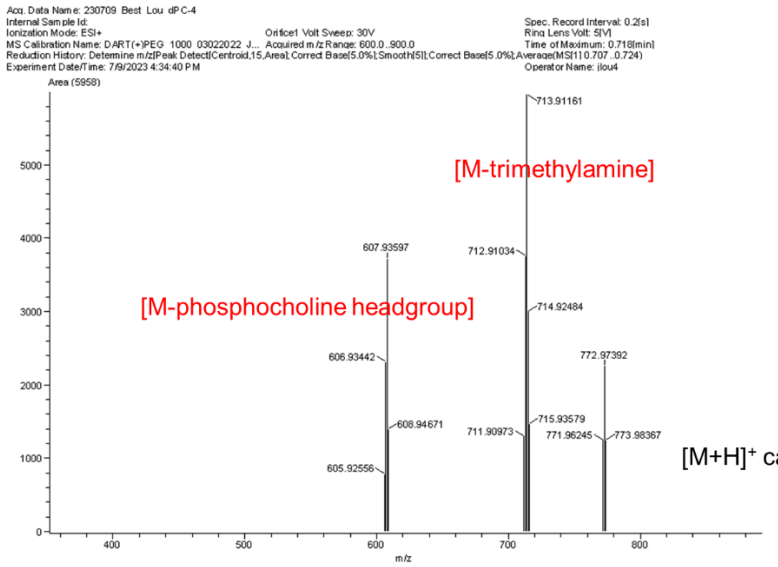


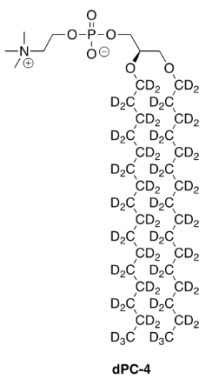


$[M+H]^+$ calcd for $C_{40}H_{19}D_{66}NO_6P$: 773.0252;
Found: 773.9837.

## VITA

Karan Sharma was born in Rampura Phul, Punjab, India in 1994. After completing his secondary education in city of Faridkot, Karan attended Panjab University, Chandigarh where he received his Bachelor of Science in chemistry in 2017. Following his undergraduate studies, Karan pursued a Master of Science in physical chemistry at Panjab University, Chandigarh graduating in 2019. During his masters studies, he worked as a research assistant gaining valuable experience in computational chemistry to study unconventional non-covalent interactions between modified DNA base pairs.

In fall of 2019, Karan commenced his doctoral studies at University of Tennessee, Knoxville, focusing on studying phase-separated lipid bilayer structures using various spectroscopic and microscopy techniques. Upon completion of his doctoral degree, Karan plans to work in the field of cheminformatics in academia/industry.